ESTIMATION OF EARTHQUAKE-INDUCED GROUND STRAINS USING STRONG MOTION RECORDS

強震記録を用いた地震時地盤ひずみの評価

KEIICHI TAMURA

田村敬一

(1)

ESTIMATION OF EARTHQUAKE-INDUCED GROUND STRAINS USING STRONG MOTION RECORDS

強震記録を用いた地震時地盤ひずみの評価

KEIICHI TAMURA

田 村 敬 一

March 1992

ABSTRACT

Since the dynamic behavior of buried lifeline facilities such as pipeline systems during earthquakes is governed by spatial variation of ground motion, or ground strain resulting from this spatial variation, it is most essential to estimate earthquake-induced ground strains appropriately in the seismic design of these structures. This spatial variation may also have significant influence on the seismic response of multiple-span bridges and widely spread tanks.

Because ground strain is defined as the spatial derivative of ground displacement, the reliability of displacement calculated from acceleration should be carefully considered, when strong motion accelerograms are employed for analysis. The reliability of displacement calculated from a 16 bits digital strong motion accelerograph data is experimentally studied. Shaking table tests with this accelerograph are carried out. The accuracy of calculated displacement is studied by comparing it to the directly measured displacement. It has been proven that this digital accelerograph may provide reliable acceleration data as low as 1/10 Hz for calculating displacement.

Two simple stochastic ground motion models are established and calibrated herein from strong motion array data at four sites in Shizuoka Prefecture, Japan. These adopt a stationary Gaussian random field model of each event's ground displacement in time and space. The first model chooses a coherence function that varies with separation distance but is independent of frequency. The coherence value estimated at the ground motion predominant frequency is employed as a representative in this model. The second model assumes the infinite propagation velocity of seismic waves, so that the time-space covariance function of ground displacement is a separable function of time and space. These models are applied to estimate the maximum relative displacement, using conventional Poisson models of temporal and spatial extremes. Ground strain can be estimated from this relative displacement.

The relative displacement statistics, both root mean square and maximum values, estimated from the proposed ground motion spectral models are compared with the observed array data, and they show good agreement. Little difference exists between the results estimated from these two introduced models.

The second proposed ground motion model is further applied to estimate the attenuation characteristics of the maximum ground strains. The temporal and spatial parameters are calibrated from conventional independent strong motion records and array data, respectively. The attenuation equation of the root mean square displacement is presented in this process.

The maximum relative displacement is estimated in terms of earthquake magnitude and epicentral distance. The maximum ground strain is derived from this maximum relative displacement, and is compared with the directly monitored ground and pipe strain data. The ground strains estimated by finite element analysis of array records are also employed in this comparison. The attenuation characteristics of ground strains based on the proposed estimation method have been found to give good approximation to the observed data.

ACKNOWLEDGMENTS

The author would like to express his sincere gratitude to Professor Tsuneo Katayama, the Institute of Industrial Science, University of Tokyo, for his supervision and guidance throughout the present study. Special appreciation is extended to Professor Fumio Yamazaki for reading a draft of this dissertation and making suggestive discussions. The author would also like to express his cordial thanks to Professor Motohiko Hakuno, the Earthquake Research Institute, University of Tokyo, Professors Yozo Fujino and Jun Kanda, University of Tokyo, for their valuable suggestions.

The author wishes to sincerely thank Dr. Toshio Iwasaki, the Public Works Research Institute, Ministry of Construction, for his hearty support since the author joined the Institute. Dr. Yasushi Sasaki and Mr. Tadashi Arakawa are greatly acknowledged for their guidance. The author wishes to express his appreciation to Dr. Kazuhiko Kawashima and Mr. Ken-ichi Tokida for their advice and encouragement in various aspects. Thanks are also extended to the author's colleagues at the Public Works Research Institute. Especially, Mr. Koh Aizawa is appreciated for his enormous contribution to the present study.

The research presented in Chapters 3 and 4 of this dissertation was mainly conducted while the author was a Visiting Scholar at the Department of Civil Engineering, Stanford University, on leave from the Public Works Research Institute. The author would like to express his sincere thanks to Professor Haresh C. Shah, Stanford University, for his support and guidance. Special gratitude is extended to Dr. Steven R. Winterstein. The author can never thank him enough for his informative discussions and continuous encouragement.

Finally, however most deeply, the author would like to thank his family for their support.

TABLE OF CONTENTS

LIST OF TABLES

LIST OF FIGURES

1. INTRODUCTION

1.1 Background of Present Study

Design Consideration of Earthquake-Induced Ground Strains

In the seismic design of buried lifeline facilities, such as pipeline systems and underground tunnels, the spatial variation of ground motion along structures should be carefully considered. This spatial variation may also have significant influence on the seismic response of multiple-span bridges and widely spread tanks.

From an engineering point of view, the seismic deformation method (Public Works Research Institute, 1977), which considers spatial patterns of ground deformation during earthquakes as seismic effects on structures, instead of inertia forces, was developed and is currently in practical use in Japan (Japan Society of Civil Engineers, 1988). This design concept was first adopted in the seismic design of petroleum pipelines (Japan Road Association, 1974) and submerged tunnels (Japan Society of Civil Engineers, 1975). Thereafter, the seismic deformation method has been widely employed in the seismic design of water supply pipelines (Japan Water Works Association, 1979), sewage pipelines (Japan Sewage Works Association, 1979), common utility ducts (Japan Road Association, 1986), and so on. While structural performance during earthquakes is governed by the precise ground motion details, in the seismic design method these motions are estimated from simple models of amplification and propagation of seismic waves in the surface strata. This is mostly due to the lack of measured ground deformation, i.e., ground strain data or simultaneous ground motion data at multiple spatial locations.

Reliability of Displacement Calculated from Strong Motion Acceleration Records

Strong ground motion observations have been providing valuable and the most essential data for earthquake engineering. Since its primary objective is to make clear strong motion characteristics which may cause damage to structures, it is common to monitor ground acceleration in strong motion observations. However, ground displacement is crucial to estimate ground strain, because strain is defined as the derivative of displacement with respect to space.

The calculation method of displacement from acceleration records and reliability of calculated displacement were studied mainly with SMAC accelerograph records in previous years (Goto et al., 1978; Iai et al., 1978a, 1978b; Kawashima et al., 1982a, 1982b). Recently, a number of studies (Yamada et al., 1989; Kataoka et al., 1990; Hayashi et al.,1991) have been carried out with newly developed digital strong motion accelerographs.

Two kinds of shaking table tests with a 16 bits digital accelerograph were conducted and the results are shown in Chapter 2. These experiments are principally aimed to prove reliable frequency range for displacement calculation and error of relative displacement calculated from the two accelerographs.

Measurement of Earthquake-Induced Ground Strains

As indicated previously, ground strains induced during earthquakes are most essential to assess the appropriate seismic effects to be considered in the seismic deformation method. Various studies have been performed to monitor ground or pipe strains during earthquakes (e.g., Sakurai et al., 1969; Nishio et al., 1978; Tsuchida et al., 1981; Iwamoto et al., 1982b; Katayama and Sato, 1982; Isenberg et al., 1990; Kawashima et al., 1991).

Sakurai et al. (1967, 1969, 1970) measured ground and pipe strains during the Matsushiro swarm earthquakes from December 1966 through January 1967. They pointed out that the pipe strain is almost equal to the ground strain, which means that pipe behavior during earthquakes is governed by ground deformation, and axial strain is considerably larger as compared with bending strain in the case of a small diameter straight pipe. Iwamoto et al. (1982a, 1982b) have conducted ground and pipe strain observations in Hachinohe City, Aomori Prefecture. They indicated that the ground strain is related to the quantity v/c (Toki, 1981), where v and c are particle velocity of the ground motion and the apparent propagation velocity of the seismic wave, respectively. Katayama et al. (1982; Sato et al., 1983, 1984) have monitored ground and pipe strains as a part of a very densely deployed array observation in Chiba City. They showed that the pipe strain which is mainly caused by the surface wave is correlated with the ground velocity, and that caused by body wave is correlated with the ground acceleration (Sato et al., 1986).

Ground Strain Estimation Using Conventional Strong Motion Records

Another approach to estimate ground strain depends on the strong ground motion records. At its first stage, the ground motion data obtained at only a point or a few points

were able to be incorporated into analyses. Kamiyama (1976) proposed an estimation procedure of ground strains caused by shear, Love and Rayleigh waves, taking into account the propagation characteristics of these waves. Takada and Wright (1980) employed the same ground strain estimation procedure with Iwamoto et al., and discussed the frequency dependence of propagation velocity and separation distance for which ground strain is calculated.

Ground Strain Estimation Using Strong Motion Array Records

The recent development of closely spaced arrays of accelerographs (Iwan ed., 1978) has provided new opportunities to study ground motion characteristics and its spatial variation. Especially, a number of array observation systems have been deployed in Japan (e.g., Noda et al., 1982, 1988; Katayama et al, 1984, 1990b; Iwasaki et al., 1986; Kitagawa et al., 1988; Japan Society of Civil Engineers, 1989a). An approach to study ground strains employs finite element analysis. Yamada et al. (1985) computed seismic ground strains from a two dimensional analysis based on a three point array observation system in Kawasaki City. Katayama et al. (1984; Farjoodi et al., 1985) estimated ground strains by using a three dimensional finite element method for various size elements with their Chiba dense instrument array records. They compared the calculation results with directly measured ground and pipe strains, and discussed the element size influence on the ground strain estimation. Arakawa et al. (1985) estimated ground strains using the array data at the Public Works Research Institute, Ministry of Construction, Japan and discussed the relationship between ground strain and ground velocity. This research is further extended to study the attenuation characteristics of ground strains in terms of earthquake magnitude and epicentral distance, and the results are given in Appendix C of this dissertation.

Array observation data have also been employed differently to estimate the spatial variation of ground motions, including ground deformation characteristics. Numerous studies have been reported with the data recorded at the SMART-1 array located in Lotung, Taiwan (e.g., Bolt et al., 1982; Abrahamson, 1985; Darragh, 1988; Hao, 1989; Niazi, 1990). It is common in these studies to model the spatial variation of ground motion as a stochastic process or, in multiple dimensions, a random field. These studies mainly focus on differential ground motion, seismic wave propagation and simulation of ground motion. Specific studies, together with modelling details, are cited in Chapter 3.

Two simple variants of standard ground motion spectral models are herein established. They are calibrated from the strong motion array data at the four sites in Shizuoka Prefecture, Japan. These adopt a stationary random field model of each event's ground displacement in time and space. These models are used to estimate the maximum relative displacements. Good agreement is found with the observed relative displacements, both root mean square and maximum values.

Attenuation Characteristics of Ground Strains

A few attempts have been made to study the attenuation characteristics of ground strains. Nakamura et al. (1982) studied the attenuation characteristics of pipe strains recorded at seven sites. Tokida et al. (1990, 1991) estimated ground strains from a finite element analysis using array observation data, and presented attenuation equations of the maximum ground strains. Although these studies provide valuable information about ground strain characteristics, it should be noted that most of the ground strain and ground motion array data so far obtained were recorded from relatively small events, and that the previous studies were basically based on those specific site records. Therefore, it may not be suitable to apply these research results directly to engineering practice. In order to compensate for this disadvantage, one of the proposed ground motion spectral models is further applied to estimate the maximum ground strains, partly using the conventional independent strong motion data recorded by the SMAC accelerographs. In Chapter 5 of this dissertation, an estimation method of the maximum ground strain attenuation is proposed.

1.2 Scope and Organization

The organization of this dissertation is as follows. Chapter 2 gives the results of the empirical study on the accuracy of displacement calculated from a 16 bits digital strong motion accelerograph. Two kinds of shaking table tests are carried out. They mainly focus on the reliable frequency range for displacement calculation and error of relative displacement calculated from two accelerographs. Effects of the number of bits of AD converting and its sampling interval on the accuracy of displacement are also presented.

Chapter 3 describes analytical stochastic ground motion models. The first half of this chapter sets forth various spectral models of ground displacement, and the latter half explains how these may be used to analytically estimate the root mean square and maximum values of relative displacement. Various studies in the literature differ primarily in the

precise details of their spectral models; Chapter 3 provides a survey of various models and introduces two new, simpler models for practical engineering analysis. These two models basically assume ground motion stationarity in both time and space. The maximum relative displacement is estimated by employing a Poisson arrival process model of extremes.

Numerical results are presented in Chapter 4. The ground motion spectral models introduced in Chapter 3 are calibrated from the array observation data. The relative displacement statistics estimated from the proposed two models are compared with the array data. These comparisons include both the root mean square and maximum values, and consider both radial and transverse components at all four sites.

Chapter 5 shows how one of the proposed ground motion models is applied to estimate the maximum relative displacement in terms of earthquake magnitude and epicentral distance, partly employing the conventional independent strong motion records. The temporal parameters of the ground motion model are calibrated from these records, and an empirical attenuation equation of the root mean square displacement is presented in this process. The maximum ground strain is derived from the maximum relative displacement, and its attenuation characteristics are compared with the directly measured ground and pipe strains. The ground strains estimated by the finite element procedure is also incorporated into this comparison.

Finally, Chapter 6 presents the major findings of the present study and some recommendations for future research.

2. RECORDING ACCURACY OF A DIGITAL STRONG MOTION ACCELEROGRAPH FOR CALCULATING GROUND DISPLACEMENT

2.1 General Remarks

It is common to monitor ground acceleration in strong ground motion observations for engineering purposes. Ground displacement can be calculated from ground acceleration by numerical integration, however it may diverge if the original acceleration record contains low frequency noise. Therefore, it is the general practice to remove low frequency noise by filtering, and the lower limit of frequency incorporated into filtering is necessary to be clear.

From this point of view, an empirical study was conducted to prove the recording accuracy of the SMAC-B2 accelerograph, which has provided most of the Japanese strong motion data currently available for engineering analyses (Kawashima et al., 1982a, 1982b). This accelerograph is a mechanical type accelerograph with the natural frequency of pendulum of 7.4 Hz and with the critical damping. Accelerograms are drawn on the scratching stylus roll-paper by a diamond nail. According to their results, SMAC-B2 accelerograph records are stable over the frequency range of 1/3 to 12 Hz for calculating displacement, taking into account the accelerograph performance and digitization process.

The recording accuracy of a 16 bits digital strong motion accelerograph is empirically studied (Tamura et al., 1988). This accelerograph is used for the dense instrument array observations by the Public Works Research Institute, Ministry of Construction, Japan. Shaking table tests of the digital strong motion accelerograph are carried out, and the accuracy of displacement calculated from acceleration is studied by comparing it with the directly measured shaking table displacement. Effects of the lower cut-off frequency of instrumental correction filter, the number of bits of AD converting and its sampling interval on the accuracy of calculated displacement are studied.

In addition to the accuracy of displacement obtained from an accelerograph record, the accuracy of relative displacement estimated from two independent accelerographs is also crucial to estimate earthquake-induced ground strain appropriately, because ground strain is basically defined as dividing the difference of two ground displacement time histories by

the separation distance. Taking this point into account, the reliability of relative displacement calculated from two accelerograph records is also studied by exciting eight digital accelerographs simultaneously on a shaking table. The relative displacement resulting from two accelerograph data is considered an error, and the amount of this error is discussed by comparing it to the maximum displacement.

2.2 Shaking Table Tests of a Digital Strong Motion Accelerograph

2.2.1 Shaking Table Tests for Studying Displacement Accuracy (Experiment I)

A digital strong motion accelerograph is fixed on an electro-magnetic shaking table, and is excited by actual strong motion records. Main specifications of the accelerograph is given in Table 2.1. The maximum stroke of the shaking table is ±20 cm and this shaking table performs well in the low frequency range. The displacement of the shaking table is measured by a differential transformer displacement-meter. Its resolution is 1/50 mm.

Table 2.1 Main specifications of the digital accelerograph

Accelerometer	Type	Velocity feed-back servo type
	Full scale	±1000 gal
	Natural period	5 Hz
	Damping ratio	240
Trigger system	Sensitive direction	Vertical
	Trigger level	±5 gal (changeable)
Recording system	Type	Digital
	Number of channels	3 (horizontal: 2, vertical: 1)
	Media	Cartridge tape
	Number of bits	16
	Sampling rate	200 samples/second
	Recording time	30 minutes
	Pre-event memory	5 seconds
Clock	Accuracy	10^{-7}
	Calibration	Every 1 hour by radio signal

Table 2.2 Input motions for experiments

Date	Epicentral region	Magnitude	Epicentral distance [km]	Recording station
2/29/72	E off Hachijojima	7.0	300	Futtsu Cape (N-S)
11/25/73	Central Wakayama Pref	5.9	100	Osaka South Port (N-S)
8/4/74	SW Ibaraki Pref	5.8	90	Ohgishima (E-W)
6/29/80	Izu Peninsula Region	6.7	47	Numazu Bypass (N-S)
8/6/68	W Coast of Ehime Pref	5.3	18	Itajima Bridge (LG)

Table 2.3 Maximum values of experiment I

Record name	Case No.	Max.acceleration [gal]	Max.displacement [cm]
Futtsu Cape	1-a	196.2	2.83
	1-b	806.7	11.91
South Port	2-a	133.9	4.50
	2-b	469.9	16.32
Ohgishima	3-a	196.0	3.49
	3-b	656.4	9.16
Numazu	4-a	274.3	1.20
	4-b	746.1	3.06
Itajima Bridge	5-a	257.7	0.85
	5-b	782.5	2.50

The five strong motion records listed in Table 2.2 are employed as input motions for shaking table tests. Maximum acceleration levels are changed as two cases for every record as shown in Table 2.3. Note that the maximum acceleration is set as greater than 100

gals, this is because the ground motion with this level should be considered in the seismic design of civil engineering structures. Fig.2.1 shows acceleration time histories. From a point of strong motion duration, strong motion records with duration of 40 seconds or longer are basically selected. The Itajima Bridge record is exclusively short, which is employed for reference. Fig.2.2 shows the acceleration response spectra of these five records, where the damping ratio to the critical is taken as 0.05. As seen from this figure, strong motion records with various predominant periods are chosen as input motions for the experiments.

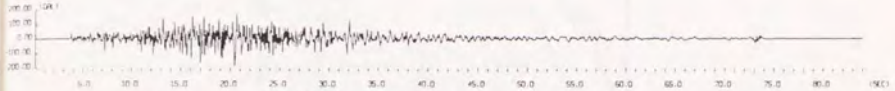

(a) Futtsu Cape (Experiment I, Case 1-a)

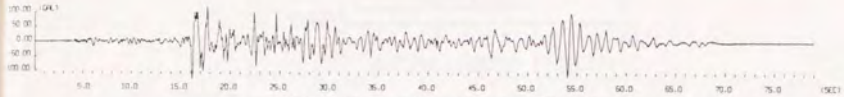

(b) South Port (Experiment I, Case 2-a)

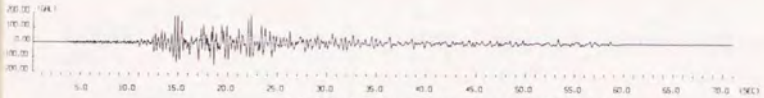

(c) Ohgishima (Experiment I, Case 3-a)

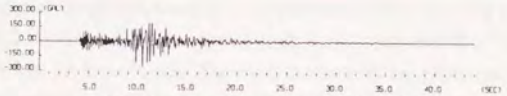

(d) Numazu (Experiment I, Case 4-a)

(e) Itajima Bridge (Experiment I, Case 5-a)

Fig.2.1 Acceleration time histories of experiment input motions

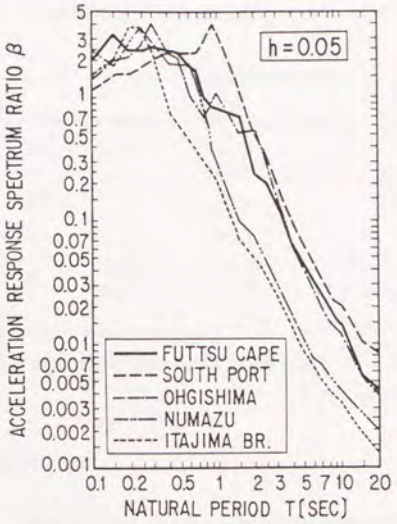

Fig.2.2 Acceleration response spectra of input motions (h=0.05)

2.2.2 Shaking Table Tests for Studying Relative Displacement Accuracy (Experiment II)

Eight independent 16 bits digital accelerographs are fixed on an electro-hydraulic shaking table and excited by strong motion records. These accelerographs are the same type as the digital accelerograph employed in the experiment I. They are very carefully set up to hold the same excitation direction with a long steel ruler, and they are synchronized immediately before the experiments. The input motions for the experiments are same with those for experiment I, which are shown in Table 2.2, and shaking levels are changed for two levels as shown in Table 2.4. Since the accelerographs are firmly fixed on the rigid table, no relative displacement can physically arise between accelerographs. If relative motion is found between displacement data calculated from accelerograph records, it should be due to the error associated with recording and/or processing of data.

Table 2.4 Maximum values of experiment II

Record name	Case No.	Max.acceleration [gal]*	Max.displacement [cm]**
Futtsu Cape	1-a	167.6	2.90
	1-b	351.2	4.70
South Port	2-a	157.6	3.02
	2-b	243.5	6.96
Ohgishima	3-a	139.3	2.91
	3-b	343.4	4.95

Note: * Mean value of eight accelerographs

** Mean value of eight calculated displacement data

2.3 Calculation of Displacement

Displacement of ground motion is calculated by integrating an acceleration record in the frequency domain as follows (Goto et al., 1978).

The Fourier transform $F_0(f)$ of original acceleration record $a_0(t)$ is written as

$$F_0(f)=\int_{-\infty}^{\infty} a_0(t)\exp(-i2\pi ft)dt \tag{2.1}$$

Introducing an instrument correction filter $F_C(f)$, the corrected acceleration $a(t)$ is obtained as

$$a(t)=\int_{-\infty}^{\infty} F(f)\exp(i2\pi ft)df \tag{2.2}$$

where

$$F(f)=F_0(f)F_C(f) \tag{2.3}$$

$$F_C(f)=\begin{cases} 0 \cdots\cdots\cdots\cdots\cdots\cdots f<f_{ll} \\ \dfrac{f-f_{ll}}{f_{lu}-f_{ll}}\dfrac{\exp\{p(f)\}}{A(f)} \cdots f_{ll}\leq f\leq f_{lu} \\ \dfrac{\exp\{p(f)\}}{A(f)} \cdots\cdots\cdots f_{lu}<f<f_{ul} \\ \dfrac{f_{uu}-f}{f_{uu}-f_{ul}}\dfrac{\exp\{p(f)\}}{A(f)} \cdots f_{ul}\leq f\leq f_{uu} \\ 0 \cdots\cdots\cdots\cdots\cdots\cdots f_{uu}<f \end{cases} \tag{2.4}$$

f_{lu} and f_{ul} in Eq.(2.4) represent the lower and the upper cut-off frequencies, respectively. f_{ll} and f_{uu} are the frequencies at which the amplitude of correction filter becomes 0 in low and high frequency range, respectively. $A(f)$ and $p(f)$ in Eq.(2.4) are the amplitude and phase characteristics functions of the accelerograph, respectively, which are shown in Fig.2.3 (Arakawa et al., 1983b). Velocity $v(t)$ and displacement $d(t)$ can be obtained from Eq.(2.2) as

$$v(t)=\int_{-\infty}^{\infty}\frac{F(f)}{i2\pi f}\exp(i2\pi ft)df \tag{2.5}$$

$$d(t)=\int_{-\infty}^{\infty}\frac{F(f)}{-4\pi^2 f^2}\exp(i2\pi ft)df \tag{2.6}$$

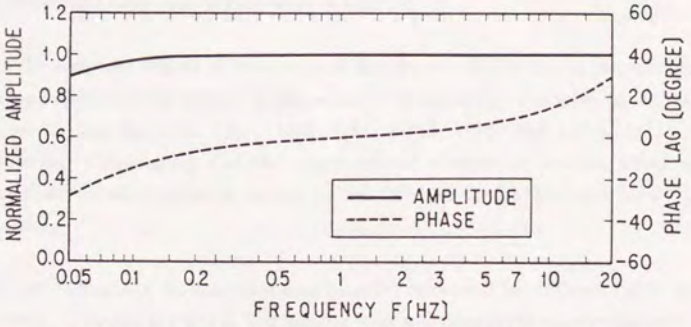

Fig.2.3 Amplitude and phase characteristics of the digital accelerograph

2.4 Accuracy of Displacement

The accuracy of calculated displacement $d(t)$ given by Eq.(2.6) is studied by comparing with the shaking table displacement $D(t)$ directly measured by a differential transformer displacement-meter. The following three parameters are defined to compare $d(t)$ with $D(t)$ (Kawashima et al., 1982b; Tamura et al., 1988):

$$\sigma=\frac{1}{T_d}\int_0^{T_d}\left|d(t)^2-D(t)^2\right|dt \tag{2.7}$$

$$\mu=\frac{\int_0^{T_d} d(t)^2dt}{\int_0^{T_d} D(t)^2dt} \tag{2.8}$$

$$\xi=\frac{|d(t)|_{\max}}{|D(t)|_{\max}} \tag{2.9}$$

where T_d is duration of $d(t)$ and $D(t)$. As seen from Eqs.(2.7), (2.8) and (2.9), σ approaches to 0, and μ and ξ approach to 1, as $d(t)$ agrees well with $D(t)$. σ has a dimension of square length. It is not normalized in order to see the effects of ground motion amplitude on the accuracy of calculated displacement.

2.4.1 Effects of Lower Cut-off Frequency of Filtering

To study the effects of lower cut-off frequencies of filtering on the accuracy of calculated displacement, ground displacement is calculated by changing f_{lu} and f_{ll} of Eq.(2.4) as (f_{lu}, f_{ll})=(1/5, 1/6), (1/10, 1/11) (1/15, 1/16) and (1/20, 1/21) [Hz], respectively. Considering that the upper cut-off frequencies do not affect much displacement calculation results, f_{ul} and f_{uu} are fixed as f_{ul}=20 [Hz] and f_{uu}=21 [Hz], respectively.

An example of displacement time histories calculated for different lower cut-off frequencies is shown in Fig.2.4. The directly measured displacement time history is also shown in the same figure. Any apparent difference is hard to be seen between calculated

displacement time histories for changing $1/f_{lu}$ from 5 to 20 seconds and the directly measured displacement.

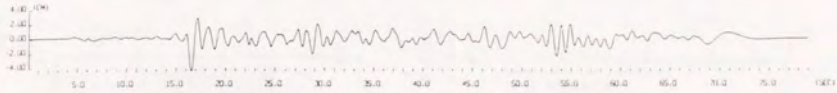

(a) Measured displacement

(b) $1/f_{lu}$=20 [s]

(c) $1/f_{lu}$=15 [s]

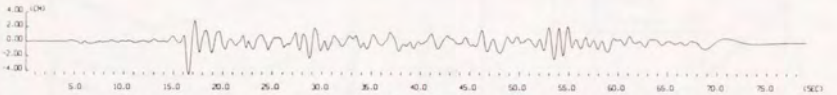

(d) $1/f_{lu}$=10 [s]

(e) $1/f_{lu}$=5 [s]

Fig.2.4 Displacement time histories for various cut-off periods (Experiment I, Case 2-a)

Relationships between the cut-off period $1/f_{lu}$ and parameters σ, μ and ξ are shown in Figs.2.5 to 2.7, respectively. The following can be pointed out from these figures.

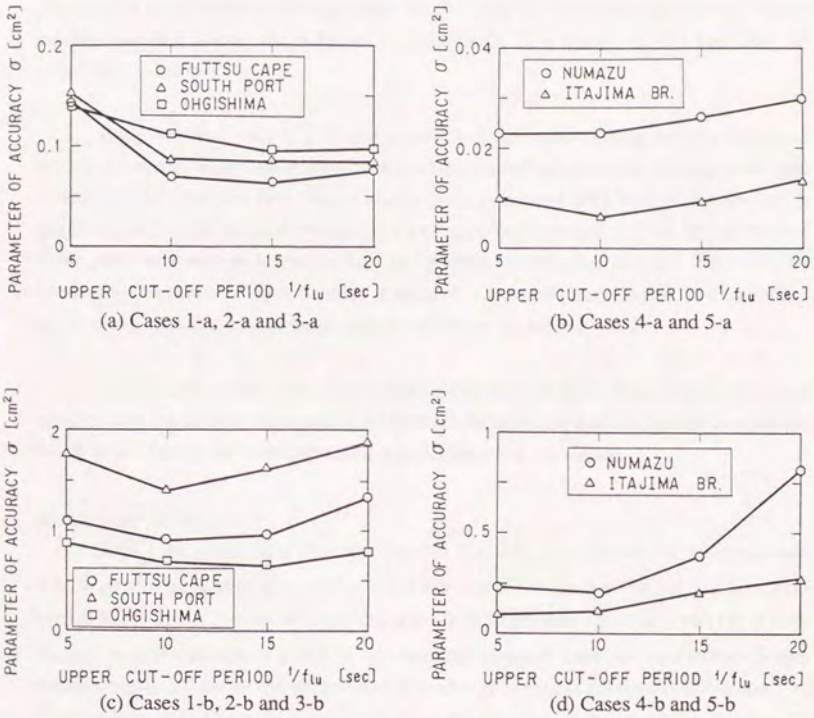

(a) Cases 1-a, 2-a and 3-a

(b) Cases 4-a and 5-a

(c) Cases 1-b, 2-b and 3-b

(d) Cases 4-b and 5-b

Fig.2.5 Parameter of accuracy σ

(1) Accuracy Defined by σ

In experiment case Nos.1-a, 2-a and 3-a, σ decreases as $1/f_{lu}$ becomes from 5 to 10 seconds. σ takes its minimum value between $1/f_{lu}$=10 and 20 [s]. In case of Nos.1-b, 2-b

and 3-b, in which the same ground motion records are employed with Nos.1-a, 2-a and 3-a and only acceleration levels are set as higher, σ takes its minimum value between $1/f_{lu}$=10 and 15 [s]. Whereas, σ takes its minimum value between $1/f_{lu}$=5 and 10 [s] in experiment case Nos.4-a, 5-a, 4-b and 5-b. σ increases as $1/f_{lu}$ increases from 10 to 20 seconds.

According to these experiment results, σ generally takes its minimum value when $1/f_{lu}$ is taken as 10 seconds. In other words, the accuracy of calculated displacement can be regarded as best when $1/f_{lu}$ is taken as 10 seconds. The reason of this fact may be interpreted as follows:

It is desirable to take $1/f_{lu}$ as long as possible to estimate the long-period component motion. However, acceleration amplitude of a long-period component is usually small, and its accuracy is relatively low. Therefore, the error associated with long-period motion is amplified during the integral process. For example, Numazu and Itajima Bridge records show good accuracy with shorter $1/f_{lu}$ as compared with other records. This may be because the duration of these records is relatively short and they do not predominantly contain long-period components of ground motion as shown in Fig.2.2.

On the other hand, when $1/f_{lu}$ is taken short, the calculated displacement becomes smaller than the directly measured displacement, because the ground motion component longer than $1/f_{lu}$ can not be incorporated into displacement calculation.

(2) Accuracy Defined by μ

As for the experiment case Nos.1-a, 1-b, 2-a, 2-b, 3-a, 3-b and 4-a, the parameter μ is almost 1.0 without regard to $1/f_{lu}$, except that it is a little smaller than 1.0 at $1/f_{lu}$ =5 [s] in case Nos.1-a, 2-a, 3-a and 4-a, and that it is a little larger than 1.0 at $1/f_{lu}$ =20 [s] in case No.2-b. μ seems to increase a little as $1/f_{lu}$ becomes longer in case No.5-a, however μ still remains nearly 1.0 for all cut-off periods. This change is clearer for case Nos.4-b and 5-b, μ becomes large as $1/f_{lu}$ becomes long. The cut-off period at which μ is closest to 1.0 is 10 seconds.

Although the change of μ with $1/f_{lu}$ is not very large, and μ is nearly 1.0 irrespective of $1/f_{lu}$ in most experiment cases, these results are not contradictory to the former result of displacement accuracy dependence on cut-off periods studied by the parameter σ.

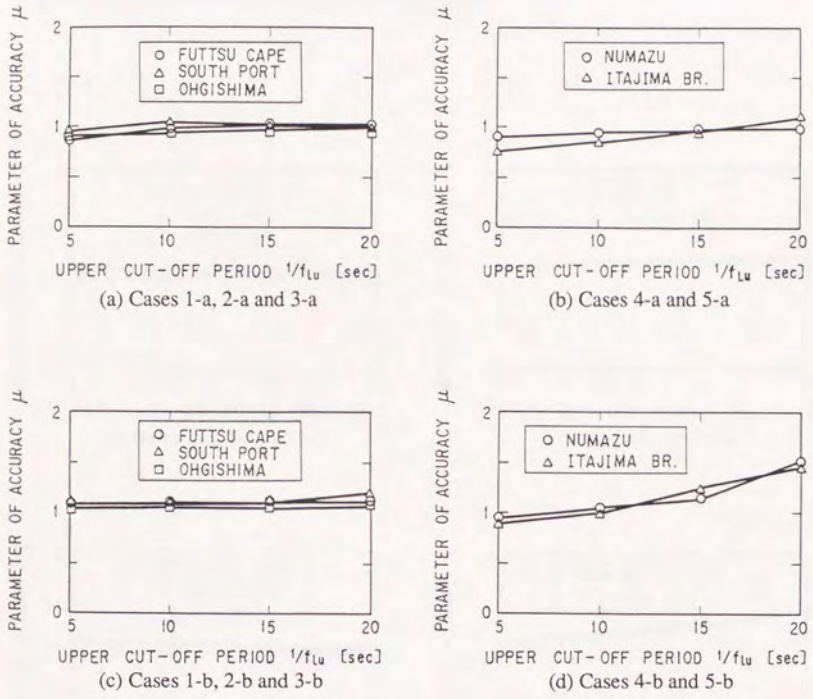

(a) Cases 1-a, 2-a and 3-a

(b) Cases 4-a and 5-a

(c) Cases 1-b, 2-b and 3-b

(d) Cases 4-b and 5-b

Fig.2.6 Parameter of accuracy μ

(3) Accuracy Defined by ξ

Comparing to the case of parameter μ, the parameter ξ is still less sensitive to the change of $1/f_{lu}$. ξ is almost 1.0 for $1/f_{lu}$ =5 to 20 [s] in most experiment cases. As for the Numazu and Itajima Bridge records, ξ is closest to 1.0 when $1/f_{lu}$ is 5 seconds.

Combining the above mentioned facts based on the parameters σ, μ and ξ, $1/f_{lu}$ may be taken as long as 10 seconds in the scope of present study. However, it may be suitable to set $1/f_{lu}$ as 5 seconds, when the strong motion duration is short, and the long-period ground motions are not predominantly included.

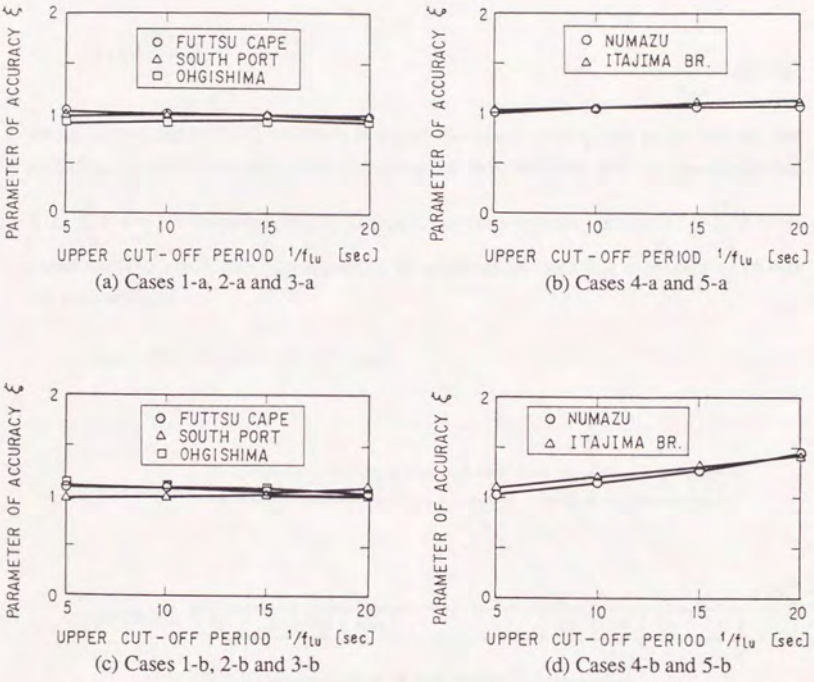

(a) Cases 1-a, 2-a and 3-a

(b) Cases 4-a and 5-a

(c) Cases 1-b, 2-b and 3-b

(d) Cases 4-b and 5-b

Fig.2.7 Parameter of accuracy ξ

2.4.2 Effects of Number of Bits of AD Converting

Effects of the number of bits of AD converting on the accuracy of calculated displacement is numerically studied by changing the number of AD converting bits from 16 to 10.

An acceleration value A can be expressed by 16 bits AD converting as follows: An integer number which can be expressed by 16 bits digit X_{16} is given by

$$X_{16}=\sum_{i=0}^{15} a_i 2^i \tag{2.10}$$

where a_i takes either 0 or 1 as shown in Fig.2.8 (a), which corresponds to the i-th bit. The recording range of the strong motion accelerograph is ±1000 gals. The maximum value of X_{16}, $\sum_{i=0}^{15} 1\cdot 2^i=2^{16}-1$ corresponds to 1000 gals, and the minimum value of X_{16}, $\sum_{i=0}^{15} 0\cdot 2^i=0$ corresponds to –1000 gals. Consequently, an acceleration value A is expressed by 16 bits AD converting as

$$A_{16}=1000\{2X_{16}/(2^{16}-1)-1\} \quad \text{[gal]} \tag{2.11}$$

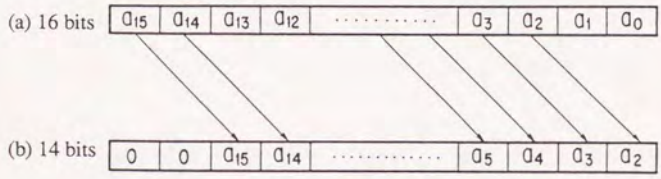

Fig.2.8 Comparison of 16 and 14 bits AD converting

Let us express the same acceleration value A by 14 bits AD converting. In the case of 14 bits AD converting, the lower 2 bits of 16 bits AD converting is truncated as shown

in Fig.2.8 (b). Therefore, an integer number which can be expressed by 14 bits AD converting is given by

$$X_{14}=\sum_{i=0}^{13} a_{i+2}2^i$$
$$=[X_{16}/4] \tag{2.12}$$

where $[N]$ indicates the maximum integer number which does not exceed N. Similar to Eq.(2.11), an acceleration value A is expressed by 14 bits AD converting as

$$A_{14}=1000\{2X_{14}/(2^{14}-1)-1\} \quad [\text{gal}] \tag{2.13}$$

Substituting Eq.(2.12) into Eq.(2.13) yields an acceleration value which corresponds to a 14 bits AD converter inferred from the acceleration X_{16} recorded by a 16 bits AD converter. Similarly, acceleration values corresponding to 12 and 10 bits AD converting can be estimated.

The cut-off frequencies for filtering to calculate displacement are set up as f_{ll}=1/11, f_{lu}=1/10, f_{ul}=20, f_{uu}=21 [Hz] based on the previous results. The experiment cases considered are Nos.1-a, 1-b, 2-a, 2-b, 3-a and 3-b.

Fig.2.9 shows an example of displacement time histories, where the number of bits of AD converting is changed from 16 to 10 bits. Little difference can be found among these time histories.

(a) Measured displacement

(b) 16 bits

(c) 14 bits

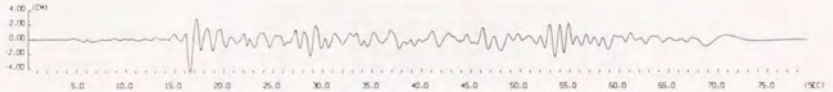

(d) 12 bits

(e) 10 bits

Fig.2.9 Displacement time histories for various AD converting (Case 2-a)

Fig.2.10 shows the parameters σ, μ and ξ calculated for 16 to 10 bits AD converting. Results are shown for cases 1-a, 2-a and 3-a. According to these results, little difference can be seen for the accuracy of displacement with changing the number of AD converting from 16 to 10 bits. This may be due to the fact that the acceleration level of experiments is considerably high. Even in the smallest case, No.2-a, the maximum

acceleration is about 130 gals, and is sufficiently large as compared with the resolution of 10 bits AD converting, which is 1.96 gal (=2000/(2^{10}–1)).

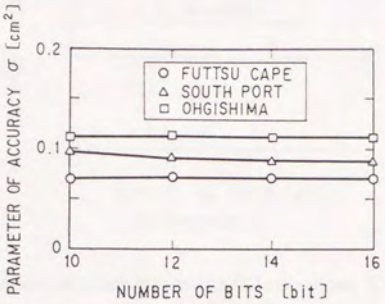

(a) Parameter σ

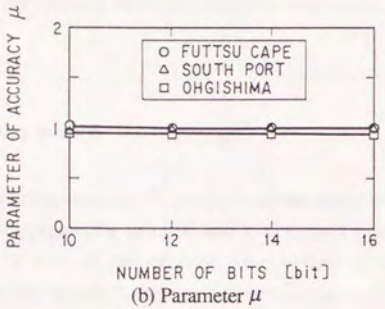

(b) Parameter μ

Fig.2.10(1) Displacement accuracy for various AD converting (Cases 1-a, 2-a and 3-a)

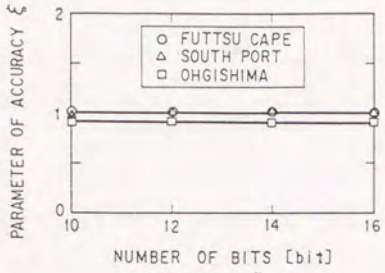

(c) Parameter ξ

Fig.2.10(2) Displacement accuracy for various AD converting (Cases 1-a, 2-a and 3-a)

It may be concluded that the number of AD converting changing over 16 to 10 bits does not much affect the accuracy of displacement, as long as the ground motion level is sufficiently high.

2.4.3 Effects of Sampling Interval

Effects of a sampling interval Δt on displacement accuracy is also studied. The acceleration records corresponding to 1/100 and 1/50 second sampling are estimated by taking every 2 and 4 data of the original time history data with 1/200 second sampling,respectively. The cut-off frequencies of instrumental correction filter are taken in the same procedure as Section 2.4.2; f_{lt}=1/11, f_{lu}=1/10, f_{ut}=20, f_{uu}=21 [Hz]. The experiment cases considered are Nos.1-a, 1-b, 2-a, 2-b, 3-a and 3-b.

An example of displacement time histories calculated from acceleration data with different sampling intervals is shown in Fig.2.11. Little difference can be seen between the cases of Δt=1/200 and 1/100 [s]. However, noise can be recognized at the first portion of displacement time history with Δt=1/50 [s].

(a) Measured displacement

(b) Δt=1/200 [s]

(c) Δt=1/100 [s]

(d) Δt=1/50 [s]

Fig.2.11 Displacement time histories for various sampling intervals (Case 2-a)

Fig.2.12 shows the parameters σ, μ and ξ. Seen from this figure, σ takes almost the same value for Δt=1/200 and 1/100 [s]. σ for Δt=1/50 [s] is larger than those for Δt=1/200 and 1/100 [s]. The parameter μ is almost 1.0 for Δt=1/200 and 1/100 [s], however it is apparently greater than 1.0 when Δt is taken as 1/50 second. ξ does not change very much over Δt=1/200 to 1/50 [s], and is almost 1.0.

The displacement integrated from acceleration has almost the same accuracy for Δt=1/200 and 1/100 [s]. The accuracy for Δt=1/50 [s] is lower as compared with the cases of Δt=1/200 and 1/100 [s].

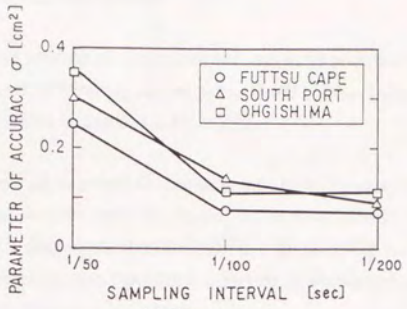

(a) Parameter σ

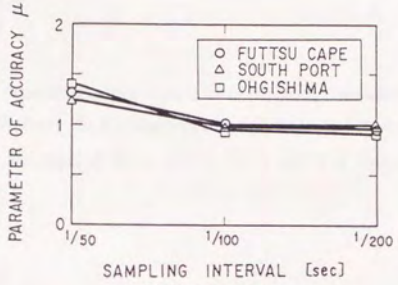

(b) Parameter μ

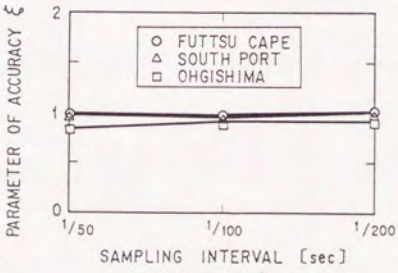

(c) Parameter ξ

Fig.2.12 Displacement accuracy for various sampling intervals (Cases 1-a, 2-a and 3-a)

2.5 Reliability of Relative Displacement

The calculation method of displacement is the same with that shown in Section 2.3, and cut-off frequencies of filtering are set up as f_{ll}=1/11, f_{lu}=1/10, f_{ul}=20, f_{uu}=21 [Hz] based on the results shown in Section 2.4.1.

Fig.2.13 shows an example of displacement time histories calculated from eight accelerograph records. As seen from this figure, all the time histories look almost identical. An example of relative displacement time histories is given in Fig.2.14. To demonstrate the accuracy of relative displacement calculated from two accelerograph records, the following parameter η is defined (Tamura et al., 1988):

$$\eta=\frac{|d_i(t)-d_j(t)|_{\max}}{|d_j(t)|_{\max}} \tag{2.14}$$

where $d_i(t)$ and $d_j(t)$ represent displacement time histories estimated from the i-th and j-th accelerographs, respectively. In the analysis that follows, the j-th accelerograph is fixed to a accelerograph (Accelerograph No.8 in Fig.2.13) and η is calculated for other seven accelerographs.

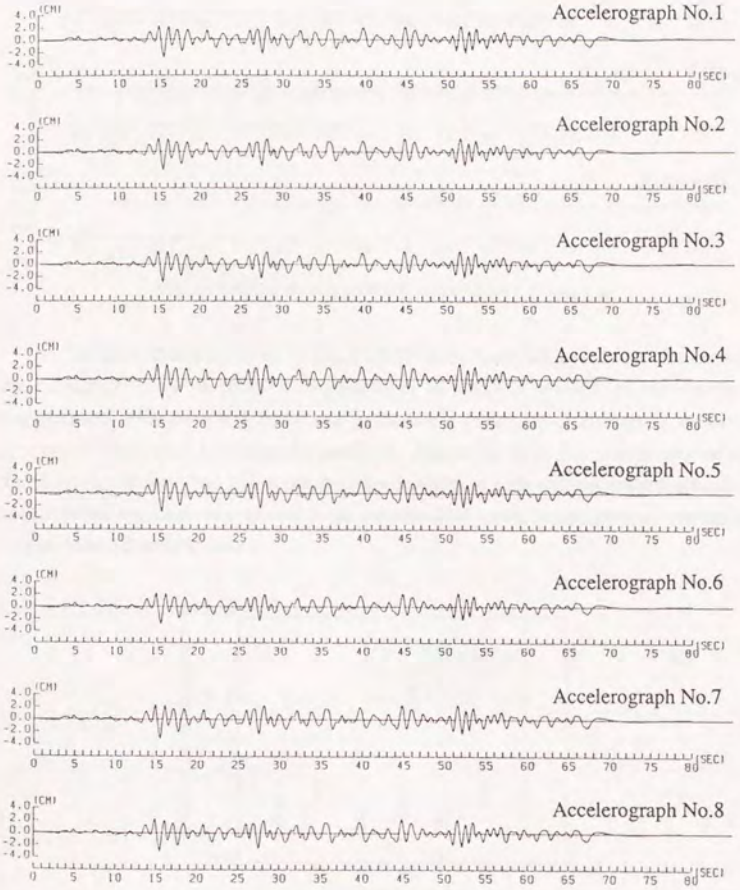

Fig.2.13 Displacement time histories calculated from eight accelerograph records (Case 2-a)

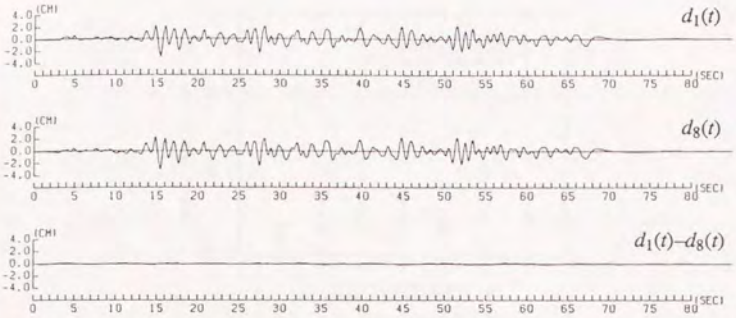

Fig.2.14 Relative displacement time history (Case 2-a)

The parameter η is shown in Fig.2.15. η varies from 0.05 to 0.1, which means that the maximum error of relative displacement is about 5 to 10% of the maximum displacement. This error may be caused by the slight difference of instrument sensitivity, synchronization and installation condition. Assuming that the maximum relative displacement between two points has the same magnitude with the maximum displacement at each point, the maximum ground strain estimated form two independent accelerographs may include a 5 to 10% error.

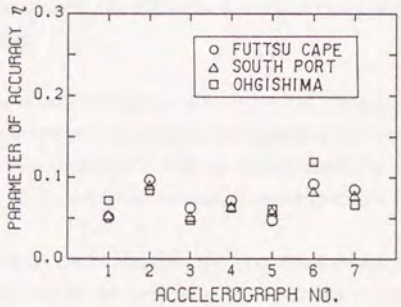

(a) Cases 1-a, 2-a and 3-a

Fig.2.15(1) Relative displacement accuracy

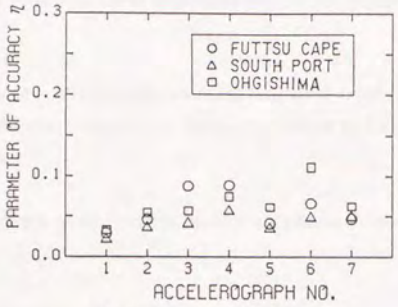

(b) Cases 1-b, 2-b and 3-b

Fig.2.15(2) Relative displacement accuracy

2.6 Conclusions

The accuracy of displacement calculated from a 16 bits digital strong motion accelerograph is studied by shaking table tests. Effects of the lower cut-off frequency of filtering, the number of bits of AD converting and sampling interval on the accuracy of displacement are studied. The reliability of relative displacement estimated from two accelerographs is also studied. The following conclusions may be deduced from the study presented in this chapter.

1) The lower cut-off frequency of instrumental correction filter for calculating displacement from the 16 bits digital strong motion accelerograph may be taken as low as 1/10 Hz. However, it may be recommended to take the lower cut-off frequency as 1/5 Hz, when the duration of strong motion is relatively short.

2) Little difference can be found for displacement accuracy when the number of bits of AD converting is changed from 16 to 10 bits, if ground motion level is considerably high, e.g., greater than 100 gals.

3) Little difference exists between the accuracy of displacement with sampling intervals of 1/200 and 1/100 second. Accuracy of displacement with sampling interval 1/50 second is lower than those for sampling intervals of 1/200 or 1/100 second.

4) The maximum relative displacement estimated from two independent digital accelerographs may include an error corresponding to 5 to 10 % of the maximum displacement.

In the following chapters, strong motion records are processed considering the results of this chapter.

3. STOCHASTIC FORMULATION OF TIME–SPACE VARYING GROUND MOTIONS

3.1 General Remarks

The recent development of closely spaced arrays of accelerographs (Iwan ed., 1978) has provided valuable data for the analysis of ground motion and its spatial variation. Numerous studies (e.g., Bolt et al., 1982; Abrahamson et al., 1987) have been reported with the data recorded at the SMART-1 array located in Lotung, Taiwan. It is usual in these studies to model the spatial variation of ground motion as a stochastic process or a random field in multiple dimensions. These studies mainly focus on differential ground motion, seismic wave propagation and simulation of ground motion. Specific studies, together with modelling details, are cited in the next section.

Two simple variants of standard ground motion spectral models are here introduced to reduce data collection and processing needs. These adopt a stationary Gaussian random field model of each event's ground displacement in time and space (Tamura et al., 1990, 1991). Although adequacy for assuming temporal and spatial stationarity of ground motion requires future studies, this assumption may be acceptable at present (Hoshiya et al., 1987). The first model employs a coherence function that varies with separation length but is independent of frequency. A coherence value is estimated at the ground motion predominant frequency in this model. The second model assumes the apparent horizontal propagation velocity of seismic waves to be infinite, so that the time-space covariance function of ground motion is a separable function of time and space.

The time-space covariance function of relative displacement between two points on the ground surface is derived from the proposed ground motion spectral models. Assuming that the crossings of a specified threshold occur as a Poisson arrival process, both the temporal maximum relative displacement over any fixed distance and the spatial maximum at any fixed time are estimated.

3.2 Background

Assuming that the earthquake ground motion displacement $u(t, x)$ results from a stationary Gaussian process with zero mean which is a function of both time t and spatial coordinate x, the time-space covariance function $C(\tau,\eta)$ is defined as

$$C(\tau,\eta)=\mathrm{E}[u(t+\tau, x+\eta)u(t, x)] \tag{3.1}$$

where E[ ] represents the expectation operator. Transforming time lag τ into frequency f by means of the Wiener-Khinchine relationship, the time-space cross spectral density function $S(f,\eta)$ can be obtained as

$$S(f,\eta)=\int_{-\infty}^{\infty} C(\tau,\eta)\exp(-i2\pi f\tau)d\tau \tag{3.2}$$

Viewing the displacement process over space at a fixed time, substituting τ=0 into Eq.(3.1) yields the spatial covariance function $C_S(\eta)$ as

$$\begin{aligned} C_S(\eta)&=C(0,\eta)\\ &=\sigma_u^2\rho_S(\eta)\end{aligned} \tag{3.3}$$

where σ_u^2 and $\rho_S(\eta)$ are the mean square value of displacement and the correlation function in space at any fixed time, respectively. If the time-space process is assumed to be ergodic and its mean value has been removed, σ_u^2 can be estimated as

$$\sigma_u^2=\lim_{T\to\infty}\frac{1}{T}\int_0^T u(t, x)^2dt \tag{3.4}$$

where T is duration of ground motion. Fig.3.1 shows the relationship among Eqs.(3.1), (3.2) and (3.3). The functions listed in the lower row of Fig.3.1 are translations into the wave number domain. Those functions are related to each other by the Wiener-Khinchine relationship.

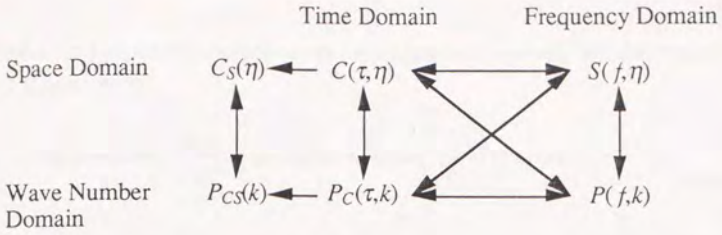

Fig.3.1 Relationship among stochastic functions for a time-space varying process

Typical previous studies on the time-space variation of ground motion may be classified into three groups. One approach is to model the time-space cross spectral density function $S(f,\eta)$. Assuming that seismic waves propagate horizontally, Eq.(3.2) may be described as (Loh, 1985; Harichandran, 1988)

$$S(f,\eta)=S_0(f)\gamma(f,\eta)\exp\left(-i\frac{2\pi f\eta}{c}\right) \tag{3.5}$$

where $S_0(f)$ is the power spectral density function of displacement u at any fixed location x, $\gamma(f,\eta)$ is the coherence function, and c is the apparent propagation velocity of seismic waves. Several models of coherence function have been proposed. Kawakami and Sato (1983) proposed the following model:

$$\gamma(f,\eta)=\exp\left(-\alpha\frac{f\eta}{c}\right) \tag{3.6}$$

where α is a constant. In this model, the coherence is assumed to decrease exponentially according to the product of frequency f and wave propagation delay η/c. Loh (1985) considered the following four functions:

$$\gamma(f,\eta)=\begin{cases}\exp(-\alpha_1|\eta|)\\ \exp(-\alpha_1|\eta|)(1+\alpha_1|\eta|+\alpha_1|\eta|^2)\\ \exp\{-(\alpha_1\eta)^2\}\\ \exp\{-(\alpha_1+\alpha_2 f)|\eta|\}\end{cases} \tag{3.7}$$

where α_1 and α_2 are empirical constants. Harichandran and Vanmarcke (1986) proposed the following model:

$$\gamma(f,\eta)=A\exp\left\{-\frac{2\eta}{\alpha\theta(f)}(1-A+\alpha A)\right\}+(1-A)\exp\left\{-\frac{2\eta}{\theta(f)}(1-A+\alpha A)\right\} \tag{3.8}$$

$$\theta(f)=k\left\{1+\left(\frac{f}{f_0}\right)^b\right\}^{-1/2} \tag{3.9}$$

where A, α, k, f_0 and b are parameters to be estimated by regression analysis.

A second approach is to model the spatial correlation function $\rho_S(\eta)$. Harada (1984) suggested the following model:

$$\rho_S(\eta)=\exp\{-(b\eta)^2\}\{1-2(b\eta)^2\} \tag{3.10}$$

where b is an empirical parameter. Loh (1985, 1988) indicated the following four models:

$$\rho_S(\eta)=\begin{cases}\exp(-a|\eta|)\\ \exp(-a|\eta|^2)\\ \exp(-a|\eta|)\cos(2\pi k_0\eta)\\ \exp(-a|\eta|^2)\cos(2\pi k_0\eta)\end{cases} \tag{3.11}$$

where a and k_0 are parameters to be determined empirically.

Finally, a third approach focuses on the frequency-wave number spectrum (Capon, 1967; Bolt, 1987) which may be used to simulate ground motions and study seismic wave propagation characteristics (e.g., Harada and Shinozuka, 1988, 1989; Yamazaki and Shinozuka, 1988; Deodatis and Shinozuka, 1989).

A number of studies (Kawakami and Sato, 1983; Harada , 1984; Loh, 1985, 1988) discuss differential ground motion characteristics based on stochastic ground motion models. Comparing to these studies, the present study is characterized by establishing

simple and practical time-space varying ground motion spectral models and applying them to estimate both the temporal and spatial maximum relative displacement.

3.3 Basic Presuppositions and Limitations of Proposed Models

The primary objective of this chapter is to establish ground motion spectral models for estimating the maximum relative displacement on the approximately homogeneous ground, which is the most essential and basic condition to consider input ground motions in the seismic design of buried structures. Note that the estimation of relative displacement where spatial heterogeneity, such as ground condition discontinuity exists, is beyond the scope of the present study.

Since attention is focused on the strong motion duration on the nearly homogeneous ground, it may be acceptable to assume the temporal and spatial stationarity of ground motion. Furthermore, it may be considered that ground displacement has a single predominant frequency and this frequency does not vary very much over the points of interest. The adequacy of this assumption will be confirmed with the array observation records in Chapter 4.

Because the relative displacement between two points is defined as the difference of displacement time histories at these points, the relative displacement may also have the same predominant frequency with each displacement. This motivates to propose a ground motion coherence model which estimates a coherence value at the ground motion predominant frequency in Section 3.4.

3.4 Proposed Frequency Independent Coherence Model

Two simple spectral ground motion models are here introduced, and the relationship between these models are discussed. In the first model, a coherence value is estimated at the predominant frequency of ground motion, and it is assumed that the coherence function $\gamma(f,\eta)$ is independent of frequency. Then, Eq.(3.5) can be reduced to

$$S(f,\eta)=S_0(f)\gamma(\eta)\exp\left(-i\frac{2\pi f\eta}{c}\right) \tag{3.12}$$

Let us call this model the "frequency independent coherence model". As seen from Eq.(3.12), this model requires $S_0(f)$, $\gamma(\eta)$ and c to be determined. Once these quantities have been estimated, the resulting spatial correlation function $\rho_S(\eta)$ implied by this model can be found. It is derived below.

From Eq.(3.12), $C(\tau,\eta)$ is obtained by the Wiener-Khinchine relationship as

$$\begin{aligned} C(\tau,\eta) &= \int_{-\infty}^{\infty} S(f,\eta)\exp(i2\pi f\tau)df \\ &= \gamma(\eta)\int_{-\infty}^{\infty} S_0(f)\exp\{i2\pi f(\tau-\eta/c)\}df \end{aligned} \tag{3.13}$$

The auto-covariance function $C_0(\tau)$, which is a counterpart of $S_0(f)$ in the time lag domain, is expressed as

$$C_0(\tau) = \int_{-\infty}^{\infty} S_0(f)\exp(i2\pi f\tau)df \tag{3.14}$$

Combining Eqs.(3.13) and (3.14), $C(\tau,\eta)$ is written as

$$\begin{aligned} C(\tau,\eta) &= C_0(\tau-\eta/c)\gamma(\eta) \\ &= \sigma_a^2\rho_I(\tau-\eta/c)\gamma(\eta) \end{aligned} \tag{3.15}$$

Substituting $\tau=0$ into Eq.(3.15) yields the desired spatial correlation result for this model:

$$\rho_S(\eta) = \rho_I(-\eta/c)\gamma(\eta) \tag{3.16}$$

Eq.(3.16) permits $\rho_S(\eta)$ to be evaluated from the frequency independent coherence model, once $\rho_I(\tau)$, $\gamma(\eta)$ and c have been estimated. In the numerical example shown in Chapter 4, this inferred $\rho_S(\eta)$ is compared with that estimated directly from the data.

3.5 Proposed Time-Space Separable Correlation Model

Let us assume that seismic waves propagate horizontally at the apparent velocity of c, then Eq.(3.1) may be written as

$$C(\tau,\eta)=C_0(\tau-\eta/c)\rho_S(\eta) \tag{3.17}$$

The second model assumes c in Eq.(3.17) to be infinite, then Eq.(3.17) can be reduced to a separable function of time and space as

$$\begin{aligned} C(\tau,\eta)&=C_0(\tau)\rho_S(\eta)\\ &=\sigma_u^2\rho_T(\tau)\rho_S(\eta) \end{aligned} \tag{3.18}$$

where $\rho_T(\tau)$ is the displacement correlation function in time at any fixed spatial location, and $\rho_S(\eta)$ is the correlation function in space at any fixed time. Let us call this model the "time-space separable correlation model". Taking c to be infinite means physically that seismic waves are assumed to propagate vertically to the ground surface. This assumption may be consistent with the shear wave propagation characteristics in horizontally layered soil deposits. It will be shown in Section 4.5 that the apparent propagation velocity of seismic waves can be viewed as essentially infinite over moderate distances.

Since $C_0(\tau)$ links to $S_0(f)$ by Eq.(3.14), this model is completely defined by $\rho_S(\eta)$, and either $C_0(\tau)$ or $S_0(f)$. The advantage of Eq.(3.18) lies in its simplicity. While the frequency independent coherence model required $S_0(f)$, $\gamma(\eta)$ and c, this model requires only $S_0(f)$ and $\rho_S(\eta)$.

3.6 Relative Displacement Covariance Statistics

The relative displacement $d(t,x;\xi)$ between two points with the separation distance ξ is given by

$$d(t,x;\xi)=u(t,\,x+\xi)-u(t,\,x) \tag{3.19}$$

Since $u(t, x)$ is assumed to be a stationary Gaussian time-space process, $d(t,x;\xi)$ is also a Gaussian process with zero mean. For a fixed relative distance ξ, $d(t,x;\xi)$ will vary with both time t and spatial coordinate x. The time-space covariance function of relative displacement $C_d(\tau,\eta;\xi)$ is expressed in terms of the corresponding displacement covariance function as

$$\begin{aligned} C_d(\tau,\eta;\xi) &= \mathrm{E}[d(t+\tau,x+\eta;\xi)d(t,x;\xi)] \\ &= \mathrm{E}[\{u(t+\tau, x+\eta+\xi)-u(t+\tau, x+\eta)\}\{u(t, x+\xi)-u(t, x)\}] \\ &= 2C(\tau,\eta)-C(\tau,\eta+\xi)-C(\tau,\eta-\xi) \end{aligned} \tag{3.20}$$

Eq.(3.20) is completely general in this form. To specialize it to the frequency independent coherence model or time-space separable correlation model, $C(\tau,\eta)$ should be replaced by Eq.(3.15) or Eq.(3.17):

$$C_d(\tau,\eta;\xi)=\sigma_u^2\left\{2\chi(\eta)\rho_T\left(\tau-\frac{\eta}{c}\right)-\chi(\eta+\xi)\rho_T\left(\tau-\frac{\eta+\xi}{c}\right)-\chi(\eta-\xi)\rho_T\left(\tau-\frac{\eta-\xi}{c}\right)\right\}$$

for frequency independent coherence (3.21)

$$C_d(\tau,\eta;\xi)=\sigma_u^2\rho_T(\tau)\{2\rho_S(\eta)-\rho_S(\eta+\xi)-\rho_S(\eta-\xi)\}$$

for time-space separable correlation (3.22)

The mean square value of relative displacement can be obtained by setting $\tau=\eta=0$ in Eq.(3.21) or Eq.(3.22):

$$\sigma_d^2=\sigma_u^2\left\{2-\chi(\xi)\rho_T\left(-\frac{\xi}{c}\right)-\chi(-\xi)\rho_T\left(\frac{\xi}{c}\right)\right\}$$ for frequency independent coherence (3.23)

$$\sigma_d^2=\sigma_u^2\{2-\rho_S(\xi)-\rho_S(-\xi)\}$$ for time-space separable correlation (3.24)

3.7 Maximum Relative Displacement Statistics

Consider a random process with zero mean $X(s)$, where the argument s may be either time or space. The probability that $|X(s)|$ does not exceed level z during an interval B can be estimated as

$$\begin{aligned}\text{Prob}\left[\max_{s\in B}|X(s)|\le z\right] &= \text{Prob}\left[\max_{s\in B} X(s)\le z\right]\times\text{Prob}\left[\min_{s\in B} X(s)\ge -z\right]\\ &=\exp(-\nu_z^+ B)\times\exp(-\nu_{-z}^- B)\\ &=\exp(-2\nu_z^+ B)\end{aligned} \tag{3.25}$$

where ν_z^+ and ν_{-z}^- are the mean rates of up-crossings of level z and down-crossings of $-z$, respectively. Eq.(3.25) is derived from the assumption that the crossings of a specified level occur as a Poisson process. If $X(s)$ is a Gaussian process, ν_z^+ is given by (Vanmarcke, 1983)

$$\nu_z^+=\frac{\exp(-z^2/2\sigma_X^2)}{L_D} \tag{3.26}$$

$$L_D=2\pi\frac{\sigma_X}{\sigma_{X'}} \tag{3.27}$$

in terms of the average interval between zero up-crossings L_D, where σ_X and $\sigma_{X'}$ are the root mean squares of $X(s)$ and its derivative with respect to s, respectively. From Eqs.(3.25) and (3.26), z can be obtained for an arbitrary probability of not being exceeded p as

$$\frac{z}{\sigma_X}=\sqrt{2\ln\left|-\frac{2B}{L_D\ln p}\right|} \tag{3.28}$$

Vanmarcke and Lai (1980) suggested to truncate this result at $z=\sqrt{2}\sigma_X$, the value attained for a sinusoid. The final expression is then

$$\frac{z}{\sigma_X}=\begin{cases}\sqrt{2\ln\left|-\dfrac{2B}{L_D\ln p}\right|} \cdots -\dfrac{2B}{L_D\ln p}\geq e\\ \sqrt{2} \cdots\cdots\cdots\cdots\cdots \text{ otherwise}\end{cases} \tag{3.29}$$

This result for z should be interpreted as the p-fractile of the maximum value of $|X(s)|$ over a temporal or spatial interval B. Similarly, the maximum relative displacement $d_{\max}$ over a temporal or spatial interval B is given by

$$\frac{d_{\max}}{\sigma_d}=\begin{cases}\sqrt{2\ln\left|-\dfrac{2B}{L_D\ln p}\right|} \cdots -\dfrac{2B}{L_D\ln p}\geq e\\ \sqrt{2} \cdots\cdots\cdots\cdots\cdots \text{ otherwise}\end{cases} \tag{3.30}$$

in which σ_d is given by Eq.(3.23) or Eq.(3.24), and L_D is estimated from Eq.(3.27) as (Hino, 1977)

$$L_{DT}=2\pi\sqrt{\left.\frac{C_d(\tau,\eta;\xi)}{-\partial^2 C_d(\tau,\eta;\xi)/\partial\tau^2}\right|_{\tau=\eta=0}} \qquad \text{for temporal maximum} \tag{3.31}$$

$$L_{DS}=2\pi\sqrt{\left.\frac{C_d(\tau,\eta;\xi)}{-\partial^2 C_d(\tau,\eta;\xi)/\partial\eta^2}\right|_{\tau=\eta=0}} \qquad \text{for spatial maximum} \tag{3.32}$$

3.8 Conclusions

The background of stochastic formulation of time-space varying ground motions is summarized, and two new simple ground motion spectral models are here introduced. An advantage of the proposed models is that they can be easily applied to prescribe the time-space covariance function of ground motion, and this covariance function is further applied to the estimation of differential ground motion statistics, which are particularly important from an engineering point of view. The main conclusions of this chapter may be summarized as follows.

1)Two simple ground motion spectral models, i.e., the frequency independent coherence model and the time-space separable correlation model are derived from a standard model of ground motion. The former chooses a coherence function which varies with separation distance, but is independent of frequency. A coherence value estimated at the ground motion predominant frequency is employed as a representative in this model. The latter assumes the apparent horizontal propagation velocity of seismic waves to be infinite, so that the time-space covariance function of ground motion is a separable function of time and space.

2)These models are applied to estimate the maximum relative displacement between two points, using a conventional Poisson arrival process model. Both the temporal maximum over any fixed distance and the spatial maximum at any fixed time can be estimated by the preceding procedure.

4. ANALYSIS OF ARRAY DATA

4.1 General Remarks

The frequency independent coherence model and the time-space separable correlation model established as ground motion spectral models in Chapter 3 are applied to the dense instrument array data recorded at the four sites in Shizuoka Prefecture, Japan. Simple empirical functions are introduced as the temporal correlation, spatial correlation and coherence functions of ground motions. Parameters of these functions are calibrated from the array records by least squares fits.

The apparent propagation velocity of seismic wave is estimated by cross-correlation analysis. The spatial correlation function inferred from the frequency independent coherence model and seismic wave propagation velocity is compared with that in the time-space separable correlation model, which is estimated directly from the observed data.

The root mean square and maximum values of relative displacement are estimated from the two proposed ground motion models, and the results are compared with the observed data. Both the temporal maxima over any fixed distance and the spatial maxima at any fixed time are estimated. The maximum ground strain between two points may be described as dividing the maximum relative displacement by separation distance. The maximum ground strain can be also read from the presenting results.

4.2 Array Observation System

The Public Works Research Institute, Ministry of Construction, Japan is conducting strong motion array observations at five sites in Japan as shown in Fig.4.1, including its Tsukuba campus (Ohkubo et al., 1984; Iwasaki et al., 1986). The array data analyzed here were obtained at the four sites in Shizuoka Prefecture from four earthquakes shown in Table 4.1. Note that all the sites except Yaizu experienced comparable displacement, due to similar magnitude events at similar distances. The motions at Yaizu site are notably stronger. However, the normalized correlation statistics at this site are not anomalous.

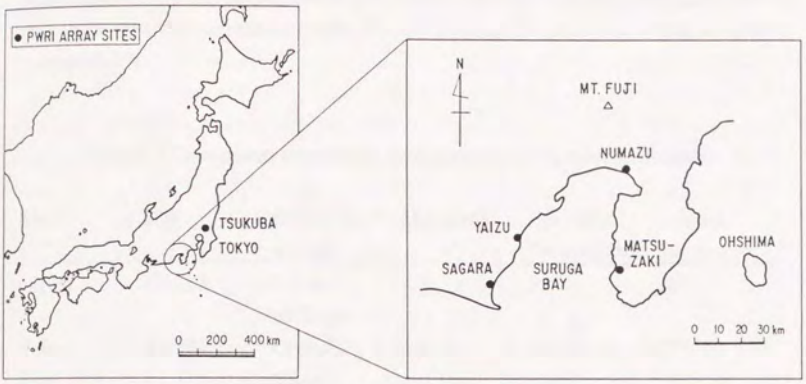

Fig.4.1 Array locations

Table 4.1 Earthquakes analyzed

Site	Date	Epicentral Region	Magnitude	Epicentral Distance[km]	Azimuth [degree]*
Sagara	11/24/83	S Coast of Chubu	5.0	45	277
Yaizu	9/14/84	Central Chubu	6.8	126	327
Numazu	9/5/88	E Yamanashi Prefecture	5.6	45	25
Matsuzaki	11/22/86	Near Izu-Oshima Is.	6.0	72	108

Note: * Clockwise from north

In addition to the four event records, which are listed in Table 4.1, used to calibrate both the frequency independent coherence model and the time-space separable correlation model, another four earthquake records presented in Table 4.2 are employed to calibrate the time-space separable correlation model. Numerical results for these four events are shown in Appendix A.

Table 4.2 Earthquakes analyzed for time-space separable correlation model

Site	Date	Epicentral Region	Magnitude	Epicentral Distance[km]	Azimuth [degree]*
Sagara	3/16/83	S Coast of Chubu	5.7	55	283
Yaizu	9/15/84	Central Chubu	6.2	127	323
Numazu	3/18/88	Tokyo Prefecture	6.0	96	51
Matsuzaki	12/17/87	Kujukuri Coast, Boso	6.7	171	66

Note: * Clockwise from north

The outlines of array deployment at each site are as follows (Tamura, 1984; Iwasaki et al., 1986).

4.2.1 Sagara Site (Arakawa et al., 1982)

Sagara site is located in Sagara Town near Omaezaki. This area is comprised of the lowland of the Hagima River which is covered with soft alluvial clay, surrounding hills and sand dunes along the coast. The base rock of this site is of the Sagara group, tertiary strata consisting of alternating sandy and clayey rocks, which appear very wide around this area with shear velocity of approximately 700 m/s. Considering the geographical features, ten tri-axial 16 bits digital strong motion accelerographs, which are the same accelerographs tested in Chapter 2, are installed on the ground surface along a T-shaped configuration as shown in Fig.4.2. The direction of each leg is selected so that local soil condition varies along a leg. Four down-hole accelerometers are also installed at four stations as deep as 30-36 m so that base rock motions can be recorded. Signals of a down-hole accelerometer is transmitted via cable to a recording unit on the ground surface which has the same specifications with accelerographs installed on the surface. The observation began in 1982.

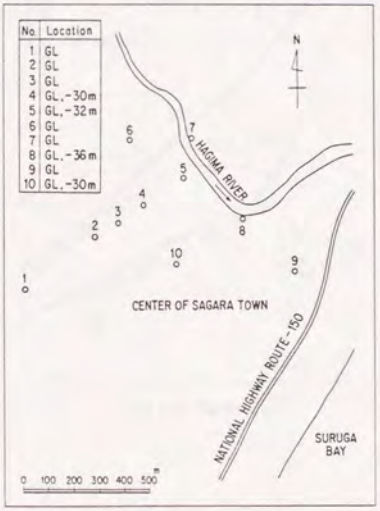

Fig.4.2 Sagara site

4.2.2 Yaizu Site (Arakawa et al., 1983a)

Yaizu site is deployed in the northern part of Yaizu City. This site is widely covered with very soft silty materials on the left bank of the Seto River, whereas the right bank of the river mainly consists of gravel formations. The base rock of this site is Takakusa group, basalt in Neogene period, which appears near the ground surface at station No.1, and is gradually increasing in depth toward the direction of stations Nos.4, 7, 8 and 9. The depth of the base rock at station No.9 is about 110 m below the surface. Twelve accelerographs are installed along a cross-shaped line as illustrated in Fig.4.3. Besides these accelerographs, at station No.9, three down-hole accelerometers are installed at the depths of 30, 63 and 112 m below the surface so as to monitor the amplification of ground motions in soil deposits. The observation began in 1983.

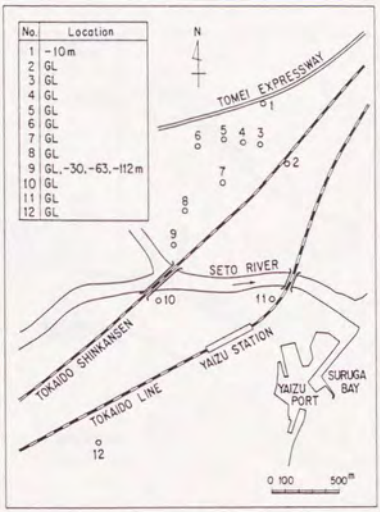

Fig.4.3 Yaizu site

4.2.3 Numazu Site (Arakawa et al., 1984)

Numazu site is located in the western part of Numazu City. The array deploys from the costal dune to the foot of Mt. Ashitaka, crossing the lowlands of Ukishimagahara. It is believed that there used to be a bay shut in by coastal sandbars at the Ukishimagahara, and marshes remained until recently. The surface strata of Ukishimagahara consist of 10-15 m thick organic materials underlain by silt and sand formation. The base rock of this area is tuff breccia. The depth of base rock increases from the foot of Mt. Ashitaka to the costal dune, where it is estimated to be as deep as 150 m below the ground surface. Thirteen accelerographs are installed mainly along the local soil condition varying direction and five down-hole accelerometers are also installed as shown in Fig.4.4. At this site, the most important traffic facilities in Japan, such as National Highway Route-1, Tokaido Line and Shinkansen, go across the array. The observation began in 1984.

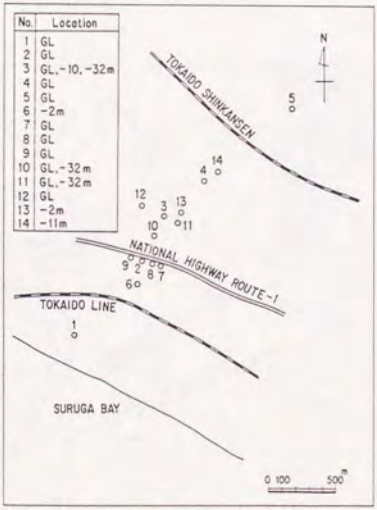

Fig.4.4 Numazu site

4.2.4 Matsuzaki Site (Sasaki et al., 1985)

Matsuzaki site is located in Matsuzaki Town, southwest of the Izu Peninsula. The array deploys from the slope of Mt. Ushibara to the central part of town, where an alluvial fan has been formed by the Naka River. This alluvial fan, approximately 3 km by 1 km, is surrounded by mountains which rise about 200 m above sea level. Eleven accelerographs and four down-hole accelerometers are installed at eleven stations as shown in Fig.4.5. The main line of stations extends from the slope of Mt. Ushibara to the low flats of the alluvial deposits. Five stations are located on the slope, an additional five stations are deployed on the flat and one more reference station is located apart from the main line. The observation began in 1985.

The objective of array observation at this site is to study the effects of local topographical change on ground motion characteristics, whereas the other sites are designated to study local ground condition effects.

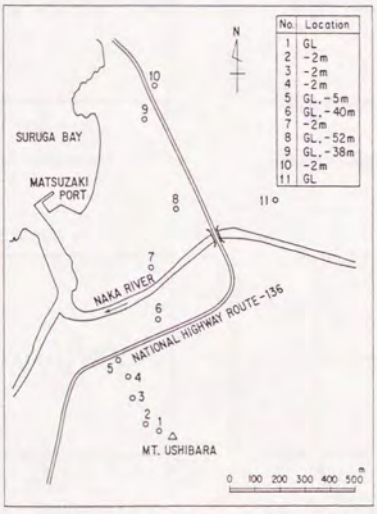

Fig.4.5 Matsuzaki site

4.3 Data Processing

Displacement of ground motion is calculated by integrating the acceleration record in the frequency domain as shown in Section 2.3. Considering that the duration of records for analysis is relatively short, the cut-off frequencies are set up as f_{ll}=1/6, f_{lu}=1/5, f_{ul}=20, f_{uu}=21 [Hz]. Since the original acceleration time histories are recorded along north-south and east-west directions, radial and transverse components of displacement are calculated by rotating the coordinates. Fig.4.6 shows an example of displacement time histories. These records are obtained at two stations at a distance of 250 m. Note that both the amplitude and phase characteristics of the two wave forms look considerably similar.

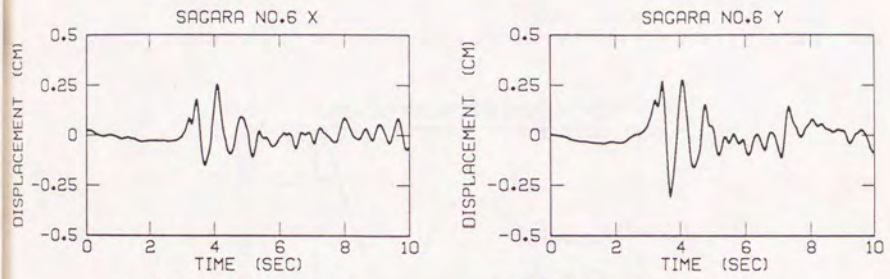

(a) No.6, radial component

(b) No.6, transverse component

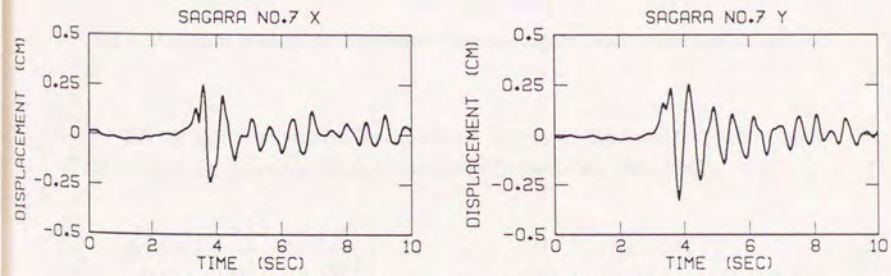

(c) No.7, radial component

(d) No.7, transverse component

Fig.4.6 Example of displacement time histories (Sagara)

4.4 Temporal and Spatial Correlation Functions

The following function is assumed to represent the temporal correlation function (auto-correlation function) of ground displacement (Tamura et al., 1990, 1991):

$$\rho_T(\tau)=\frac{\cos(2\pi\tau/T_0)}{(2\pi\alpha\tau/T_0)^2+1} \tag{4.1}$$

where T_0 and α are determined by least squares fit to the temporal correlation function calculated from the displacement data. An example of least squares fits is shown in Fig.4.7. The solid and dashed lines correspond to temporal correlation functions calculated from the observed data and Eq.(4.1), respectively.

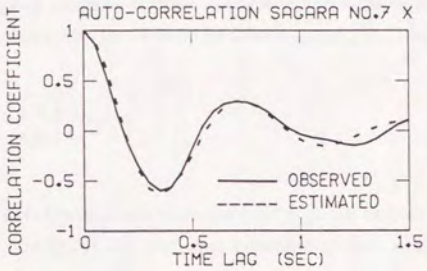

Fig.4.7 Example of temporal correlation function (Sagara, No.7, radial component)

For the spatial correlation function in the time-space separable correlation model (TSSC model), the following function is adopted (Tamura et al., 1990, 1991):

$$\rho_S(\eta)=\left\{1-\left(\frac{\eta}{\xi_0}\right)^2\right\}\exp\left\{-\left(\frac{\eta}{\xi_0}\right)^2\right\} \tag{4.2}$$

where ξ_0 is determined by least squares fit to the spatial correlation coefficients calculated from displacement records. The transverse component data at the Yaizu site with a separation distance longer than 600 m, are ignored for this least squares fit because its correlations seem unusually high compared with its radial component.

Fig.4.8 compares the least squares fit spatial correlation function indicated by solid line and correlation coefficients calculated from the observed data. The dashed line in Fig.4.8 shows the spatial correlation function inferred from the frequency independent coherence model (FIC model), which will be mentioned in Section 4.5. The separation distance in Fig.4.8 is the distance between two points projected to the radial direction. It can be seen from Fig.4.8 that Eq.(4.2) gives good approximation of ground motion spatial correlation, though the observed data show certain scatter.

$\rho_S(\eta)$ is nearly 0 for $\eta>\xi_0$, which physically means that the ground motion data recorded at locations with this separation range may be considered independent.

The mean square value of relative displacement estimated from the time-space separable correlation model can be obtained by substituting Eq.(4.2) into Eq.(3.24) as

$$\sigma_d^2=2\sigma_u^2\left[1-\left\{1-\left(\frac{\xi}{\xi_0}\right)^2\right\}\exp\left\{-\left(\frac{\xi}{\xi_0}\right)^2\right\}\right] \tag{4.3}$$

The covariance function of relative displacement $C_d(\tau,\eta;\xi)$ can be obtained by substituting Eqs.(4.1) and (4.2) into Eq.(3.22), and then substituting this result into Eq.(3.31) or Eq.(3.32) yields:

$$L_{DT}=\frac{T_0}{\sqrt{1+2\alpha^2}} \qquad \text{for temporal interval} \tag{4.4}$$

$$L_{DS}=2\pi\xi_0\sqrt{\frac{1-(1-X^2)\exp(-X^2)}{2\{2-(2X^4-7X^2+2)\exp(-X^2)\}}};\ X=\frac{\xi}{\xi_0}$$

for spatial interval (4.5)

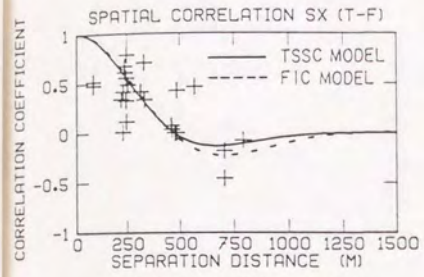

(a) Sagara, radial component

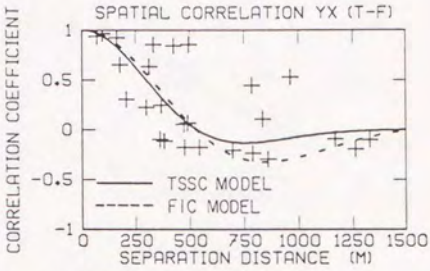

(b) Yaizu, radial component

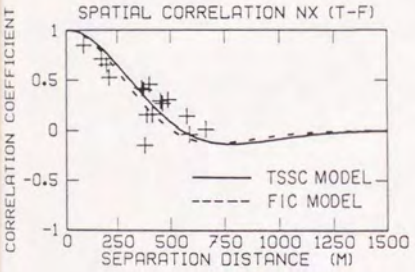

(c) Numazu, radial component

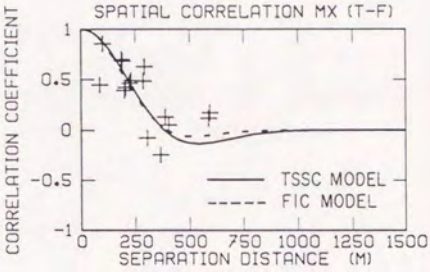

(d) Matsuzaki, radial component

Fig.4.8(1) Spatial correlation function

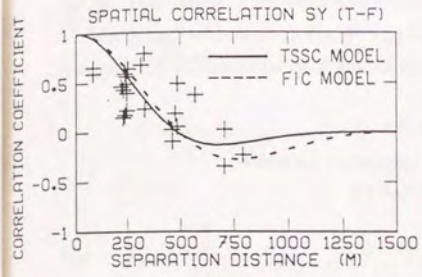

(e) Sagara, transverse component

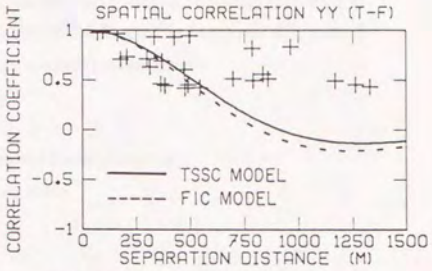

(f) Yaizu, transverse component

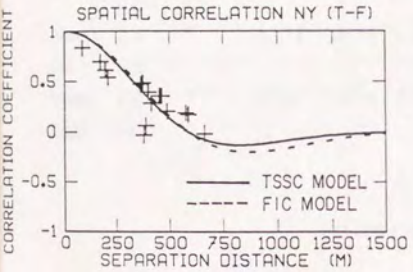

(g) Numazu, transverse component

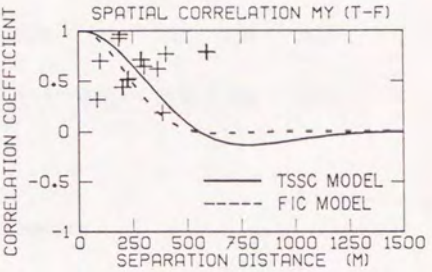

(h) Matsuzaki, transverse component

Fig.4.8(2) Spatial correlation function

Table 4.3 shows the parameters of temporal and spatial correlation functions. Besides these parameters, the maximum ground displacement u_{max} and the root mean square value of displacement σ_u for each site are also shown in the same table. u_{max} and σ_u are the mean values of the maximum displacements and root mean square displacements at stations in each site, respectively. B_T and B_S in Table 4.3 indicate the temporal and spatial intervals in which stationarity of ground motion is assumed, respectively.

Table 4.3 Parameters of ground motion models

(a) Radial component

Site	B_T [sec]	N*	u_{max} [cm]	σ_u [cm]	T_0 [sec]	α	ξ_0 [m]	B_S [m]	a_0 [m]	c [m/s]
Saga-ra	3.0-8.5	8	0.239	.0792	0.70	0.25	470	1000	760	2635
Yaizu	1.0-9.0	8	0.937	.4145	1.65	0.15	530	2000	960	1276
Numa-zu	2.5-8.5	7	0.171	.0675	0.80	0.30	550	1500	650	2526
Matsu-zaki	7.0-13.0	7	0.193	.0816	1.00	0.15	380	1000	370	1573

(b) Transverse component

Site	B_T [sec]	N*	u_{max} [cm]	σ_u [cm]	T_0 [sec]	α	ξ_0 [m]	B_S [m]	a_0 [m]	c [m/s]
Saga-ra	3.0-8.5	8	0.298	.0951	0.70	0.15	480	1000	810	2798
Yaizu	7.0-15.0	8	1.141	.5278	2.00	0.30	910	2000	1370	1632
Numa-zu	2.5-8.5	7	0.260	.0793	0.85	0.20	580	1500	860	2740
Matsu-zaki	7.0-13.0	7	0.202	.1001	1.10	0.15	550	1000	380	1920

Note: * Number of stations

4.5 Spatial Coherence and Propagation Velocity of Seismic Wave

Fig.4.9 shows an example of power spectra. It can be seen that most of the power is concentrated in a relatively narrow band. The predominant frequencies of the power spectra do not vary very much among the stations in each site. Fig.4.10 shows an example of coherence functions. A Hamming spectral window with Δf=0.098 [Hz] is employed for smoothing (Ohsaki, 1976) and the number of smoothing is taken as 5, 10 and 20, respectively. Note that coherence variation with frequency seems somewhat sensitive to data smoothing.

The following frequency independent function is adopted to represent coherence decay with separation (Tamura et al., 1990, 1991):

$$\gamma(\eta)=\exp\left\{-\left(\frac{\eta}{a_0}\right)^2\right\} \tag{4.6}$$

where a_0 is determined by least squares fit. Fig.4.11 shows the comparison of the least squares fit function and coherence calculated from the observed data, where coherence is calculated for the predominant frequency of ground motions, and the number of smoothing is taken as 10. The parameter a_0 is shown in Table 4.3 for each site.

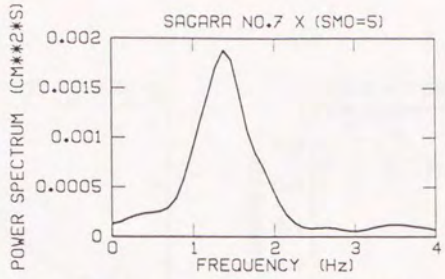

Fig.4.9 Example of power spectrum (Sagara, No.7, radial component)

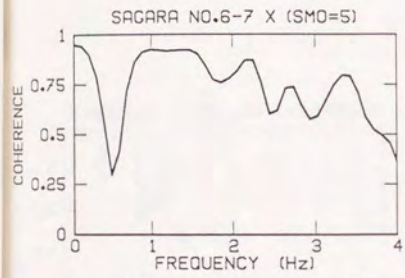

(a) Number of smoothing=5

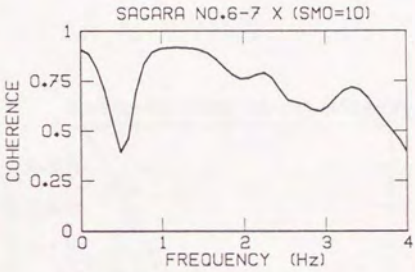

(b) Number of smoothing=10

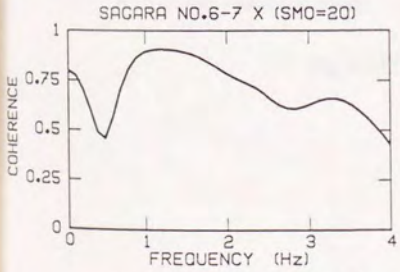

(c) Number of smoothing=20

Fig.4.10 Example of coherence (Sagara, Nos.6-7, radial component)

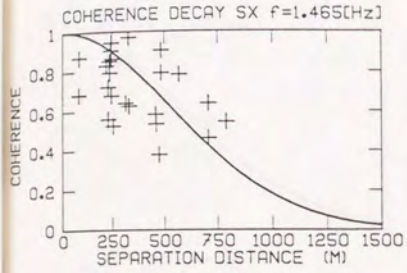

(a) Sagara, radial component

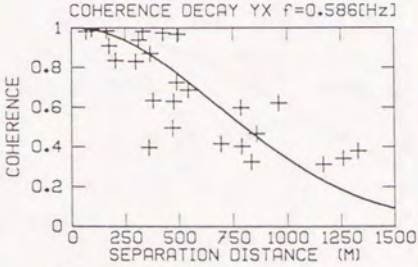

(b) Yaizu, radial component

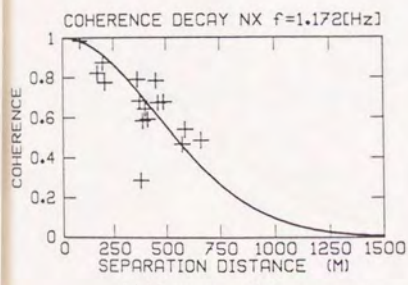

(c) Numazu, radial component

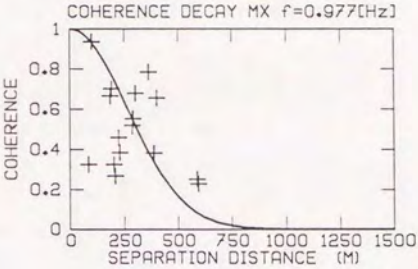

(d) Matsuzaki, radial component

Fig.4.11(1) Coherence decay

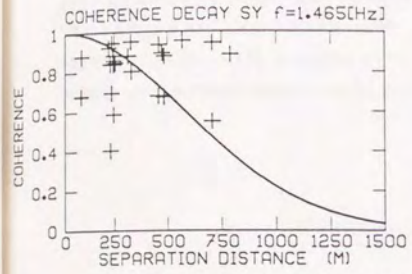

(e) Sagara, transverse component

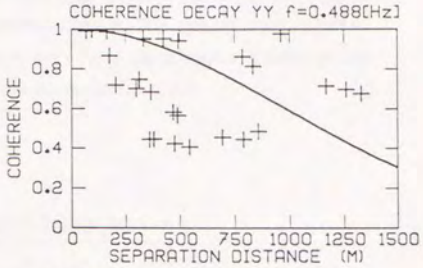

(f) Yaizu, transverse component

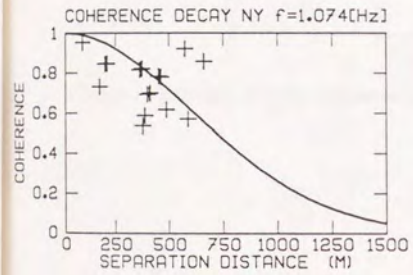

(g) Numazu, transverse component

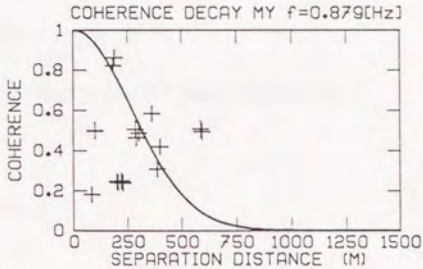

(h) Matsuzaki, transverse component

Fig.4.11(2) Coherence decay

Propagation velocity of seismic wave is calculated by cross-correlation analysis (Sasaki et al., 1988b). An example of cross-correlation functions is shown in Fig.4.12. Fig.4.13 shows the relationship between separation distance of stations and time lag at which cross-correlation function takes its maximum value. The apparent propagation velocity, c in Eq.(3.12), is estimated by least squares fit to these points. Values of the seismic wave propagation velocity for each site are shown in Table 4.3.

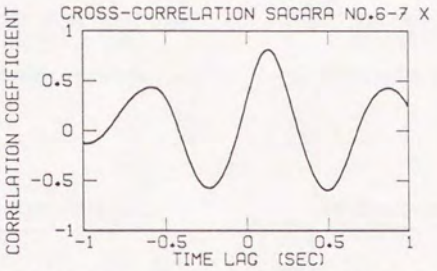

Fig.4.12 Example of cross-correlation function (Sagara, Nos.6-7, radial component)

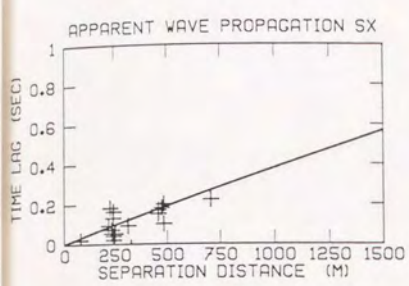

(a) Sagara, radial component

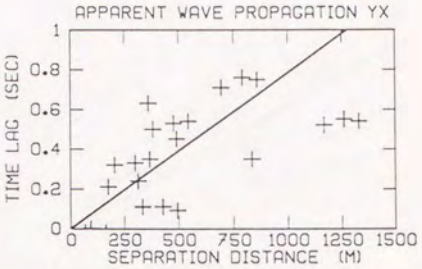

(b) Yaizu, radial component

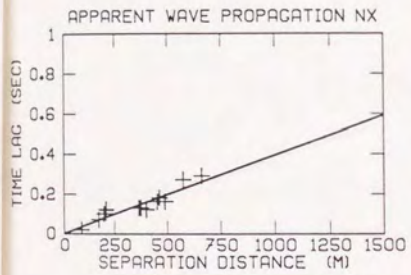

(c) Numazu, radial component

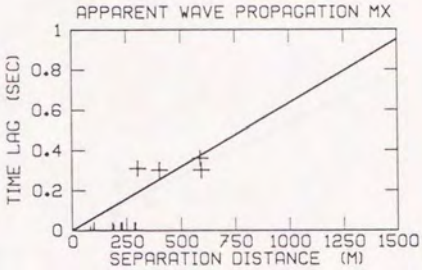

(d) Matsuzaki, radial component

Fig.4.13(1) Apparent propagation of seismic wave

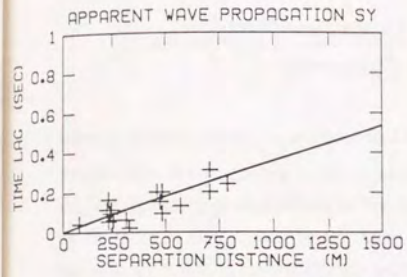

(e) Sagara, transverse component

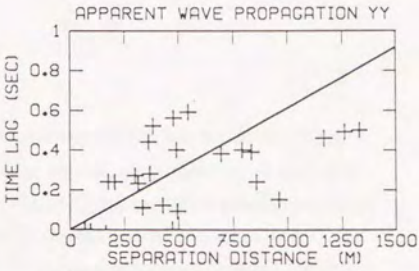

(f) Yaizu, transverse component

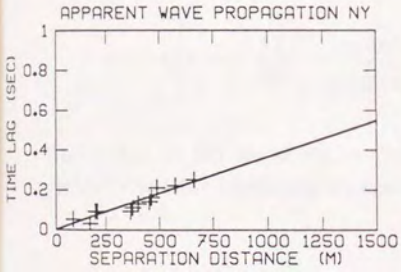

(g) Numazu, transverse component

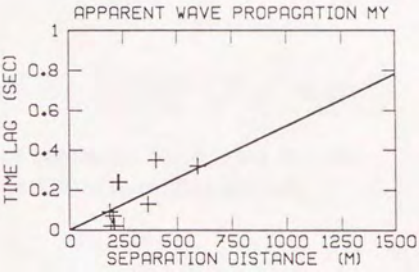

(h) Matsuzaki, transverse component

Fig.4.13(2) Apparent propagation of seismic wave

Substituting Eqs.(4.1) and (4.6) into Eq.(3.16), the inferred spatial correlation function can be estimated from coherence as

$$\rho_S(\eta)=\exp\left\{-\left(\frac{\eta}{a_0}\right)^2\right\}\frac{\cos(2\pi\eta/cT_0)}{(2\pi\alpha\eta/cT_0)^2+1} \tag{4.7}$$

where c is the apparent propagation velocity of seismic wave. Note that this choice of $\rho_S(\eta)$ results from the frequency independent coherence model, using fitted $\rho_I(\tau)$ and $\gamma(\eta)$. Eq.(4.7) is shown as dashed line in Fig.4.8. The directly fitted spatial correlation function by Eq.(4.2) is also shown in the same figure. Comparing these results, Eq.(4.7) and Eq.(4.2) are found to coincide fairly well. This shows good agreement between the time-space separable correlation model and the frequency independent coherence model.

The mean square value of relative displacement evaluated from the frequency independent coherence model is given by substituting Eqs.(4.1) and (4.6) into Eq.(3.23) as

$$\sigma_d^2=2\sigma_u^2\left[1-\exp\left\{-\left(\frac{\xi}{a_0}\right)^2\right\}\frac{\cos(2\pi\xi/cT_0)}{(2\pi\alpha\xi/cT_0)^2+1}\right] \tag{4.8}$$

L_{DT} or L_{DS} for this model can be obtained by substituting Eqs.(4.1) and (4.6) into Eq.(3.22), and then substituting this result into Eq.(3.31) or Eq.(3.32), respectively.

4.6 Maximum Relative Displacement

When the time-space separable correlation model is adopted, the temporal maximum relative displacement over the strong motion duration can be obtained by combining Eqs.(3.30), (4.3) and (4.4). The spatial maximum relative displacement at any fixed time can be estimated by combining Eqs.(3.30), (4.3) and (4.5). Similarly, when the frequency independent coherence model is chosen, the temporal or spatial maximum relative displacement can be obtained by substituting the corresponding σ_d, and either L_{DT} or L_{DS} into Eq.(3.30).

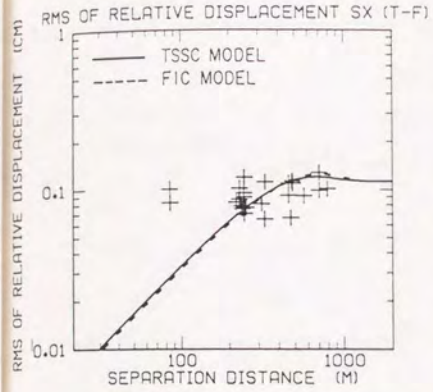

(a) Sagara, radial component

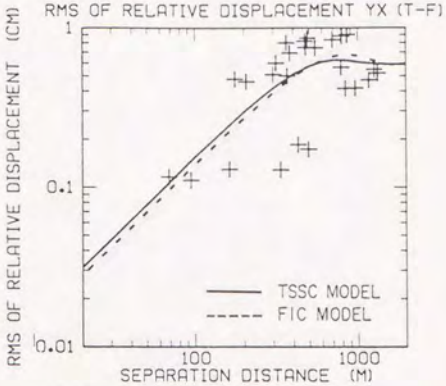

(b) Yaizu, radial component

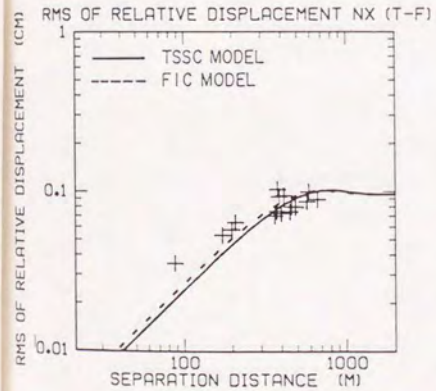

(c) Numazu, radial component

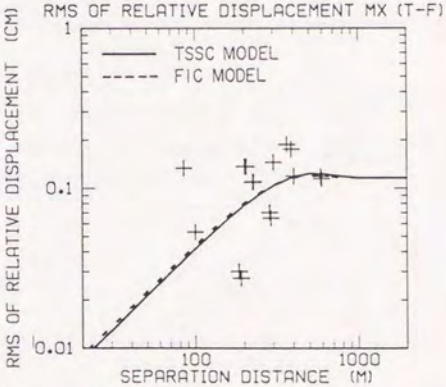

(d) Matsuzaki, radial component

Fig.4.14(1) RMS of relative displacement

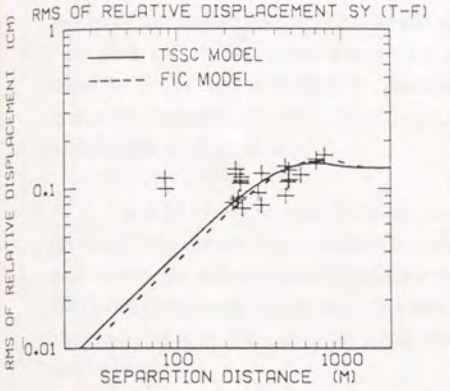

(e) Sagara, transverse component

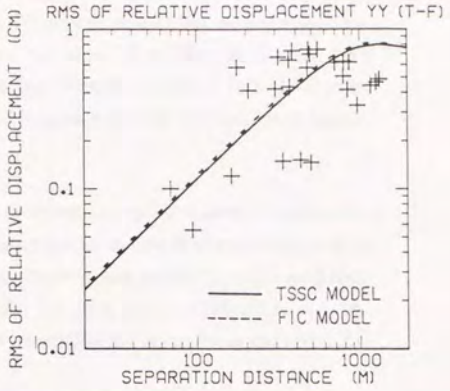

(f) Yaizu, transverse component

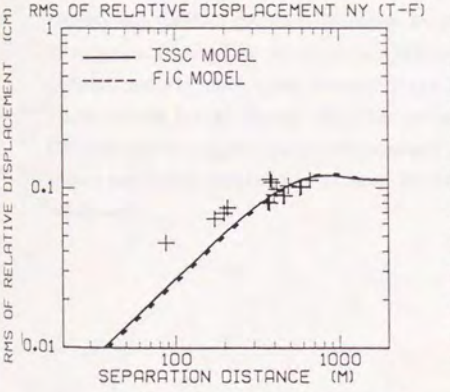

(g) Numazu, transverse component

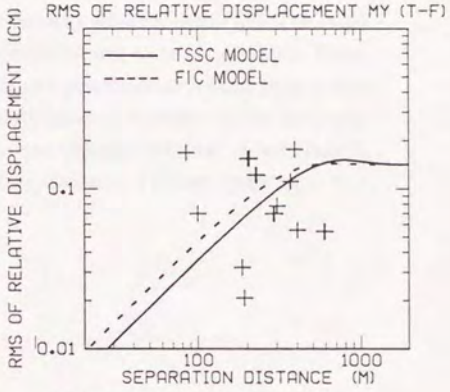

(h) Matsuzaki, transverse component

Fig.4.14(2) RMS of relative displacement

Fig.4.14 shows the comparison of the root mean square value of relative displacement σ_d estimated from the time-space separable correlation model (Eq.(4.3)), frequency independent coherence model (Eq.(4.8)) and calculated from the observed data. The solid and dashed lines indicate values estimated from Eqs.(4.3) and (4.8), respectively. As seen from Fig.4.14, σ_d calculated from the observed data show some scatter, the estimated value from Eqs.(4.3) and (4.8) agree quite well and are almost located in the middle of observed data.

Fig.4.15 compares peak factors of the temporal maximum relative displacement estimated from the time-space separable correlation model and the frequency independent coherence model with values calculated from the observed data, where the solid and dashed lines correspond to the former and latter models. The peak factor is defined as d_{max}/σ_d, which appears at the left side of Eq.(3.30), and the probability of not being exceeded p is taken as 0.5.

Fig.4.16 shows the peak factor calculated from both the time-space separable correlation model and the observed data. The solid line corresponds to p=0.5, and dashed lines correspond to p=0.84 and 0.16. The range between the two dashed lines indicates roughly one standard deviation dispersion from the mean value consistent with a Gaussian distribution. Most of the observed data fall between the two dashed lines for the Yaizu, Numazu and Matsuzaki sites, however, it can be seen that the observed data show a little higher values for the Sagara site. This underestimation of extremes by the stationary Gaussian model suggests either nonstationary or non-Gaussian behavior, or both. Indeed, somewhat better agreement has been found by choosing different "stationary time windows".

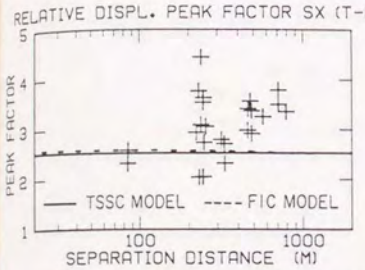

(a) Sagara, radial component

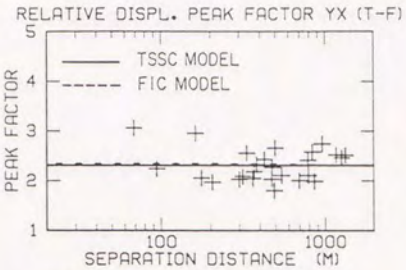

(b) Yaizu, radial component

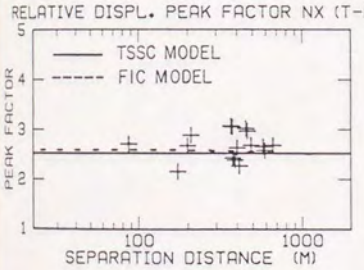

(c) Numazu, radial component

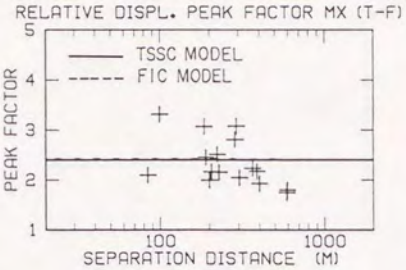

(d) Matsuzaki, radial component

Fig.4.15(1) Peak factor of temporal maximum relative displacement (p=0.5)

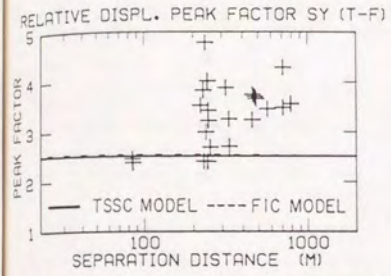

(e) Sagara, transverse component

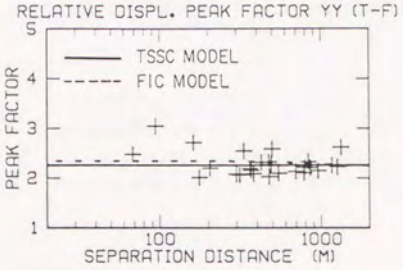

(f) Yaizu, transverse component

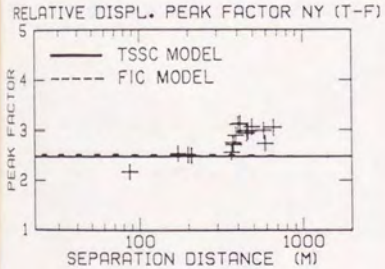

(g) Numazu, transverse component

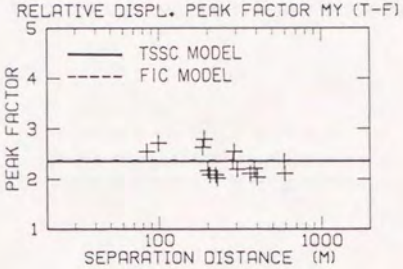

(h) Matsuzaki, transverse component

Fig.4.15(2) Peak factor of temporal maximum relative displacement (p=0.5)

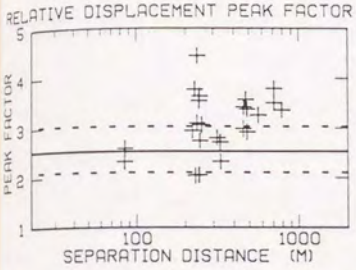

(a) Sagara, radial component

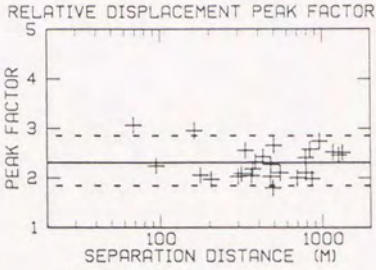

(b) Yaizu, radial component

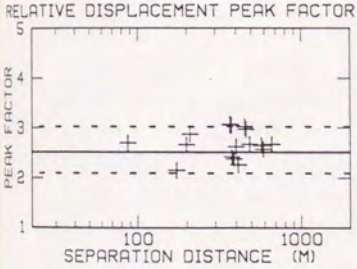

(c) Numazu, radial component

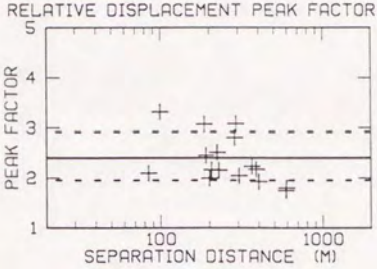

(d) Matsuzaki, radial component

Fig.4.16(1) Peak factor of temporal maximum relative displacement estimated from time-space separable correlation model (p=0.84, 0.5, 0.16)

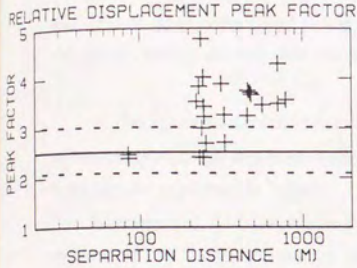

(e) Sagara, transverse component

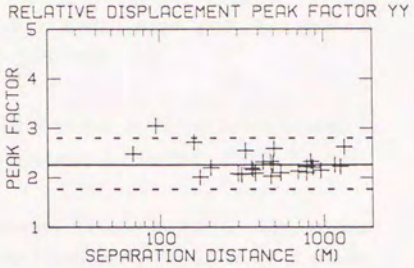

(f) Yaizu, transverse component

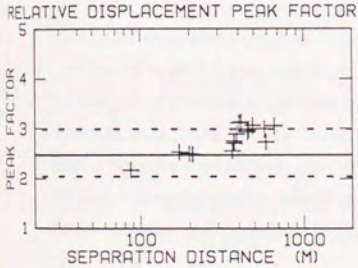

(g) Numazu, transverse component

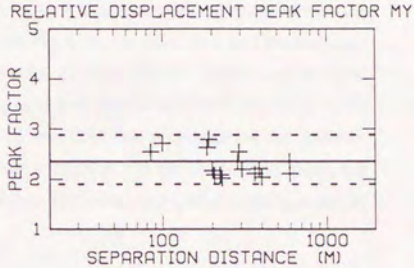

(h) Matsuzaki, transverse component

Fig.4.16(2) Peak factor of temporal maximum relative displacement estimated from time-space separable correlation model (p=0.84, 0.5, 0.16)

Fig.4.17 compares the temporal maximum relative displacement between any fixed locations estimated from the time-space separable correlation model and the frequency independent coherence model, where only the median level (p=0.5) is shown. The solid and dashed lines correspond to the former and latter models, respectively. As seen from this figure, the results from the two models agree fairly well.

The maximum relative displacement d_{max} increases, as the separation distance ξ increases up to $\xi=\xi_0$, and then it takes almost a constant value for $\xi>\xi_0$. Physically, these facts may be explained as follows:
For the range of $\xi\leq\xi_0$, according as the separation distance becomes longer, ground motions at two locations become less correlated, consequently the difference of ground motions, i.e., relative displacement becomes larger. However, as for the range of $\xi>\xi_0$, the ground motions at two locations may be considered independent, therefore the degree of difference between these two ground motions does not depend on the separation distance.

Fig.4.18 shows the temporal maximum relative displacement estimated from the time-space separable correlation model. Similar to Fig.4.16, the solid line and dashed lines correspond to p=0.5 and p=0.84, 0.16, respectively. Though certain scatter can be seen, the theoretical formula of maximum relative displacement agrees well with the trend of the observed data. Note that the range between 0.16 and 0.84 fractiles appears too narrow. This is because they include only random process uncertainty in the Gaussian model, not the gross uncertainty in the model and its parameters. Temporal and spatial heterogeneity of the records may also contribute to this scatter.

The maximum ground strain between two points can be described as

$$\varepsilon_{max}=d_{max}/\xi \tag{4.9}$$

where ξ is the separation distance between two points. Since the temporal maximum relative displacement is the maximum difference of two ground motions at any fixed locations in time, the maximum ground strain here defined should be considered as an average ground strain over the fixed distance. For example, the maximum ground strain over a distance of 100 m is calculated as a certain value, however the local ground stain for a shorter separation which is a part of this 100 m distance can be larger or smaller than the maximum value for the 100 m.

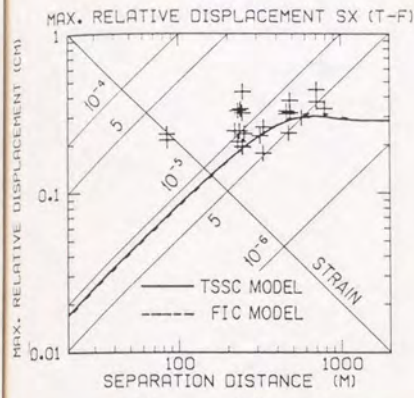

(a) Sagara, radial component

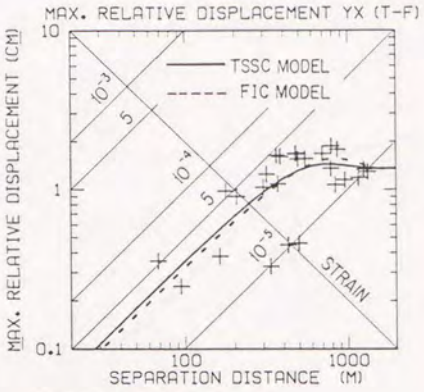

(b) Yaizu, radial component

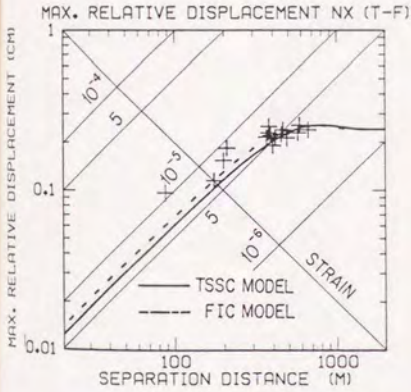

(c) Numazu, radial component

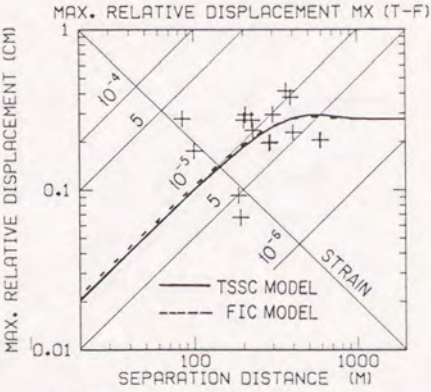

(d) Matsuzaki, radial component

Fig.4.17(1) Temporal maximum relative displacement (p=0.5)

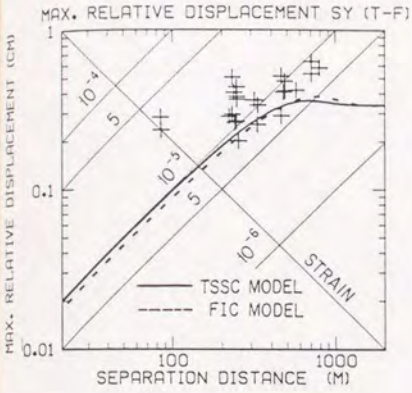

(e) Sagara, transverse component

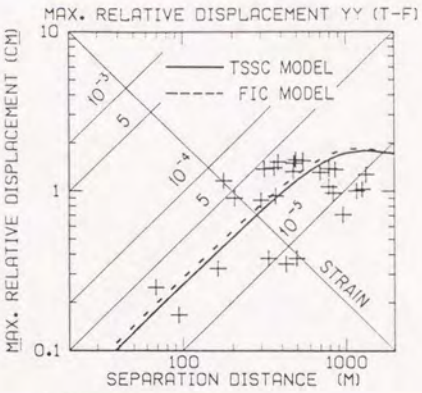

(f) Yaizu, transverse component

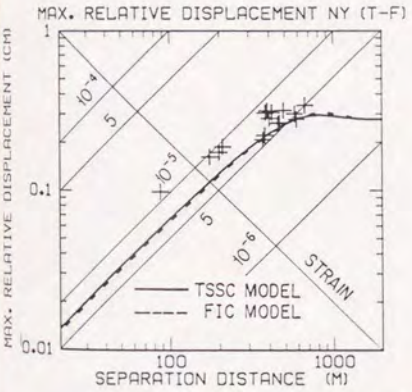

(g) Numazu, transverse component

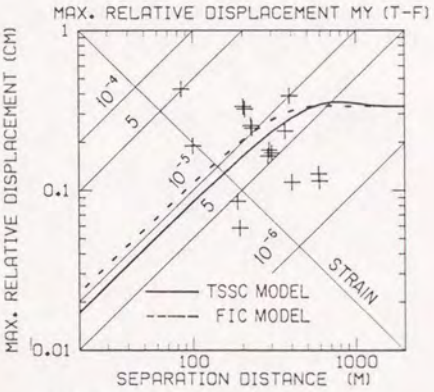

(h) Matsuzaki, transverse component

Fig.4.17(2) Temporal maximum relative displacement (p=0.5)

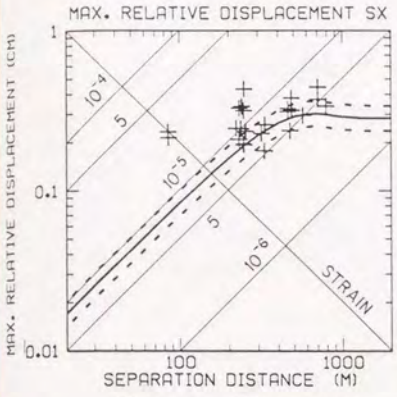

(a) Sagara, radial component

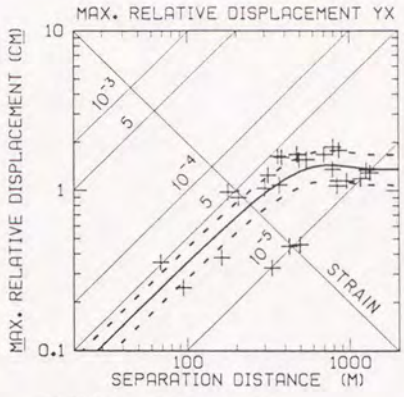

(b) Yaizu, radial component

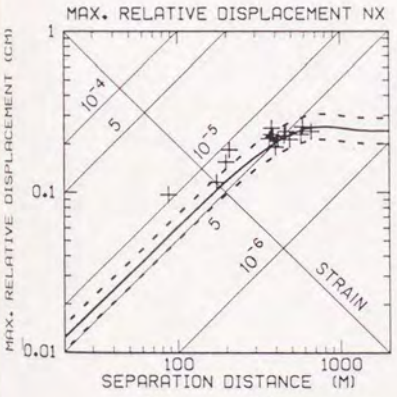

(c) Numazu, radial component

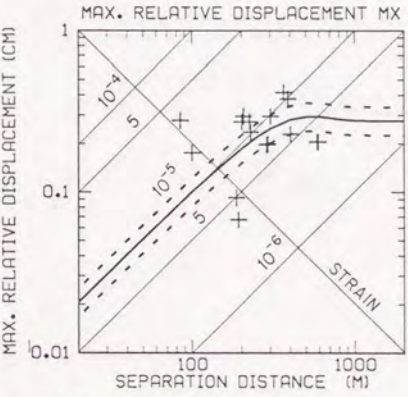

(d) Matsuzaki, radial component

Fig.4.18(1) Temporal maximum relative displacement estimated from time-space separable correlation model (p=0.84, 0.5, 0.16)

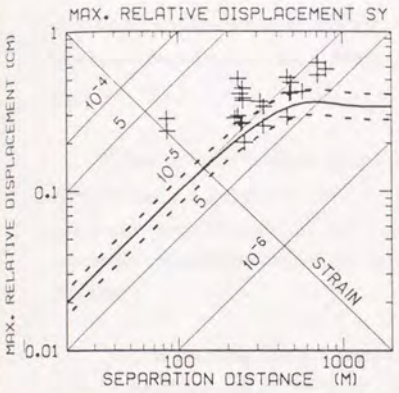

(e) Sagara, transverse component

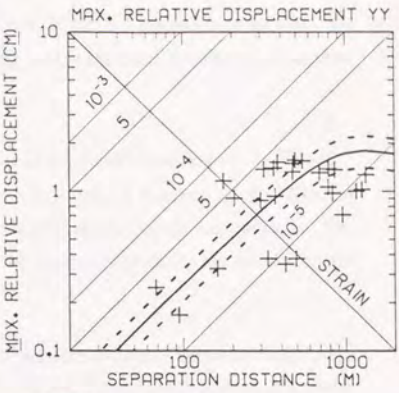

(f) Yaizu, transverse component

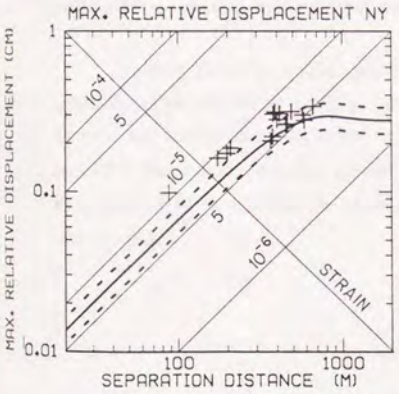

(g) Numazu, transverse component

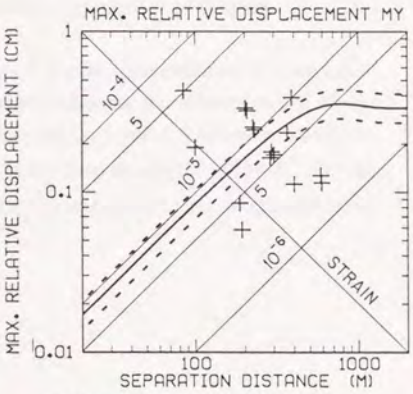

(h) Matsuzaki, transverse component

Fig.4.18(2) Temporal maximum relative displacement estimated from time-space separable correlation model (p=0.84, 0.5, 0.16)

From the definition by Eq.(4.9), the maximum ground strain can be read from the axes which go up from left to right with 45 degrees in Fig.4.17 or Fig.4.18. As seen from these figures, the maximum relative displacement is almost proportional to the separation distance for $\xi \leq \xi_0$, and it takes nearly a constant value for $\xi > \xi_0$. This fact indicates that the maximum ground strain is almost constant for $\xi \leq \xi_0$, and it becomes smaller as ξ becomes large for $\xi > \xi_0$.

The maximum temporal ground strains over an any fixed distance are $(25–35)\times10^{-6}$ for the Yaizu site and $(6–10)\times10^{-6}$ for the other sites, when p is taken as 0.5. Ground strains are also estimated by finite element analysis as shown in Appendix B. The maximum values here obtained are consistent with those estimated by the finite element procedure.

As for the array data analyzed here, the separation distances between stations are mostly greater than 100 m. The array data recorded at the Public Works Research Institute (PWRI) campus in Tsukuba, Japan, where the separation distance of monitoring points is 50 m, is employed to estimate ground strains by finite element method. Detailed results are presented in Appendix C. The results of the PWRI campus data analysis will be cited in Section 5.5 to supplement the ground strain characteristics over a short distance.

Fig.4.19 shows the spatial maximum relative displacement estimated from the time-space separable correlation model and the frequency independent coherence model, where the solid and dashed lines correspond to the former and latter model. The results shown are for p=0.5. The maximum spatial ground strains at any fixed time are $(20–30)\times10^{-6}$ for the Yaizu site and $(4–7)\times10^{-6}$ for the other sites, when the probability of not being exceeded is taken as 0.5.

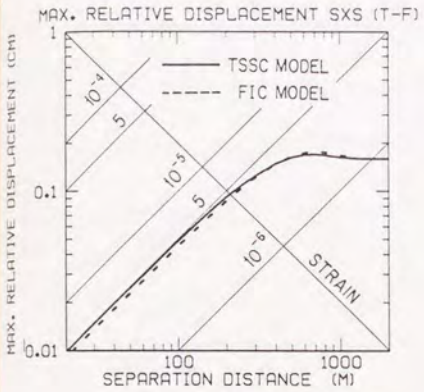

(a) Sagara, radial component

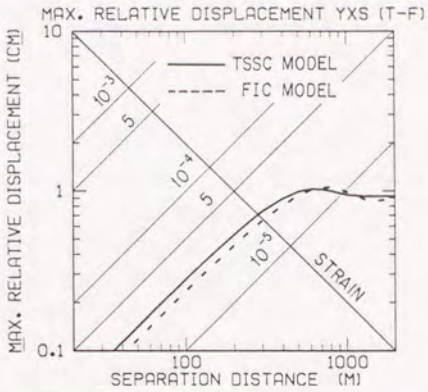

(b) Yaizu, radial component

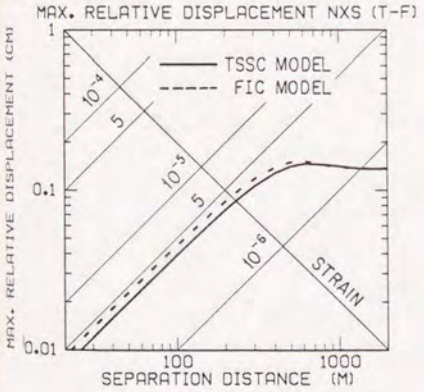

(c) Numazu, radial component

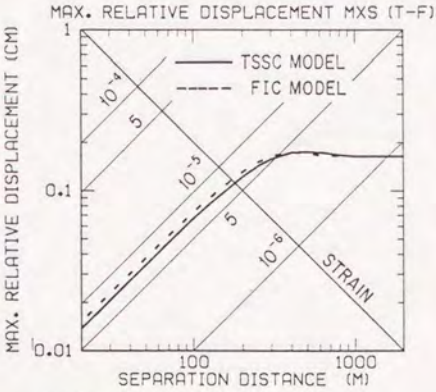

(d) Matsuzaki, radial component

Fig.4.19(1) Spatial maximum relative displacement (p=0.5)

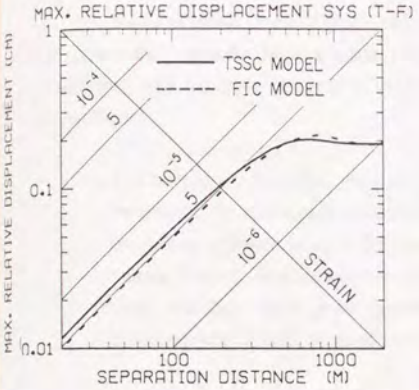

(e) Sagara, transverse component

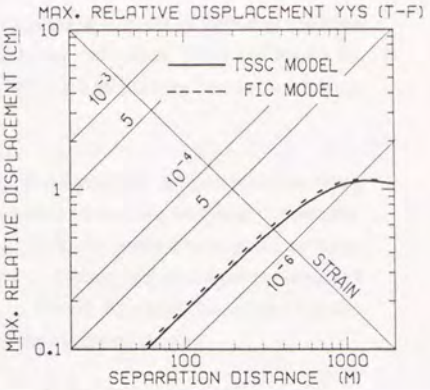

(f) Yaizu, transverse component

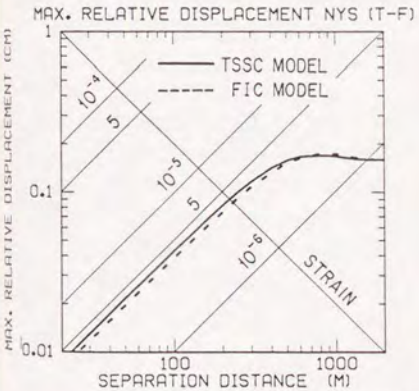

(g) Numazu, transverse component

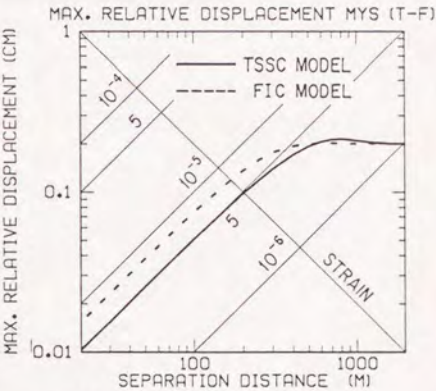

(h) Matsuzaki, transverse component

Fig.4.19(2) Spatial maximum relative displacement (p=0.5)

4.7 Conclusions

Two stochastic ground motion models are applied to estimate the maximum relative displacement over a temporal or spatial interval between two points. Numerical results are calibrated with the array observation data. The following points may be concluded from this chapter.

1) The proposed ground motion models, the frequency independent coherence model and the time-space separable correlation model, can be useful engineering models to estimate relative displacement, both root mean square and maximum values. The numerical results are compared with those calculated from the observed data, and they show good agreement. It should be noted, however, that the observed data exhibit certain scatter around the estimated values.

2) Little difference exists between the frequency independent coherence model and the time-space separable correlation model, once the spatial coherence function and the apparent propagation velocity of seismic wave in the former model, and the spatial correlation function in the latter model are suitably estimated.

5. GROUND STRAIN ESTIMATION USING THE TIME-SPACE SEPARABLE CORRELATION MODEL

5.1 General Remarks

The frequency independent coherence model and the time-space separable correlation model were established as ground motion spectral models and applied to estimate the maximum relative displacement between two points in the previous chapters. They are calibrated from the array observation data and show good agreement with the observed data. According to these results, little difference exists between relative displacement statistics estimated from the proposed two ground motion models.

In the time-space separable correlation model, the time-space covariance function is expressed as the product of the mean square value of displacement, the temporal correlation function at any fixed spatial location and the spatial correlation function at any fixed time. An advantage of this model is that conventional independent strong motion records can be incorporated into estimating the mean square value and temporal correlation function of ground displacement.

Taking this advantage into account, 197 sets of two horizontal strong motion records obtained in Japan by SMAC accelerographs are employed to assess the root mean square (RMS) displacement and temporal correlation function. An attenuation equation of RMS displacement in terms of earthquake magnitude and epicentral distance is presented by multiple regression analysis. The temporal correlation function of displacement is calibrated from the same data set. The spatial correlation function of displacement is calibrated from the eight events data recorded at the four array observation sites in Shizuoka Prefecture, Japan.

The maximum relative displacement is estimated by using a Poisson process model of extremes as shown in Chapter 3. Note that the discussion in this chapter is limited to the temporal maxima, which are usually of interest in design practice, and are easily calibrated from actual records. However, the spatial maxima can be estimated similarly. Results are compared with the array observation records, and examples of predicted maximum relative

displacement are shown for several combinations of earthquake magnitude and epicentral distance.

The maximum ground strains are derived from the maximum relative displacement, and their attenuation characteristics with epicentral distance are compared with the observed ground strain and pipe strain data. The ground strains estimated from array observation records by finite element analysis are also employed for comparison of the ground strain attenuation.

5.2 RMS Displacement and Strong Motion Duration

The RMS value of a stationary process with zero mean $u(t)$ may be estimated by Eq.(3.4). When Eq.(3.4) is applied to a ground motion time history with finite duration, it is necessary to define strong motion duration for which stationarity is assumed and the RMS value is calculated. Various studies on the definition of strong motion duration have been made (Bolt, 1973; Trifunac and Brady, 1975; Vanmarcke and Lai, 1980; McCann, 1980; Kawashima et al., 1985b). Among them, the definition by Trifunac and Brady (1975) is adopted in this study. Their definition corresponds to the 5% to 95% of the integral of a squared time history. The lower and upper bounds of this integral seem to be somewhat arbitrary, however it may be acceptable at present to assume ground motion stationarity over certain strong motion duration (Hoshiya et al., 1987). RMS value studied in the following analysis is calculated for this duration.

Table 5.1 Classification of soil conditions

Soil Condition	Natural Period Range [sec]	Geological Feature	Number of Sites	Number of Records
Group-1	$T_G<0.2$	Tertiary or Older	19	46
Group-2	$0.2\leq T_G<0.6$	Alluvium and Diluvium	31	107
Group-3	$0.6\leq T_G$	Soft Alluvium	17	44

197 sets of two horizontal components of strong motion data are considered in this study. They were recorded at 67 free filed sites in Japan from earthquakes with magnitudes ranging from 5.0 to 7.9 (Kawashima et al., 1985a). The soil conditions at the recording sites are classified into three groups according to the natural period of ground T_G as shown in Table 5.1. This classification depends on the earthquake resistant design specifications for highway bridges in Japan (Japan Road Association, 1990). All the data analyzed were obtained by the SMAC accelerographs. The ground displacement is calculated by integrating acceleration record in the frequency domain (Goto et al., 1978). Considering the SMAC accelerograph record reliability (Kawashima et al., 1982a, 1982b), the lower and upper cut-off frequencies for filtering are taken as 1/3 Hz and 12 Hz, respectively.

Two horizontal orthogonal components of ground displacement are combined to give a motion along an arbitrary direction (Kawashima et al., 1983). RMS displacement is calculated for every 5 degrees, and the maximum RMS displacement on the horizontal plane and the corresponding strong motion duration is obtained. Besides the RMS value, the temporal correlation function which will be mentioned in the following section, is also calibrated for the same duration of ground motion along the same direction.

Referring to the attenuation equations of the maximum ground motions by Kawashima et al. (1984, 1985a), the following empirical formula is assumed to represent the attenuation characteristics of RMS displacement σ_u [cm]:

$$\sigma_u = a(GC_i) \times 10^{b(GC_i)M} \times (\Delta+30)^{c(GC_i)} \tag{5.1}$$

where M and Δ [km] are earthquake magnitude and epicentral distance, respectively, and GC_i (i=1···3) represents the soil condition group. Coefficients $a(GC_i)$, $b(GC_i)$ and $c(GC_i)$ are constants to be determined for each soil condition.

The coefficients determined by a multiple regression analysis are shown in Table 5.2 (Tamura and Aizawa, 1992). The coefficient $b(GC_i)$, which represents the effect of earthquake magnitude on RMS displacement, varies from 0.46 to 0.60, and it becomes larger in the order soil condition group 1, 2 and 3. The coefficient $c(GC_i)$, representing the attenuation rate of RMS displacement with epicentral distance, is about −1.0 for groups 2 and 3. The coefficient $c(GC_i)$ for group 1 is a little smaller than those for groups 2 and 3.

Table 5.2 Coefficients of RMS displacement attenuation equation

Soil Condition	*a*	*b*	*c*	Correlation Coefficient	Standard Error
Group-1	7.394×10^{-2}	0.460	−1.314	0.814	0.247
Group-2	7.022×10^{-3}	0.545	−1.000	0.761	0.247
Group-3	5.935×10^{-3}	0.595	−1.027	0.652	0.256

Kawashima et al. (1984, 1985a) studied the attenuation characteristics of the maximum displacement based on the same 197 sets of two horizontal SMAC accelerograph records with those analyzed in this study. The same formula with Eq.(5.1) was adopted as an attenuation equation of the maximum displacement. According to their result, the coefficients of attenuation equation of the maximum displacement [cm] are listed in Table 5.3.

Comparing the coefficients *b* in Tables 5.2 and 5.3, they show almost equal values. This fact means that the earthquake magnitude affects similarly attenuations of the RMS and maximum values of displacement. The coefficients *c* in Tables 5.2 and 5.3 also take close values, which indicates that the attenuation rate with epicentral distance is almost equivalent for the RMS and maximum values of displacement.

Table 5.3 Coefficients of maximum displacement attenuation equation

Soil Condition	*a*	*b*	*c*
Group-1	0.886	0.393	−1.390
Group-2	0.056	0.549	−1.179
Group-3	0.070	0.575	−1.224

Fig.5.1 compares the RMS displacement calculated from the observed data and estimated from the attenuation equation for M=5, 6, 7 and 8. RMS displacement for an arbitrary combination of earthquake magnitude M and epicentral distance Δ can be read from Fig.5.1. For example, RMS displacement for M=7 and Δ=50 [km] is 0.39 cm for group 1, 0.57 cm for group 2 and 0.96 cm for group 3.

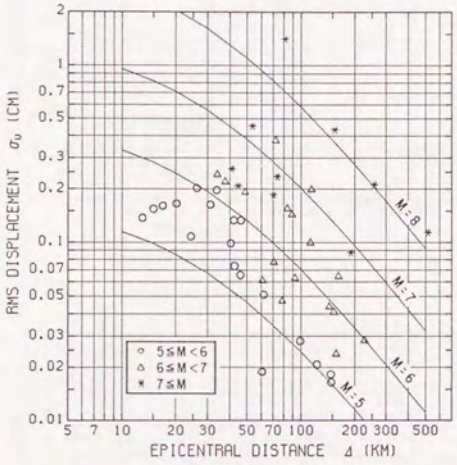

(a) Soil condition group 1

Fig.5.1(1) Attenuation of RMS displacement

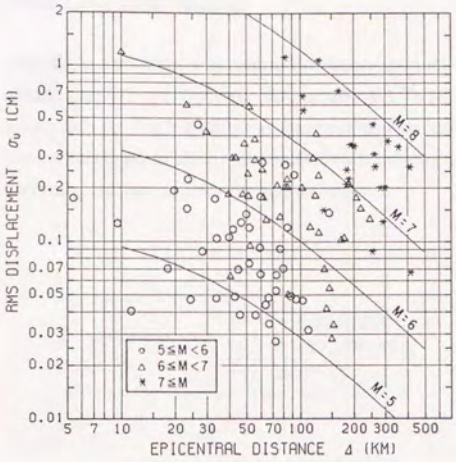

(b) Soil condition group 2

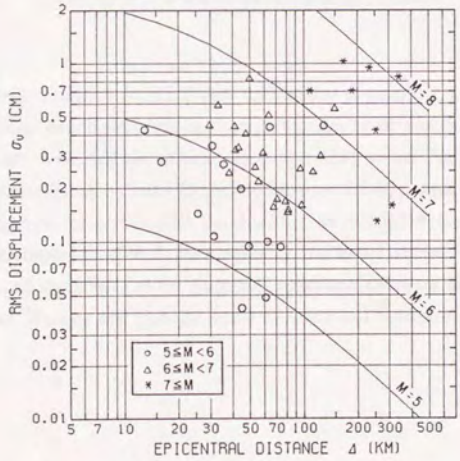

(c) Soil condition group 3

Fig.5.1(2) Attenuation of RMS displacement

5.3 Temporal and Spatial Correlation Functions

Eq.(4.1) is adopted as a temporal correlation function of ground motion and applied to the 197 sets of ground displacement records. The parameters T_0 and α are determined for each data by least squares fit. Fig.5.2 shows an example of least squares fits, where the solid and dashed lines correspond to temporal correlation functions calculated from the observed data and estimated by least squares fit, respectively.

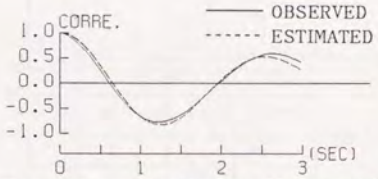

Fig.5.2 Temporal correlation function (Horoman Bridge, Aftershock of Tokachi-Oki earthquake, 1968)

Strong motion duration B_T for which stationarity is assumed, L_{DT} calculated from Eq.(4.4) and $2B_T/L_{DT}$ which signifies an average number of up and down zero crossings over the duration are evaluated simultaneously with a RMS value. Fig.5.3 shows $2B_T/L_{DT}$ for each soil condition. Since a clear relationship between $2B_T/L_{DT}$ and, M or Δ is hard to be found from Fig.5.3, let us consider the distribution of $\log(2B_T/L_{DT})$ as a Gaussian distribution without regard to M or Δ, for simplicity. Table 5.4 shows the mean value and standard deviation of $\log(2B_T/L_{DT})$ for each soil condition (Tamura and Aizawa, 1992). The mean values of $2B_T/L_{DT}$ are 12.4, 27.4 and 24.7 for soil condition groups 1, 2 and 3, respectively.

Table 5.4 Mean and standard deviation of $\log(2B_T/L_{DT})$

Soil Condition	Mean	Standard Deviation
Group-1	1.092	0.255
Group-2	1.437	0.285
Group-3	1.393	0.268

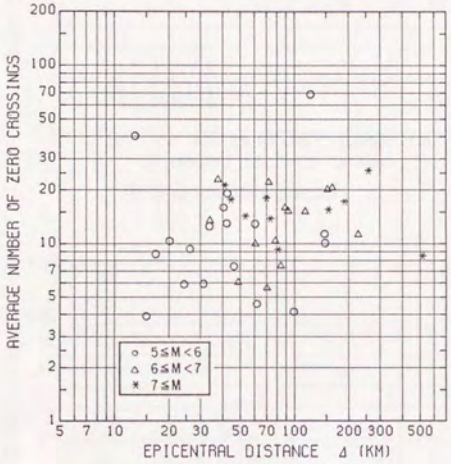

(a) Soil condition group 1

Fig.5.3(1) Relationship between $2B_T/L_{DT}$, earthquake magnitude and epicentral distance

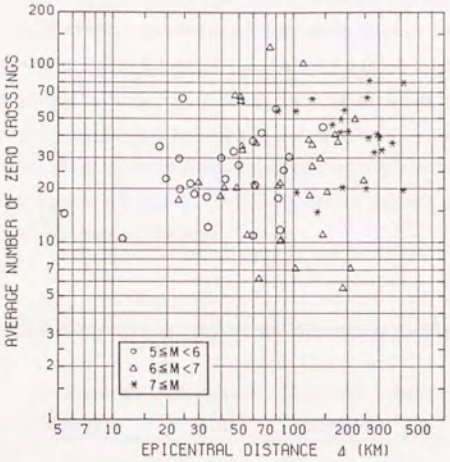

(b) Soil condition group 2

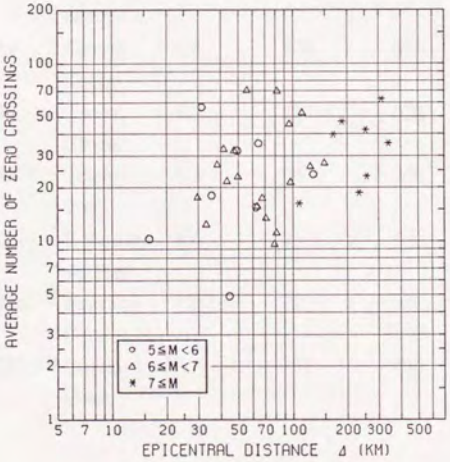

(c) Soil condition group 3

Fig.5.3(2) Relationship between $2B_T/L_{DT}$, earthquake magnitude and epicentral distance

Eq.(4.2) is employed as a spatial correlation function and applied to the ground motion data of the eight events recorded at the four array sites in Shizuoka Prefecture, Japan, which are shown in Tables 4.1 and 4.2. ξ_0 values for these events shown in Tables 4.3 and A.2 are again listed in Table 5.5. ξ_0 varies from 300 m to 910 m among these eight events. Fig.5.4 shows the relationship between ξ_0 and the maximum ground displacement u_{max}. u_{max} is the mean value of the maximum displacements of the stations in each site, which are shown in Tables 4.3 and A.2. In the scope of present study, ξ_0 seems to increase as ground motion becomes stronger.

Table 5.5 Array records analyzed and their spatial parameters

Site	Date	Epicentral Region	Magnitude	Epicentral Distance[km]	Radial ξ_0[m]	Transverse ξ_0[m]
Sagara	3/16/83	S Coast of Chubu	5.7	55	300	340
	11/24/83	S Coast of Chubu	5.0	45	470	480
Yaizu	9/14/84	Central Chubu	6.8	126	530	910
	9/15/84	Central Chubu	6.2	127	620	650
Numazu	3/18/88	Tokyo Pref	6.0	96	700	820
	9/5/88	E Yamana-shi Pref	5.6	45	550	580
Matsuzaki	11/22/86	Near Izu-Oshima Is.	6.0	72	380	550
	12/17/87	Kujukuri Coast	6.7	171	420	370

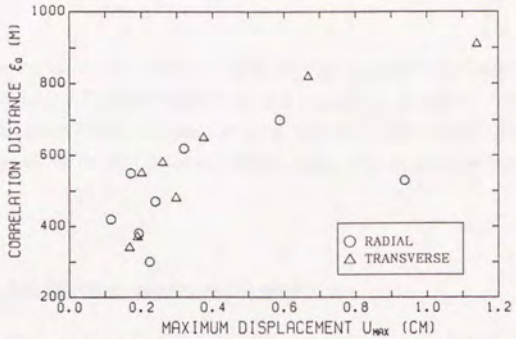

Fig.5.4 Relationship between ξ_0 and maximum displacement

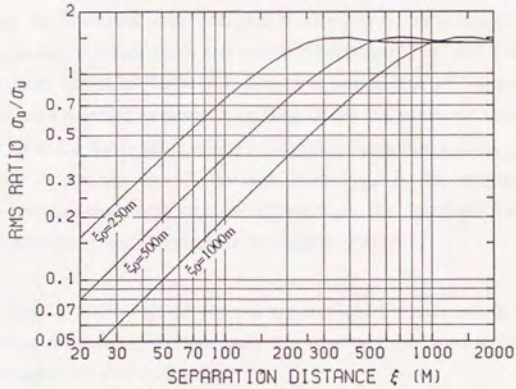

Fig.5.5 RMS displacement ratio σ_d/σ_u

ξ_0 may be related to earthquake magnitude, epicentral distance, soil condition, and so on, however it is not practical to discuss this relationship with only eight relatively small event records. Therefore, the effect of ξ_0 on the estimation of σ_d is studied by varying ξ_0

over a certain range. Fig.5.5 shows the rate of σ_d/σ_u for ξ_0=250, 500 and 1000 [m]. As seen from Eq.(4.3) and Fig.5.5, σ_d/σ_u varies nearly as $2\xi/\xi_0$ up to $\xi=\xi_0$, and then it takes almost a constant value ($=\sqrt{2}$). Note that the shorter ξ_0 will give the larger σ_d for a given σ_u.

Combining either Eqs.(4.3) and (5.1), or Figs.5.1 and 5.5, σ_d can be estimated for a combination of earthquake magnitude and epicentral distance. Although Eq.(4.3) represents a deviation of the Gaussian process once σ_u is determined, it should be noted that the estimation of σ_u also involves scatter around the regression value as shown in Fig.5.1.

5.4 Maximum Relative Displacement and Ground Strain

The maximum relative displacement $d_{\max}$ can be estimated by combining Eqs.(3.30), (4.3), (5.1), and either B_T and L_{DT} defined by Eq.(4.4) or $2B_T/L_{DT}$. As stated in Section 5.1, the discussion is here limited to the temporal maxima, however the spatial maxima can be estimated similarly. Fig.5.6 compares the maximum relative displacement calculated from the observed array data and inferred from the presenting procedure for corresponding earthquake magnitude and epicentral distance. The results are shown for the four event records listed in Table 4.1. The soil conditions of Sagara, Numazu and Matsuzaki sites are classified as group 2, and that of the Yaizu site is classified as group 3. $2B_T/L_{DT}$ is set up as the mean value which is shown in Table 5.4, and the probability of not being exceeded p is taken as 0.5. As seen from Fig.5.6, the inferred $d_{\max}$ may be considered to be consistent with that calculated from the observed records for Yaizu, Numazu and Matsuzaki sites, allowing for the following facts:

1) The SMAC accelerograph records are employed to estimate σ_u and $\rho_T(\tau)$ in the presenting procedure, consequently the maximum relative displacement is not directly approximated in Fig.5.6.

2) Although σ_u and $2B_T/L_{DT}$ calculated from the observed records exhibit scatter as shown in Figs.5.1 and 5.3, only the mean values of them are considered to estimate the maximum relative displacement, for simplicity.

3) A resultant of two horizontal ground motion components is considered in the proposed method to yield the maximum σ_u on the horizontal plane, however the radial and transverse components are analyzed independently for the array data.

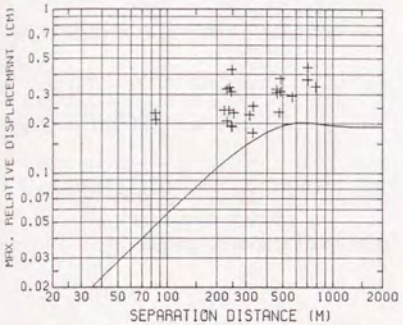

(a) Sagara, radial component

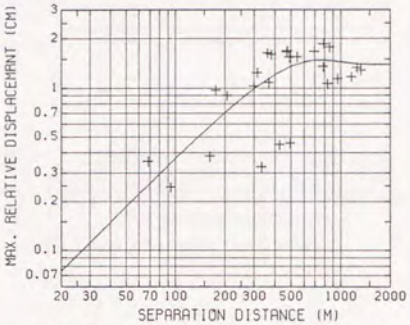

(b) Yaizu, radial component

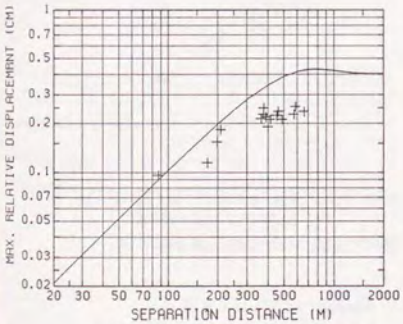

(c) Numazu, radial component

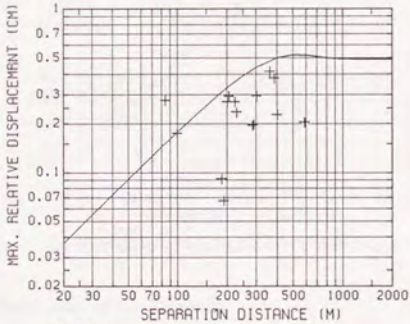

(d) Matsuzaki, radial component

Fig.5.6(1) Comparison of maximum relative displacement

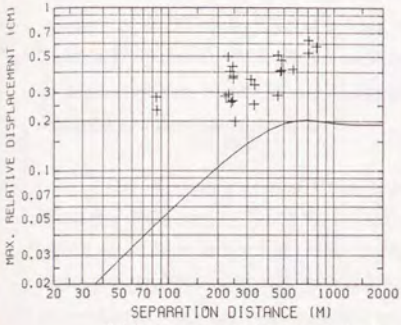

(e) Sagara, transverse component

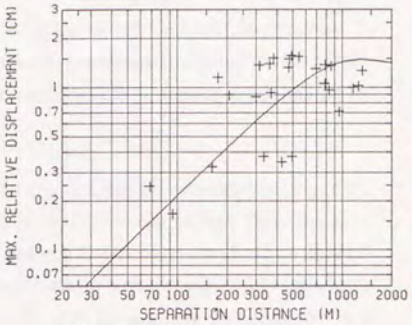

(f) Yaizu, transverse component

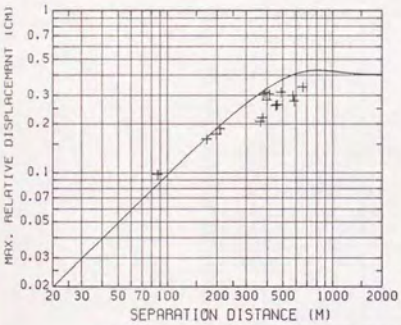

(g) Numazu, transverse component

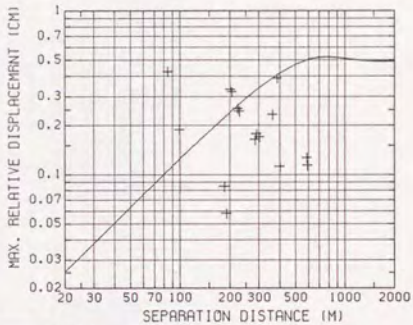

(h) Matsuzaki, transverse component

Fig.5.6(2) Comparison of maximum relative displacement

As for the Sagara site, the observed d_{max} is larger than that inferred from the proposed method. This may be due to the fact that the peak factor of the observed records at the Sagara site is exceptionally high, as shown in Fig.4.16.

Fig.5.7 shows the maximum relative displacement estimated for earthquake magnitude M=6, 7, 8 and epicentral distance Δ=50 [km], where the probability of not being exceeded p=0.5 and $2B_T/L_{DT}$ is put as the mean value for each soil condition. ξ_0 is assumed to be 500 m for all soil groups, considering the average value of ξ_0 presented in Table 5.5. As mentioned in the previous section, further studies are required to make clear ξ_0 dependence on event and site characteristics, therefore the presenting result should be regarded as a provisional estimation.

The maximum ground strain between two points can be estimated by Eq.(4.9). From the definition by Eq.(4.9), the maximum ground strain can be read from the axes which go up from left to right with 45 degrees in Fig.5.7. When the combination of M=7 and Δ=50 [km] is considered, the maximum ground strains between any two locations are about 40×10^{-6} for the soil condition group 1, 60×10^{-6} for group 2 and 100×10^{-6} for group 3.

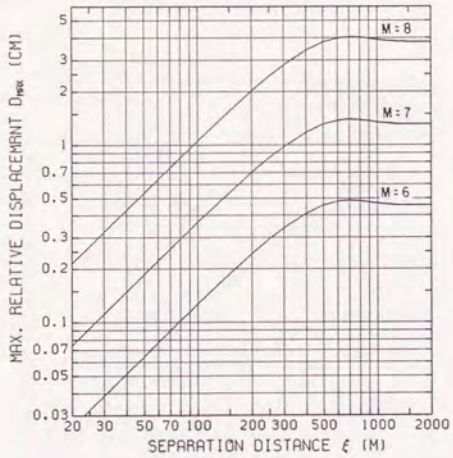

(a) Soil condition group 1

Fig.5.7(1) Estimated maximum relative displacement for M=6, 7, 8 and Δ=50 km

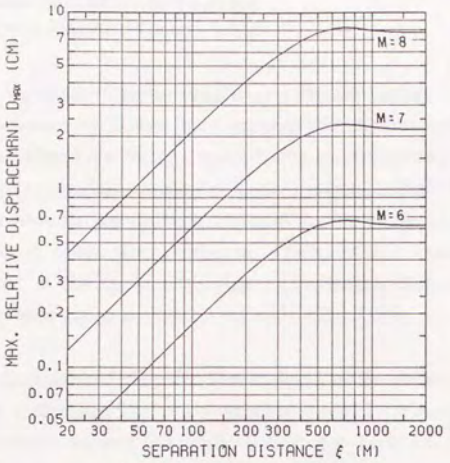

(b) Soil condition group 2

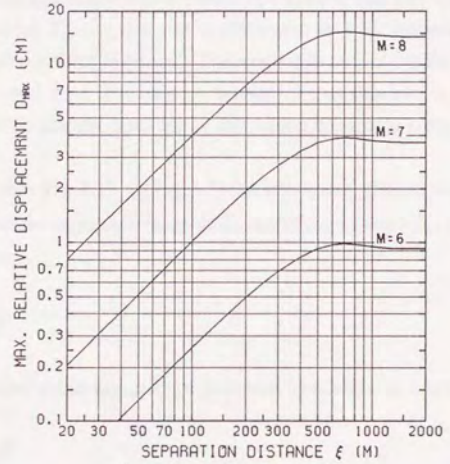

(c) Soil condition group 3

Fig.5.7(2) Estimated maximum relative displacement for M=6, 7, 8 and Δ=50 km

5.5 Attenuation Characteristics of Ground Strains

5.5.1 Comparison with Measured Ground Strains

Based on the results of the previous section, the attenuation characteristics of the maximum ground strains are studied and compared with the observed ground and pipe strain data. It is considered that the pipe strain during an earthquake is almost equivalent with the ground strain (e.g., Japan Society of Civil Engineers, 1989b). The strain data here employed were observed at the Chiba Experiment Station by the Institute of Industrial Science, University of Tokyo (Katayama et al., 1990a, 1990b), Kansen and Shimonaga observation stations in Hachinohe City, Aomori Prefecture (Kogarumai et al., 1978, 1979), and Ohmori observation station (Nishio et al., 1978, 1979).

The Chiba Experiment Station data here analyzed are the maximum axial strains of a steel pipe, 150 mm in diameter. The natural period of ground T_G at this station is calculated as 0.38 seconds from the reported soil profile. Referring to Table 5.1, the soil condition is classified as group 2. The Kansen station data are directly measured ground strains. T_G for this station is 0.44 seconds (Iwamoto et al., 1982a), and the soil condition is classified as group 2. The Shimonaga station data are axial pipe strains. This pipe is a ductile iron pipe, 1000 mm in diameter. T_G for this site is estimated as 1.31 seconds (Iwamoto et al., 1982b), and the soil condition is group 3. The strain data obtained at the Ohmori station are axial strains of a steel pipe, 200 mm in diameter. T_G of this site is calculated as 0.38 seconds, consequently the soil condition of this station belongs to group 2.

As seen from Fig.4.17 or Fig.5.7, the maximum ground strains between two locations arises over the separation range $\xi \leq \xi_0$. Referring to Fig.5.5, σ_d for this range can be approximated as

$$\sigma_d = 2\xi\sigma_u/\xi_0 \tag{5.2}$$

The maximum ground strain ε_{max} may be estimated by combining Eqs.(3.30) and (5.2) as

$$\varepsilon_{max} = d_{max}/\xi$$

$$= 2\sqrt{2\ln\left\{-\frac{2B_T}{L_{DT}\ln p}\right\}}\,\frac{\sigma_u}{\xi_0} \tag{5.3}$$

where σ_u is described by Eq.(5.1).

Fig.5.8 compares the estimated maximum ground strains and observed ones. For the estimation of the ground strain, the probability of non-exceeding is taken as 0.5, $2B_T/L_{DT}$ is chosen as the mean value for each soil condition, and ξ_0 is provisionally assumed to be 500 m for all soil groups. The observed maximum ground strains at Chiba, Kansen and Ohmori are plotted in the figure for soil condition group 2, and those observed at Shimonaga are shown in the figure for group 3. The maximum values at Kansen and Shimonaga are taken from the study by Nakamura et al. (1982). In Fig.5.8 (c), which is for the soil condition group 3, the attenuation equation of the maximum ground strains based on finite element analysis of array records are also presented, which will be referred in Section 5.5.2.

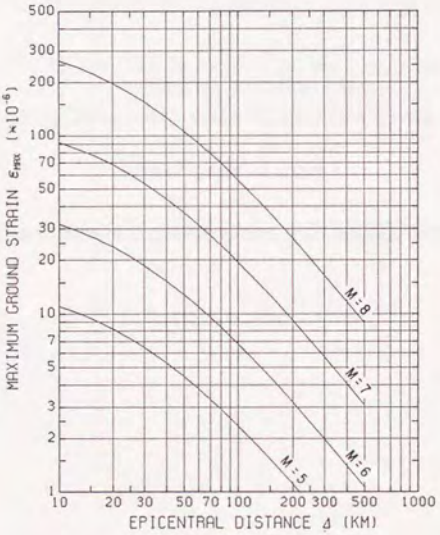

(a) Soil condition group 1

Fig.5.8(1) Comparison of maximum ground strain attenuation characteristics

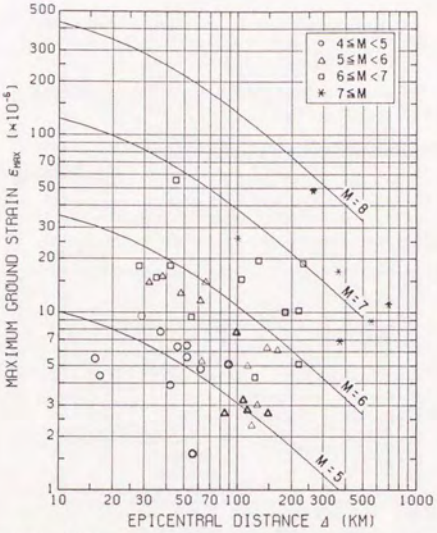

Note; Normal symbols: Chiba, Bold symbols: Kansen, Fine symbols: Ohmori

(b) Soil condition group 2

Fig.5.8(2) Comparison of maximum ground strain attenuation characteristics

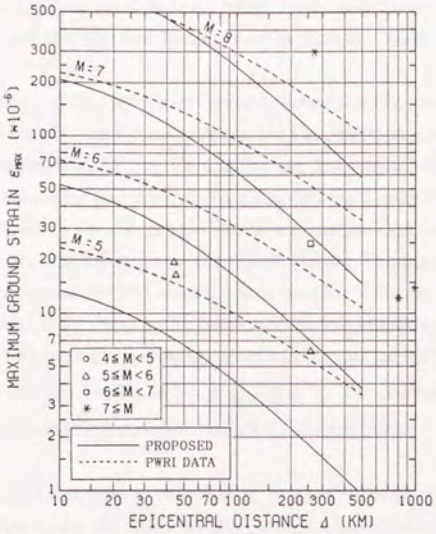

Note; Symbols: Shimonaga

(c) Soil condition group 3

Fig.5.8(3) Comparison of maximum ground strain attenuation characteristics

As seen from Fig.5.8, the attenuation characteristics of the estimated maximum ground strains coincide fairly well with those of the observed data. This fact may support the efficiency of the presenting method and assumed parameters, though it should be noted that there remains the necessity of further studies to establish event and site dependence of parameters.

5.5.2 Comparison with Finite Element Analysis Result

The attenuation characteristics of maximum ground strains are also studied with the ground strains estimated from the array observation records, which were obtained at the

Public Works Research Institute (PWRI), Tsukuba. These strains are estimated by a three dimensional finite element analysis, and empirical attenuation equations are presented by multiple regression analyses (Tokida et al., 1990, 1991). Results are shown in Appendix C. T_G for the array site at PWRI is 0.78 seconds (Sasaki et al., 1989).

The attenuation of the upper level (ground surface level) normal strains at A-Field, PWRI is employed for the comparison with that for soil condition group 3 here estimated. The result is shown in Fig.5.8 (c). Comparing the attenuation characteristics of the maximum ground strains for soil group 3 and those estimated from PWRI data, the effect of earthquake magnitude on the ground strain attenuation and attenuation rate with epicentral distance are slightly large for the former results. The maximum ground strain estimated by the proposed method shows a little smaller value as compared with that estimated from PWRI array data, for a given combination of earthquake magnitude and epicentral distance. For example, the maximum ground strains for M=7 and Δ=50 [km] are estimated as 103×10^{-6} for soil condition group 3 by the proposed procedure, and 136×10^{-6} by the attenuation equation baed on PWRI array records.

There may exist a number of contributory factors to this difference of ground strain estimation, for example, the difference of sites, ground motion data analyzed, and so on. Let us here focus on the effect of separation distance between observation stations on the ground strain estimation. The separation distances between stations are mostly greater than 100 m for the four arraies in Shizuoka Prefecture, Japan. On the other hand, it is 50 m at the PWRI campus. The proposed ground strain estimation method is basically based on the stationary Gaussian random field model of ground motion in time and space, which primarily assumes the homogeneous ground. The efficiency of this method was confirmed to yield a good approximation for estimating the average maximum ground strain mainly over a separation distance longer than 100 m, by calibrating from the array data recorded at the four sites in Shizuoka Prefecture. However, as for the shorter separation distance, the ground strain due to local heterogeneity may have dominant effects and the larger ground strain arises as compared to the ground strain based on the stationary stochastic process theory.

Considering the comparison results with both measured ground strains and those estimated by the finite element procedure, the presenting ground strain estimation may be regarded to give fairly good approximation to the observed data.

5.6 Conclusions

A practical method to estimate the maximum relative displacement between two points is proposed. It basically depends on the time-space separable correlation model established in Chapter 3, and consists of the estimation of RMS displacement, temporal and spatial correlation functions of displacement. RMS displacement and the temporal correlation function are estimated from the conventional independent strong motion observation data, and the spatial correlation function is calibrated from the array observation records. Based on the results of maximum relative displacement estimation, the attenuation characteristics of maximum ground strains are studied and compared with the observed data and those estimated by the finite element analysis of array data. The following conclusions may be deduced from the presented results.

1) Attenuation equations of RMS displacement in terms of earthquake magnitude and epicentral distance are proposed for the three soil conditions.

2) Both the proposed temporal and spatial correlation function models agree well with the correlation functions calculated from the observed data. The correlation distance parameter ξ_0, representing a separation distance at which the spatial correlation of ground motions becomes 0, seems not to exceed 1 km, although its dependence on event and site conditions should be further studied.

3) An average number of zero crossings during strong motion duration estimated from the temporal correlation function may not be very sensitive to earthquake magnitude or epicentral distance.

4) The proposed method may give useful results for the estimation of ground strain attenuation, even though it considers only the mean levels of RMS displacement, zero crossing number and correlation distance. The efficiency of estimation is confirmed by comparing to the attenuation characteristics of measured ground strains and those evaluated by finite element analysis.

6. CONCLUDING REMARKS

6.1 Conclusions

The primary objective of the present study is to establish practical methods for estimating earthquake-induced ground strains. The major conclusions of this study may be summarized as follows.

In Chapter 1, the background of the present study is summarized, and the scope and organization of this dissertation are described.

Since ground strain is defined as the derivative of displacement with respect to space, it may be usual to estimate ground strain from ground displacement. Considering the fact that ground acceleration is generally monitored in strong motion observations for engineering purposes, the accuracy of displacement calculated from acceleration is empirically studied in Chapter 2. Two kinds of shaking table tests are carried out with a 16 bits digital strong motion accelerograph, which is used for the array observation by the Public Works Research Institute, Ministry of Construction, Japan. According to the experiment results, it has been proven that the practically reliable frequency range of filtering may be taken as low as 1/10 Hz. The maximum relative displacement estimated from the two independent digital accelerographs may include an error corresponding to 5 to 10 % of the maximum displacement.

In Chapter 3, two simple ground motion spectral models are introduced, assuming ground motion stationarity in time and space. These models are derived from a standard time-space varying ground motion cross-spectrum model, which is expressed as

$$S(f,\eta)=S_0(f)\gamma(f,\eta)\exp\left(-i\frac{2\pi f\eta}{c}\right) \tag{6.1}$$

where $S_0(f)$ is the power spectral density function of displacement at any point, $\gamma(f,\eta)$ is the coherence function, and c is the apparent propagation velocity of seismic waves.

The first model, the "frequency independent coherence model", employing a coherence value calculated at the ground motion predominant frequency as a representative, assumes that $\gamma(f,\eta)$ is independent of frequency. Consequently Eq.(6.1) can be reduced to

$$S(f,\eta)=S_0(f)\gamma(\eta)\exp\left(-i\frac{2\pi f\eta}{c}\right) \tag{6.2}$$

The second model, the "time-space separable correlation function model" assumes the infinite propagation velocity of seismic waves, so that the time-space covariance function of ground motion is a separable function of time and space. The time-space cross spectral density function for this model is expressed as

$$S(f,\eta)=S_0(f)\rho_S(\eta) \tag{6.3}$$

The time-space covariance function of relative displacement is derived from these two proposed ground motion models. The maximum relative displacement is estimated by assuming a Poisson arrival of extremes. Both temporal maxima over any fixed distance and spatial maxima at any fixed time can be estimated by the proposed method.

The proposed two ground motion models are calibrated from the array observation records in Chapter 4. The array records employed were obtained in Shizuoka Prefecture, Japan. Both the frequency independent coherence model and the time-space separable correlation model have been found to yield considerably accurate relative displacement statistics, both root mean square and maximum values. Their results generally lie within the scatter shown between the observed data. Little difference exists between the results estimated from the frequency independent coherence model and the time-space separable correlation model, once the spatial coherence function and the apparent propagation velocity of seismic wave in the former model, and the spatial correlation function in the latter model are suitably calibrated.

The time-space separable correlation model is comprised of the root mean square displacement σ_u, the temporal correlation function $\rho_T(\tau)$, and the spatial correlation function $\rho_S(\eta)$ of displacement. Since σ_u and $\rho_T(\tau)$ may be estimated by pooling displacement records temporally, the conventional independent strong motion records are employed to estimate them in Chapter 5. An attenuation equation of σ_u is presented in terms of earthquake magnitude M and epicentral distance Δ. From $\rho_T(\tau)$ calibrated with the same

data set as σ_{t_0}, an average number of zero crossings over the strong motion duration, which is directly necessary to estimate the maximum relative displacement, is derived. $\rho_S(\eta)$ is calibrated from the array observation records. In addition to the array records analyzed in Chapter 4, another four sets of array records are employed for this estimation. Finally, the temporal maximum relative displacement is estimated in terms of M and Δ.

The maximum ground strains are evaluated from the maximum relative displacement, and are compared with the observed ground and pipe strains during earthquakes. The ground strains estimated from array observation records by finite element analysis are also employed for this comparison. As a result of the comparison, the ground strain estimation based on the proposed ground motion spectral models has been found to give fairly good approximation to the observed data.

Note that the present estimation method of the maximum relative displacement or ground strain considers only the mean levels of temporal and spatial parameters, for simplicity, and that the observed maximum relative displacement and ground strains show certain dispersion around the estimated values. This dispersion should be carefully considered when the present result is applied to design practice.

6.2 Recommendations for Future Research

Processing of Accelerograms

As shown in Chapter 2, ground displacement is calculated from recorded acceleration by numerical integration in the frequency domain. This calculation procedure is widely used, however it still remains as one of the methods of integrating acceleration (IASPEI/IAEE, 1988). A number of studies (e.g., Saito, 1978; Iwan et al., 1985; Yamada et al., 1989; Hayashi et al., 1991) have been conducted in this field. It may be useful to estimate ground displacement by another technique and compare the results with that presented in this study.

Model Extensions and Parameter Estimation Study

Limitations of this study include its focus on relatively small magnitude events at only four sites, and its calibration with site-specific array data. It would be useful to apply this model more widely, to validate and calibrate it with more data and facilitate its use in engineering analysis and design. In particular, systematic study might be made of the

spatial parameters of correlation and coherence functions, to assess their dependence on event characteristics, such as earthquake magnitude, epicentral distance and site condition such as soil conditions.

Statistical and Model Uncertainty

While the median predictions of peak relative displacement generally show the correct trend(e.g., Fig.4.18), note that 0.16- and 0.84-level fractiles appear too narrow. This is because they include only "random vibration" uncertainty in the Gaussian model, not gross uncertainty in the model and its parameters. For example, the model parameters may not be reliably estimated from only the limited ground motion time histories, the model itself may be of incorrect parametric form, and so on.

Methods exist to quantify this effect more precisely. By including these broader sources of statistical uncertainty, such methods could provide more realistic uncertainty bands and isolate the sources of major contributors.

Heterogeneity and Nonstationarity

Scatter in relative displacement results may also be caused by local spatial heterogeneity in site conditions. We have here adopted a simple homogeneous-stationary random field model, simply because it is the easiest to calibrate. Robust discrimination and estimation of spatial heterogeneity requires a good deal more data. This may become increasingly possible as available array data increase.

Another aspect of heterogeneity is temporal heterogeneity, i.e., nonstationary ground motion behavior over the event duration. If we retain the simplest time-space separable correlation model and spatial homogeneity, the first modification would be merely to replace $S_0(f)$ in Eq.(6.3) with a corresponding time-varying evolutionary spectrum.

APPENDIX A.
ANALYSIS OF ARRAY DATA BY THE TIME-SPACE SEPARABLE CORRELATION MODEL

A.1 General Remarks

As shown in Chapter 4, the frequency independent coherence model and the time-space separable correlation model were calibrated from the four event array records shown in Table 4.1. In addition to these records, another four sets of array data are employed to calibrate the time-space separable correlation model. These data were obtained from four earthquakes shown in Table A.1.

Table A.1 Earthquakes analyzed for time-space separable correlation model

Site	Date	Epicentral Region	Magnitude	Epicentral Distance[km]	Azimuth [degree]*
Sagara	3/16/83	S Coast of Chubu	5.7	55	283
Yaizu	9/15/84	Central Chubu	6.2	127	323
Numazu	3/18/88	Tokyo Prefecture	6.0	96	51
Matsuzaki	12/17/87	Kujukuri Coast, Boso	6.7	171	66

Note: * Clockwise from north

A.2 Temporal and Spatial Correlation Functions

Eqs.(4.1) and (4.2) are employed as temporal and spatial correlation functions of ground displacement, respectively. Parameters T_0, α and ξ_0 determined by least squares fits are shown in Table A.2. The maximum ground displacement u_{max} and the root mean square value of displacement σ_u averaged for each site are also shown in the same table. B_T

and B_S in Table A.2 represent the temporal and spatial intervals in which the stationarity of ground motion is assumed, respectively. Fitted spatial correlation functions and those calculated from the observed data are shown in Fig.A.1.

Table A.2 Parameters of ground motion model

(a) Radial component

Site	B_T [sec]	N*	$u_{\max}$ [cm]	σ_u [cm]	T_0 [sec]	α	ξ_0 [m]	B_S [m]
Sagara	3.0-9.0	8	0.223	0.0746	0.70	0.15	300	1000
Yaizu	5.0-12.0	8	0.320	0.1406	1.50	0.15	620	2000
Numazu	6.5-12.5	7	0.588	0.1872	0.90	0.40	700	1500
Matsu-zaki	2.0-10.0	6	0.116	0.0495	1.00	0.25	420	1000

(b) Transverse component

Site	B_T [sec]	N*	$u_{\max}$ [cm]	σ_u [cm]	T_0 [sec]	α	ξ_0 [m]	B_S [m]
Sagara	3.0-9.0	8	0.168	0.0666	0.70	0.15	340	1000
Yaizu	5.0-12.0	8	0.375	0.1425	1.85	0.25	650	2000
Numazu	6.5-12.5	7	0.668	0.1975	0.90	0.40	820	1500
Matsu-zaki	2.0-10.0	6	0.190	0.0771	1.05	0.15	370	1000

Note: * Number of stations

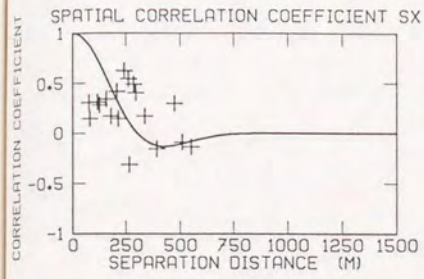

(a) Sagara, radial component

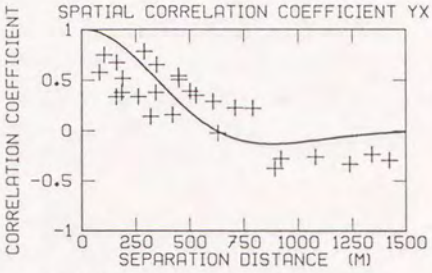

(b) Yaizu, radial component

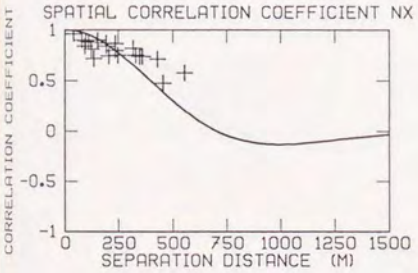

(c) Numazu, radial component

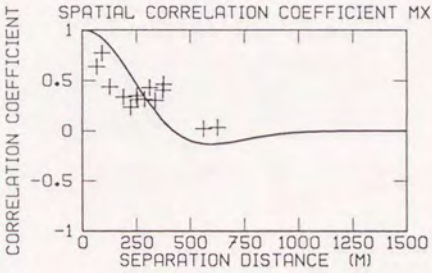

(d) Matsuzaki, radial component

Fig.A.1(1) Spatial correlation function

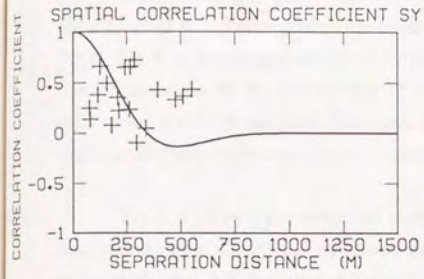

(e) Sagara, transverse component

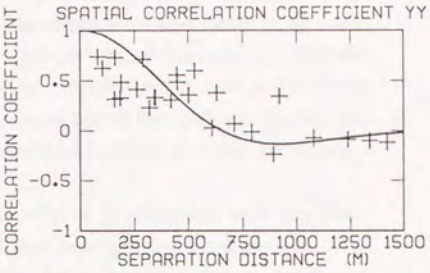

(f) Yaizu, transverse component

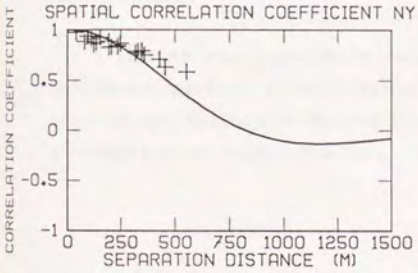

(g) Numazu, transverse component

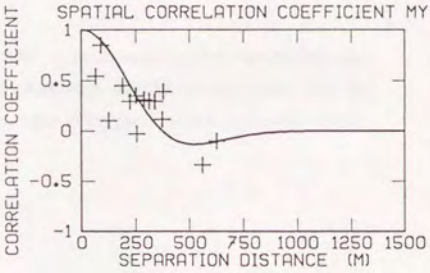

(h) Matsuzaki, transverse component

Fig.A.1(2) Spatial correlation function

A.3 Maximum Relative Displacement Estimated from Time-Space Correlation Model

The root mean square value of relative displacement estimated from Eq.(4.3) is shown in Fig.A.2. Those calculated from the observed data are also shown in the same figure. Fig.A.3 shows peak factors of temporal maximum relative displacement. The solid line corresponds to the probability of not being exceeded p=0.5, and dashed lines correspond to p=0.84 and 0.16. The range between two dashed lines indicates roughly one standard deviation dispersion from the mean value consistent with a Gaussian distribution.

Fig.A.4 shows the temporal maximum relative displacement over any fixed distance. Similar to Fig.A.3, solid and dashed lines represent p=0.5 and p=0.84, 0.16, respectively. Fig.A.5 shows the spatial maximum relative displacement at any fixed time, where results for p=0.5 and p=0.84 are shown.

A.4 Conclusions

The time-space separable correlation model is calibrated for the four earthquake array records to estimate the maximum relative displacement. Results are compared with the observed data. Although the observed data show certain dispersion, the estimated results give fairly good approximation to them.

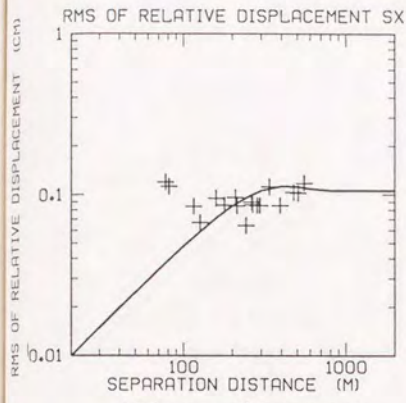

(a) Sagara, radial component

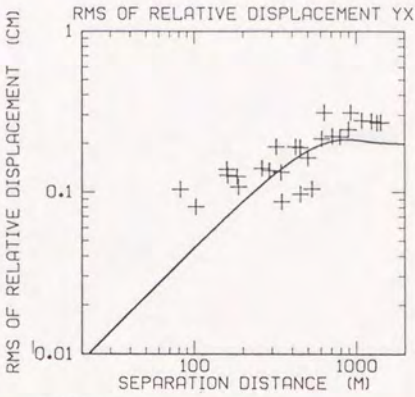

(b) Yaizu, radial component

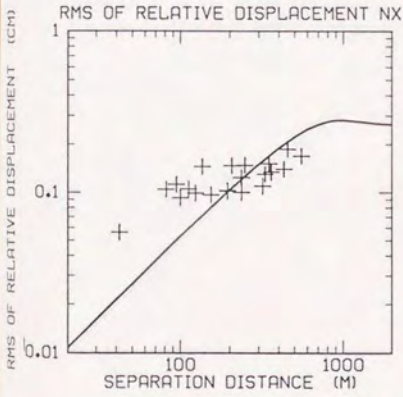

(c) Numazu, radial component

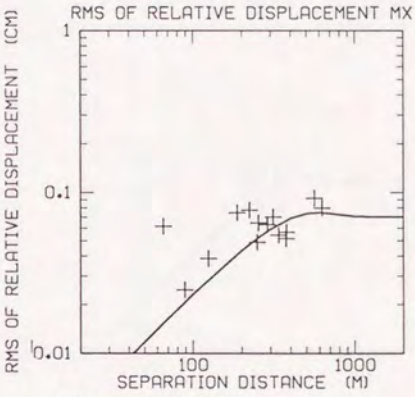

(d) Matsuzaki, radial component

Fig.A.2(1) RMS of relative displacement

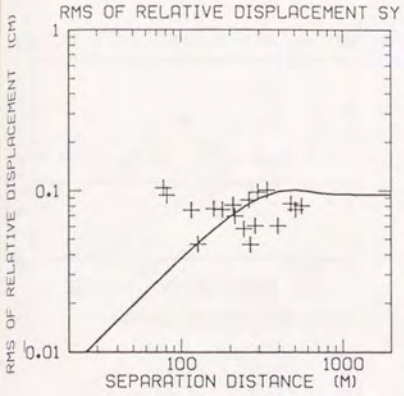

(e) Sagara, transverse component

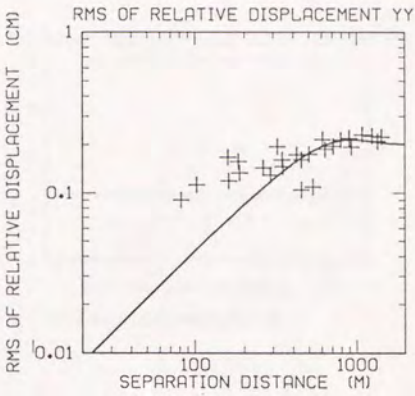

(f) Yaizu, transverse component

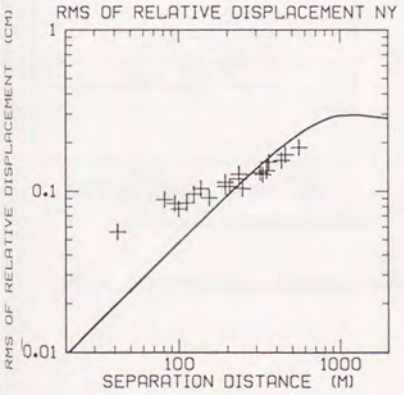

(g) Numazu, transverse component

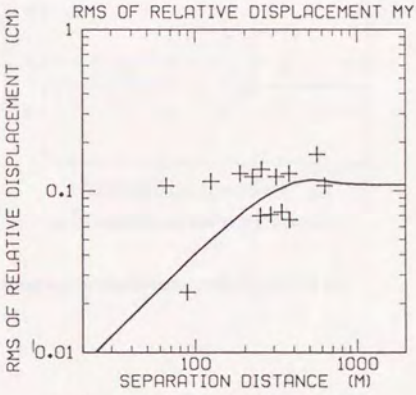

(h) Matsuzaki, transverse component

Fig.A.2(2) RMS of relative displacement

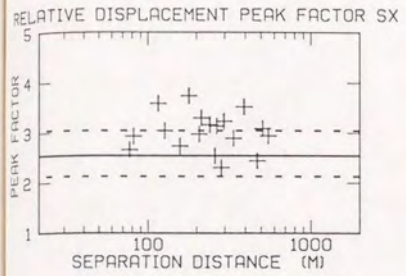

(a) Sagara, radial component

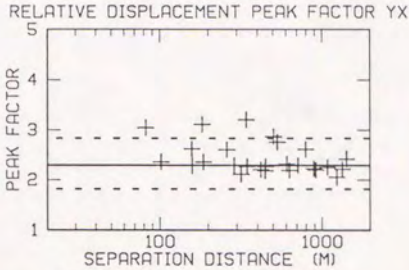

(b) Yaizu, radial component

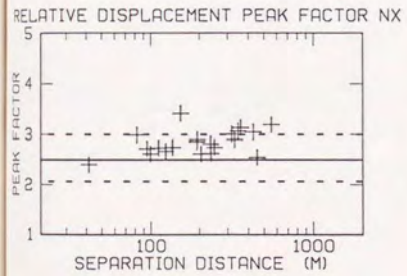

(c) Numazu, radial component

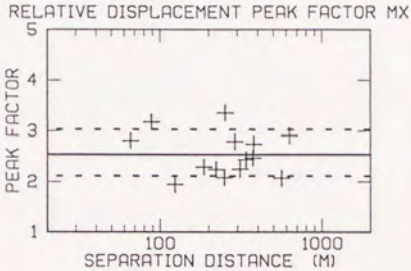

(d) Matsuzaki, radial component

Fig.A.3(1) Peak factor of temporal maximum relative displacement (p=0.84, 0.5, 0.16)

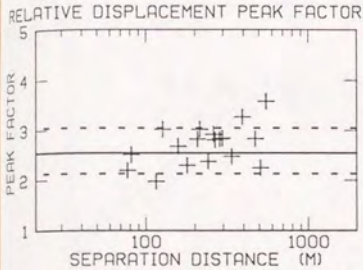

(e) Sagara, transverse component

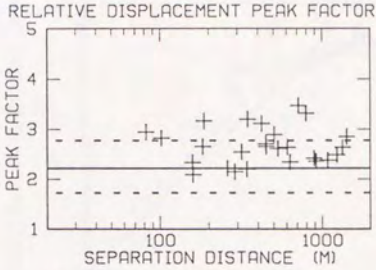

(f) Yaizu, transverse component

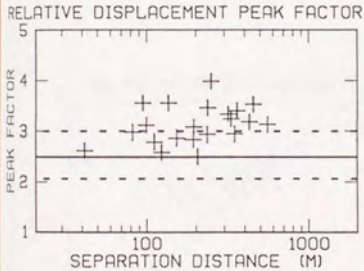

(g) Numazu, transverse component

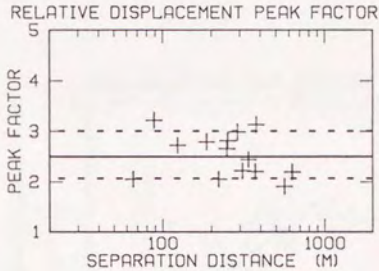

(h) Matsuzaki, transverse component

Fig.A.3(2) Peak factor of temporal maximum relative displacement (p=0.84, 0.5, 0.16)

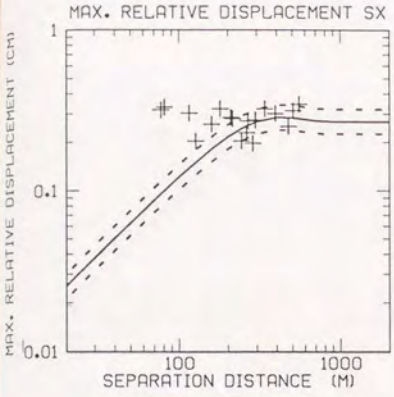

(a) Sagara, radial component

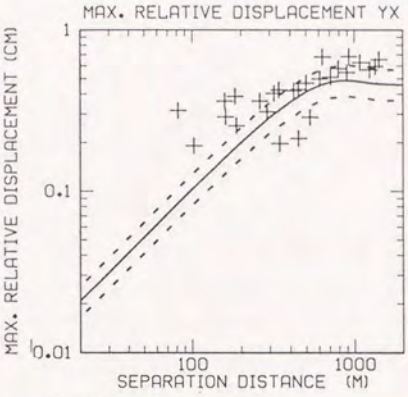

(b) Yaizu, radial component

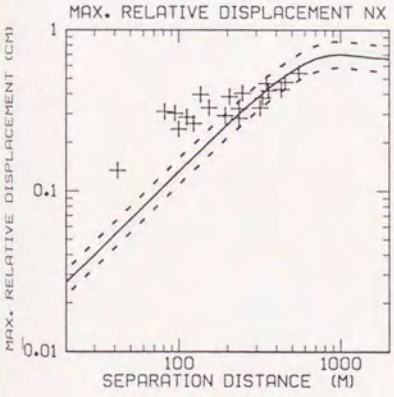

(c) Numazu, radial component

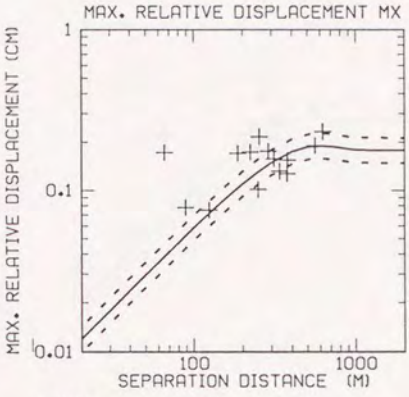

(d) Matsuzaki, radial component

Fig.A.4(1) Temporal maximum relative displacement (p=0.84, 0.5, 0.16)

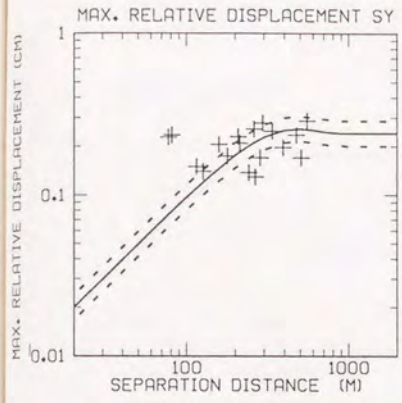

(e) Sagara, transverse component

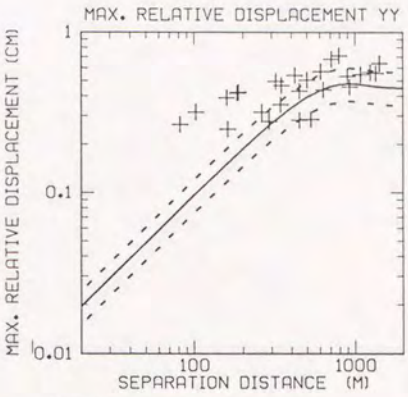

(f) Yaizu, transverse component

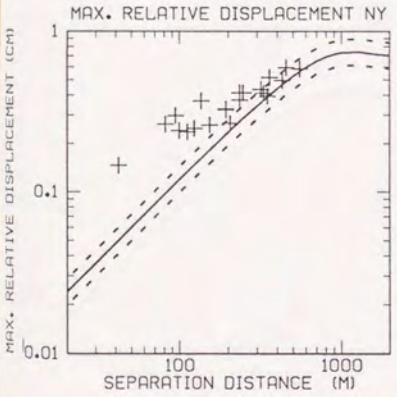

(g) Numazu, transverse component

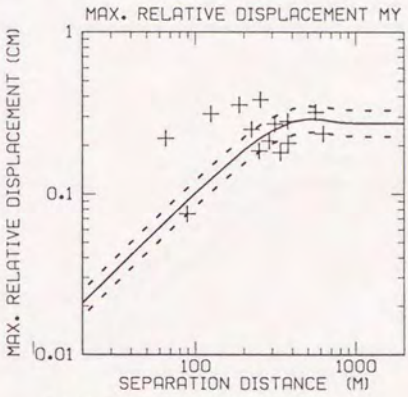

(h) Matsuzaki, transverse component

Fig.A.4(2) Temporal maximum relative displacement (p=0.84, 0.5, 0.16)

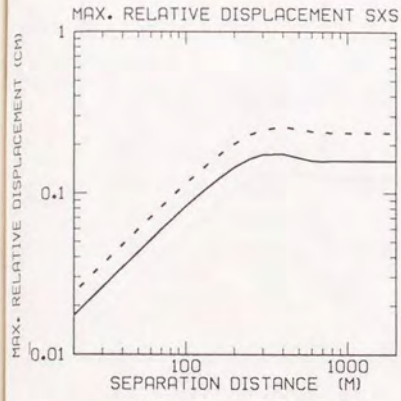

(a) Sagara, radial component

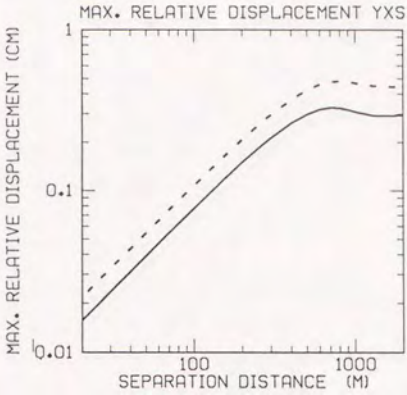

(b) Yaizu, radial component

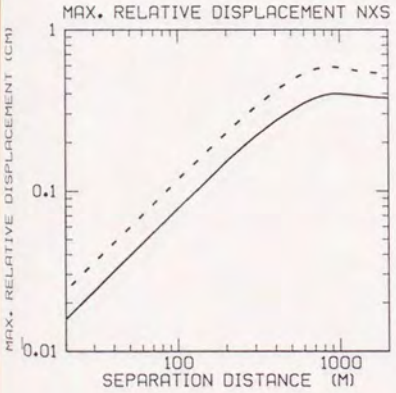

(c) Numazu, radial component

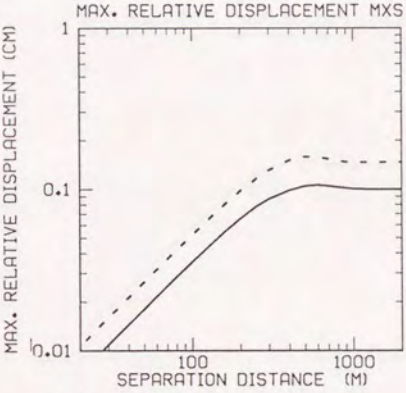

(d) Matsuzaki, radial component

Fig.A.5(1) Spatial maximum relative displacement (p=0.84, 0.5)

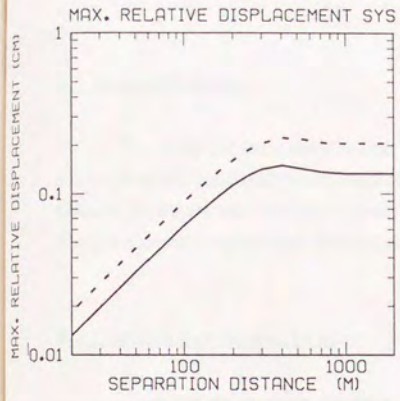

(e) Sagara, transverse component

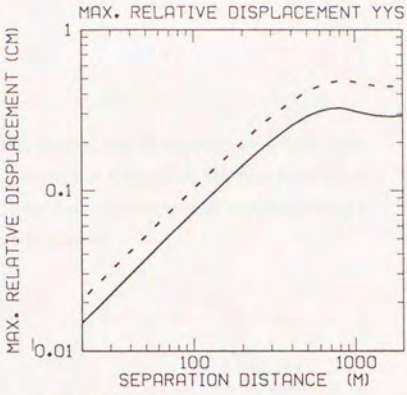

(f) Yaizu, transverse component

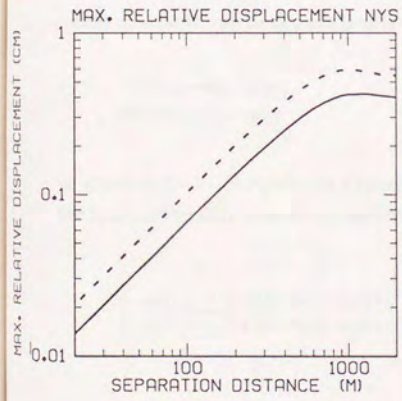

(g) Numazu, transverse component

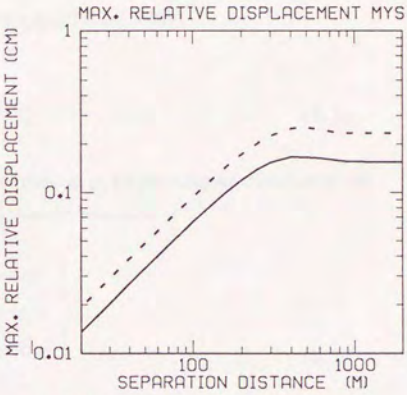

(h) Matsuzaki, transverse component

Fig.A.5(2) Spatial maximum relative displacement (p=0.84, 0.5)

APPENDIX B.
FINITE ELEMENT ANALYSIS OF GROUND STRAINS

B.1 General Remarks

To verify the estimation results of ground strains, two event records which were analyzed by the proposed ground motion spectral models in Chapter 4, are here employed. Ground strains are estimated by a standard two dimensional finite element analysis, using a triangle element consisting of three array observation stations.

B.2 Calculation of Ground Strains

Consider the triangle element shown in Fig.B.1, which consists of three array observation stations i, j and m to calculate ground strains. Assuming that ground displacement at a point in an element is expressed by a linear function of its spatial coordinate, ground displacement $u(t)$ and $v(t)$ at a point (x, y) in x (east-west) and y (north-south) directions may be described as (Zienkiewicz and Taylor, 1989)

$$u(t)=\alpha_1+\alpha_2 x+\alpha_3 y$$
$$v(t)=\alpha_4+\alpha_5 x+\alpha_6 y \qquad \text{(B.1)}$$

in which α_i $(i=1\cdots6)$ represents a constant. Determining α_i by prescribing coordinates of the three observation stations i, j and m, Eq.(B.1) can be written as

$$\begin{Bmatrix} u(t) \\ v(t) \end{Bmatrix} = \frac{1}{2\Delta}\begin{bmatrix} u_i(t) & u_j(t) & u_m(t) \\ v_i(t) & v_j(t) & v_m(t) \end{bmatrix}\begin{Bmatrix} a_i+b_i x+c_i y \\ a_j+b_j x+c_j y \\ a_m+b_m x+c_m y \end{Bmatrix} \qquad \text{(B.2)}$$

where

x_k, y_k $(k=i, j, m)$: coordinates of k-th array station

$u_k(t)$, $v_k(t)$ $(k=i, j, m)$: ground displacement at k-th array station

$$2\Delta=\begin{vmatrix} 1 & x_i & y_i \\ 1 & x_j & y_j \\ 1 & x_m & y_m \end{vmatrix} \tag{B.3}$$

$$a_i=\begin{vmatrix} x_j & y_j \\ x_m & y_m \end{vmatrix} \qquad b_i=-\begin{vmatrix} 1 & y_j \\ 1 & y_m \end{vmatrix} \qquad c_i=-\begin{vmatrix} x_j & 1 \\ x_m & 1 \end{vmatrix} \tag{B.4}$$

Other constants are obtained by cyclic interchange of the subscripts in the order m, i, j.

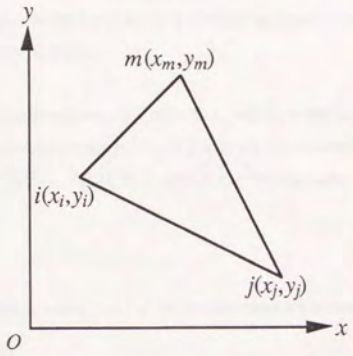

Fig.B.1 Triangle element

Ground strains are defined as derivatives of ground displacement with respect to space as

$$\{\varepsilon\}=\{\varepsilon_x,\ \varepsilon_y,\ \gamma_{xy}\}^T$$
$$=\left\{\frac{\partial u}{\partial x},\ \frac{\partial v}{\partial y},\ \frac{\partial u}{\partial y}+\frac{\partial v}{\partial x}\right\}^T \tag{B.5}$$

Substituting Eq.(B.2) into Eq.(B.5) yields

$$\{\varepsilon\}=\mathbf{B}\{\delta\}$$
$$=[\mathbf{B}_i\ \mathbf{B}_j\ \mathbf{B}_m]\{\delta\} \tag{B.6}$$

where

$$\mathbf{B}_k=\frac{1}{2\Delta}\begin{bmatrix} b_k & 0 \\ 0 & c_k \\ c_k & b_k \end{bmatrix} \quad (k=i, j, m) \tag{B.7}$$

$$\{\delta\}=\{\mathbf{U}_i, \mathbf{U}_j, \mathbf{U}_m\}^T \tag{B.8}$$

$$\mathbf{U}_k=\{u_k, v_k\}^T \quad (k=i, j, m) \tag{B.9}$$

As seen from Eq.(B.1), ground displacement is assumed to be represented by a linear function of coordinates. Consequently ground strain is uniform in an element. From this point of view, ground strains here defined should be considered as the average ground strains between observation stations.

The two event records shown in Table B.1, which were analyzed in Chapter 4, are employed to calculate ground strains. Fig.B.2 shows an example of ground strain time histories (Sasaki et al, 1988a). Table B.2 shows the maximum values of normal ground strains ε_x and ε_y.

Table B.1 Earthquakes analyzed for finite element estimation of ground strains

Site	Date	Epicentral Region	Magnitude	Epicentral Distance[km]	Azimuth [degree]*
Sagara	11/24/83	S Coast of Chubu	5.0	45	277
Numazu	9/5/88	E Yamanashi Prefecture	5.6	45	25

Note: * Clockwise from north

Table B.2 Maximum normal ground strains

Site	Station Combination	Station Separation [m]	ε_x ($\times 10^{-6}$)	ε_y ($\times 10^{-6}$)
Sagara	3-5-6	313-262-336	10.0	11.0
	5-7-6	160-247-262	14.6	11.1
	3-8-5	491-287-313	7.4	10.1
Numazu	6-7-8	236-75-202	9.5	12.6
	6-8-9	202-165-216	9.0	5.2
	11-13-12	87-311-310	9.5	10.1

B.3 Conclusions

Ground strains are estimated by a two dimensional finite element method. The same data set of ground motion records which were employed to calibrate the proposed ground motion spectral models are used for this analysis. The maximum ground strains here obtained coincide fairly well with those estimated from the ground motion spectral models proposed in the previous chapters.

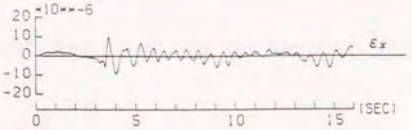

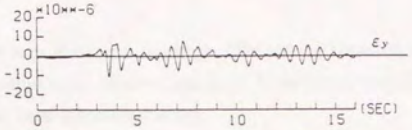

(a) Stations 3, 5 and 6

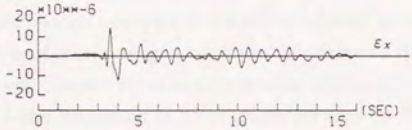

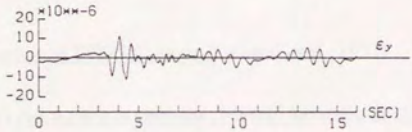

(b) Stations 5, 7 and 6

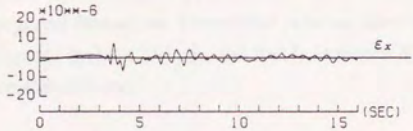

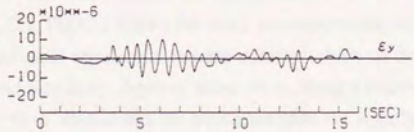

(c) Stations 3, 8 and 5

Fig.B.2 Ground strain time histories at Sagara site, 11/24/83

APPENDIX C.
ATTENUATION CHARACTERISTICS OF GROUND STRAINS AT PWRI

C.1 General Remarks

The Public Works Research Institute, Ministry of Construction, Japan has been conducting strong motion array observation at its Tsukuba campus since 1979. There are two three-dimensional local laboratory arrays.

Assuming that ground displacement is represented by a linear function of location, a three dimensional finite element method is employed to calculate ground strains. Empirical formulae of attenuation of maximum ground strains are presented in terms of earthquake magnitude and epicentral distance by multiple regression analyses. Ground motion records from 78 earthquakes with a magnitude of 4.0 or greater are used for this analysis.

C.2 Array Instrumentation at PWRI Campus (Ohkubo et al., 1981)

The Public Works Research Institute (PWRI), Ministry of Construction is located in Tsukuba City, approximately 60 km north-east of Tokyo. The local soil condition at PWRI consists of almost horizontally layered alternation of diluvial sandy and clayey deposits underlain by gravel formations. Shear wave velocity between the ground surface and 50 m below the surface is about 250 m/s, and that for between 50 m and 100 m below the surface is approximately 400 m/s.

The two local laboratory arrays are deployed at A-Field and B-Field as shown schematically in Fig.C.1. Fig.C.2 shows the array instrumentation at A-Field and B-Field. At A-Field, thirteen tri-axial accelerometers are installed; three on the ground surface, five at the depth of 2 m and five at the depth of about 50 m, along a cross-shaped configuration with each length of 100 m. At B-Field, six accelerometers are installed; one at the depth of 2 m, four at the depth of about 50 m and one at 96 m below the surface, along a L-shaped line with 100 m and 50 m long legs. The direction of cross and L shaped configurations as well as the direction of the accelerometers are set for north-south and east-west directions. Signals of each accelerometer are simultaneously transmitted by cable to a central

processing room, where the signals are digitized at a time interval of 1/100 second by 12 bits AD converters. The observation began in 1979.

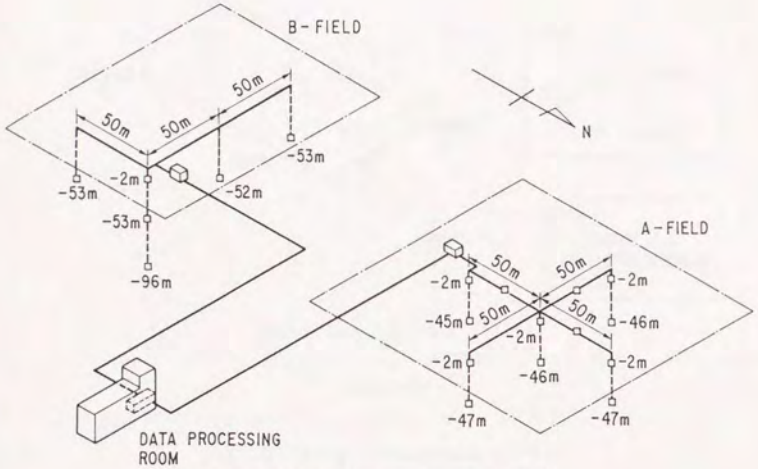

Fig.C.1 Local laboratory arrays at PWRI

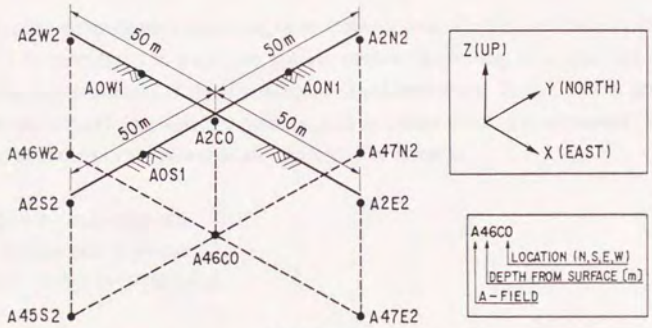

(a) A-Field

Fig.C.2(1) Array instrumentation at PWRI

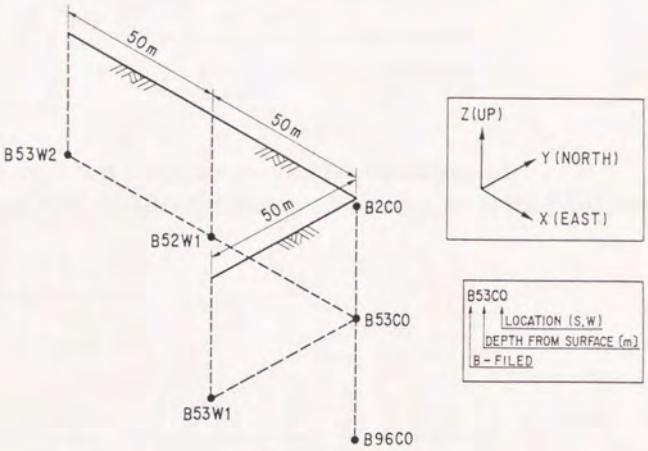

(b) B-Field

Fig.C.2(2) Array instrumentation at PWRI

C.3 Calculation of Ground Strains

A tetrahedron element consisting of four observation points i, j, m and p as shown in Fig.C.3 is considered to calculate ground strains. According to a standard three dimensional finite element analysis procedure (Zienkiewicz and Taylor, 1989), ground displacement $u(t)$, $v(t)$ and $w(t)$ at a point (x, y, z) in x (east-west), y (north-south) and z (up-down) directions in a tetrahedron are assumed to be linear as

$$u(t)=\alpha_1+\alpha_2 x+\alpha_3 y+\alpha_4 z$$
$$v(t)=\alpha_5+\alpha_6 x+\alpha_7 y+\alpha_8 z$$
$$w(t)=\alpha_9+\alpha_{10} x+\alpha_{11} y+\alpha_{12} z \qquad \text{(C.1)}$$

in which α_i $(i=1\cdots12)$ represents a constant. Determining α_i by prescribing coordinates of the four observation points i, j, m and p, Eq.(C.1) can be written as

$$\begin{Bmatrix} u(t) \\ v(t) \\ w(t) \end{Bmatrix} = \frac{1}{6V} \begin{bmatrix} u_i(t) & u_j(t) & u_m(t) & u_p(t) \\ v_i(t) & v_j(t) & v_m(t) & v_p(t) \\ w_i(t) & w_j(t) & w_m(t) & w_p(t) \end{bmatrix} \begin{Bmatrix} a_i+b_ix+c_iy+d_iz \\ a_j+b_jx+c_jy+d_jz \\ a_m+b_mx+c_my+d_mz \\ a_p+b_px+c_py+d_pz \end{Bmatrix} \tag{C.2}$$

where

x_k, y_k, z_k (k=i, j, m, p): coordinates of k-th observation point

$u_k(t)$, $v_k(t)$, $w_k(t)$ (k=i, j, m, p): ground displacement at k-th observation point

$$6V = \begin{vmatrix} 1 & x_i & y_i & z_i \\ 1 & x_j & y_j & z_j \\ 1 & x_m & y_m & z_m \\ 1 & x_p & y_p & z_p \end{vmatrix} \tag{C.3}$$

$$a_i = \begin{vmatrix} x_j & y_j & z_j \\ x_m & y_m & z_m \\ x_p & y_p & z_p \end{vmatrix} \quad b_i = -\begin{vmatrix} 1 & y_j & z_j \\ 1 & y_m & z_m \\ 1 & y_p & z_p \end{vmatrix} \quad c_i = -\begin{vmatrix} x_j & 1 & z_j \\ x_m & 1 & z_m \\ x_p & 1 & z_p \end{vmatrix} \quad d_i = -\begin{vmatrix} x_j & y_j & 1 \\ x_m & y_m & 1 \\ x_p & y_p & 1 \end{vmatrix} \tag{C.4}$$

Other constants are defined by cyclic interchange of the subscripts in the order p, i, j, m.

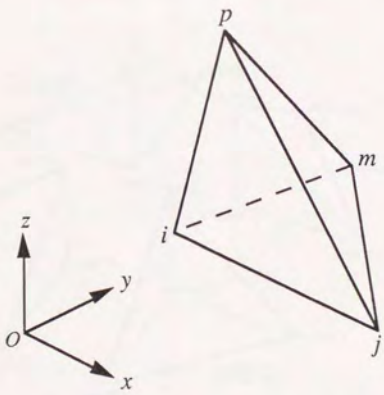

Fig.C.3 Tetrahedron element

Ground strains are defined as

$$\{\varepsilon\}=\{\varepsilon_x,\ \varepsilon_y,\ \varepsilon_z,\ \gamma_{xy},\ \gamma_{yz},\ \gamma_{zx}\}^T$$

$$=\left\{\frac{\partial u}{\partial x},\ \frac{\partial v}{\partial y},\ \frac{\partial w}{\partial z},\ \frac{\partial u}{\partial y}+\frac{\partial v}{\partial x},\ \frac{\partial v}{\partial z}+\frac{\partial w}{\partial y},\ \frac{\partial w}{\partial x}+\frac{\partial u}{\partial z}\right\}^T \tag{C.5}$$

Substituting Eq.(C.2) into Eq.(C.5) gives

$$\{\varepsilon\}=\mathbf{B}\{\delta\}$$

$$=[\mathbf{B}_i\ \mathbf{B}_j\ \mathbf{B}_m\ \mathbf{B}_p]\{\delta\} \tag{C.6}$$

where

$$\mathbf{B}_k=\frac{1}{6V}\begin{bmatrix} b_k & 0 & 0 \\ 0 & c_k & 0 \\ 0 & 0 & d_k \\ c_k & b_k & 0 \\ 0 & d_k & c_k \\ d_k & 0 & b_k \end{bmatrix}\ (k=i,\ j,\ m,\ p) \tag{C.7}$$

$$\{\delta\}=\{\mathbf{U}_i,\ \mathbf{U}_j,\ \mathbf{U}_m,\ \mathbf{U}_p\}^T \tag{C.8}$$

$$\mathbf{U}_k=\{u_k,\ v_k,\ w_k\}^T\ (k=i,\ j,\ m,\ p) \tag{C.9}$$

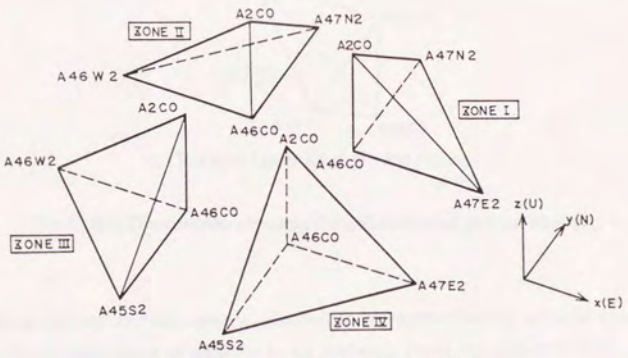

(a) A-Field, lower level ground strains

Fig.C.4(1) Tetrahedron elements for calculation of ground strains

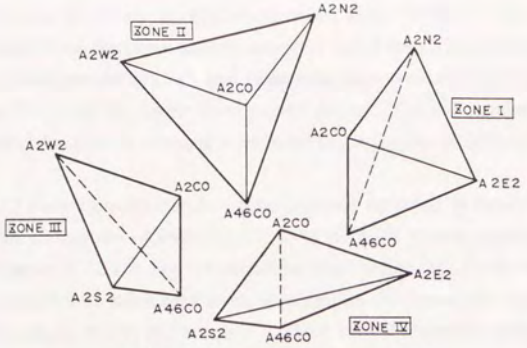

(b) A-Field, upper level ground strains

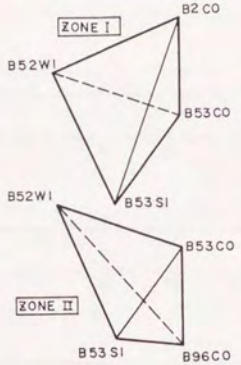

(c) B-Field, lower level ground strains

Fig.C.4(2) Tetrahedron elements for calculation of ground strains

Since ground displacement is assumed to be represented by a linear function of coordinates, ground strain is uniform in an element. From this point of view, ground strains here defined should be considered as the average ground strains between observation points.

Eight tetrahedrons are formulated to calculate ground strains at A-Field using ten observation points as shown in Fig.C.4 (Arakawa et al, 1985). Let us call the strains mainly calculated from the observation points 50 m below the surface shown in Fig.C.4 (a) as the "lower level ground strains", and those calculated from mainly the surface points shown in Fig.C.4 (b) as the "upper level ground strains". The two tetrahedrons shown in Fig.C.4 (c) are considered to calculate lower level ground strains at B-Field.

Fig.C.5 shows the acceleration time histories recorded at the observation point A2C0 from an earthquake of February 27, 1983 (EQ-28) with a magnitude of 6.0 and epicentral distance of 22 km. Fig.C.6 shows the displacement time histories for the same event. Displacement is calculated from acceleration by numerical integration in the frequency domain as shown in Section 2.3, where cut-off frequencies are set as f_{ll}=1/6, f_{lu}=1/5, f_{ul}=20, f_{uu}=21 [Hz].

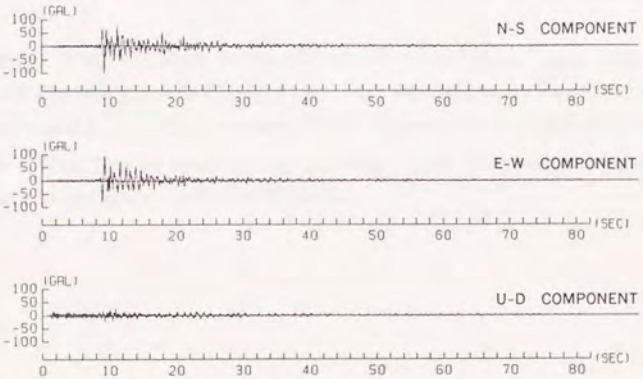

Fig.C.5 Acceleration time histories at A2C0 from EQ-28

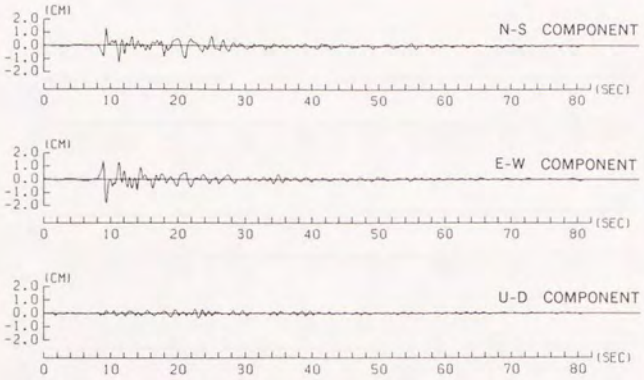

Fig.C.6 Displacement time histories at A2C0 from EQ-28

Figs.C.7 and C.8 show the time histories of the lower and upper level ground strains at A-Field calculated for EQ-28. As seen from these figures, the maximum values of horizontal strains ε_x, ε_y and γ_{xy} are about 50×10^{-6} for the lower level ground strains, and are $(100–150)\times10^{-6}$for the upper level ground strains. These strains are among the largest ground strains ever obtained at the PWRI campus.

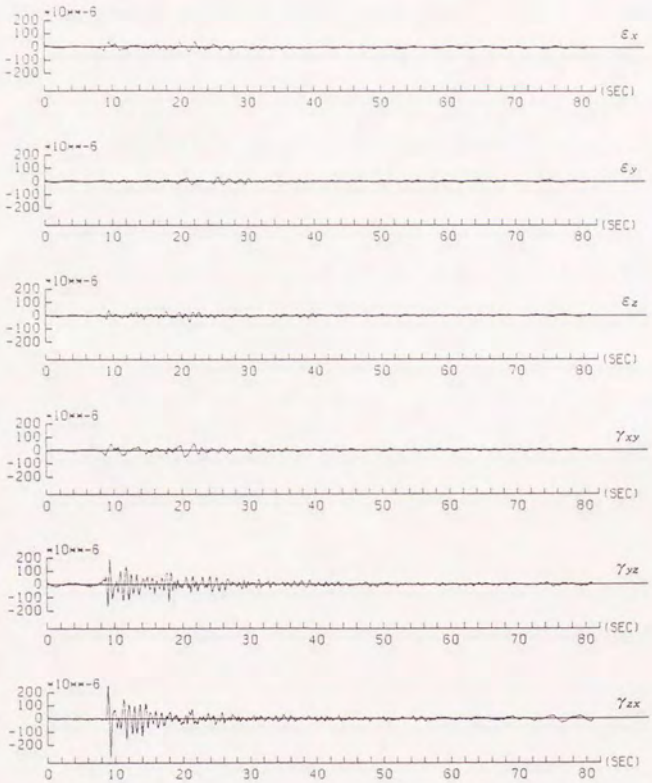

Fig.C.7 Lower level ground strains at A-Field from EQ-28 (Zone II)

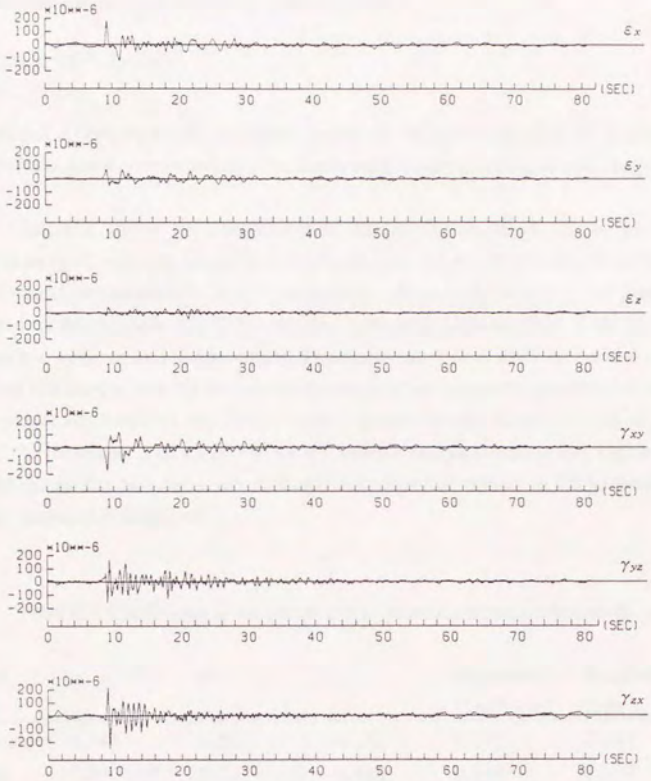

Fig.C.8 Upper level ground strains at A-Field from EQ-28 (Zone II)

C.4 Attenuation Characteristics of Ground Strains

The following empirical equation (Kawashima et al., 1984, 1985a) is adopted to study the attenuation characteristics of ground motions:

$$X=a\times10^{bM}\times(\Delta+30)^{c} \tag{C.10}$$

where M and Δ [km] represent earthquake magnitude and epicentral distance, respectively. Coefficients a, b and c are constants to be determined by a multiple regression analysis.

Table C.1 shows the coefficients of attenuation equations of the maximum acceleration [gal], velocity [cm/s] and displacement [cm] at A2C0 point (Tokida et al., 1989). Ground motion records from 78 earthquakes with a magnitude of 4.0 or greater are employed for this analysis. Fig.C.9 shows the attenuation characteristics of the maximum acceleration, velocity and displacement. Regression curves for M=5, 6, 7 and 8 are also presented. Comparing with the attenuation equations of the maximum acceleration, velocity and displacement based on the SMAC accelerograph records (Kawashima et al., 1984, 1985a), the parameter b of Eq.(C.10) for the records analyzed here shows higher value. This fact means that the attenuation characteristics of ground motions at PWRI are affected much by earthquake magnitude.

Table C.1 Coefficients of maximum ground motion attenuation equations

Ground Motion	a	b	c	Correlation Coefficient	Standard Error
Acceleration	9.344	0.511	−1.252	0.770	0.225
Velocity	7.930×10^{-2}	0.720	−1.420	0.863	0.239
Displacement	1.819×10^{-3}	0.729	−1.039	0.908	0.216

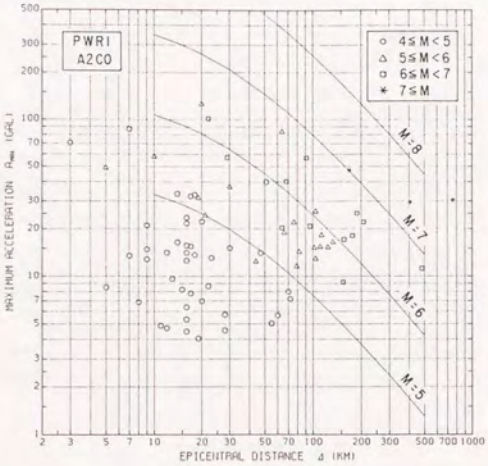

(a) Maximum acceleration

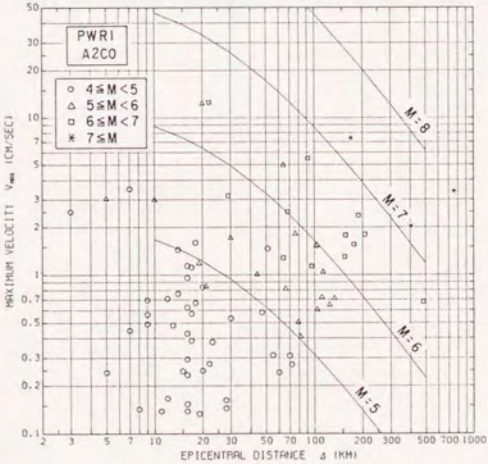

(b) Maximum velocity

Fig.C.9(1) Attenuation characteristics of maximum ground motions

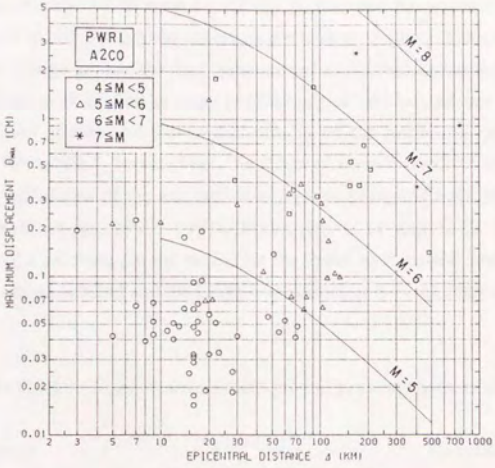

(c) Maximum displacement

Fig.C.9(2) Attenuation characteristics of maximum ground motions

The same expression with Eq.(C.10) is assumed to represent the attenuation characteristics of maximum ground strains on the horizontal plane. Since the peak values of ground strains change among the four tetrahedrons at A-Field and among two at B-Field, the average of the peak ground strains over four or two tetrahedrons are designated as the maximum ground strains. As for normal strains on the horizontal plane, after taking averages both for ε_x and ε_y for an event, the larger of them is used for analysis. Table C.2 tabulates the coefficients of the attenuation equations estimated from multiple regression analyses (Tokida et al., 1990, 1991). Figs.C.10, C.11 and C.12 show attenuation characteristics of maximum ground strains for the lower level ground strains at A-Field, the upper level strains at A-Field and the lower level strains at B-Field, respectively.

Table C.2 Coefficients of maximum ground strain attenuation equations

Site	Strain	a	b	c	Correlation Coefficient	Standard Error
A-Field	ε_{max}	1.285	0.309	–0.370	0.708	0.213
lower-level	γ_{max}	1.549	0.293	–0.319	0.699	0.212
A-Field	ε_{max}	1.237	0.493	–0.741	0.829	0.206
upper-level	γ_{max}	0.894	0.548	–0.774	0.856	0.210
B-Field	ε_{max}	1.506	0.358	–0.569	0.736	0.197
lower-level	γ_{max}	4.860	0.312	–0.596	0.690	0.190

Attenuation equation: $\left.\begin{matrix}\varepsilon_{max}\\ \gamma_{max}\end{matrix}\right\rbrace = a\times 10^{bM}\times(\Delta+30)^{c}\times 10^{-6}$

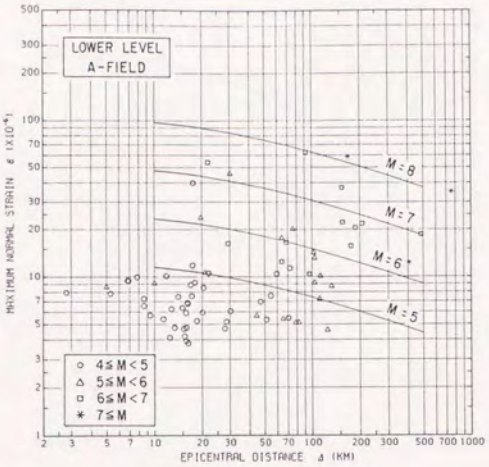

(a) Maximum normal strain

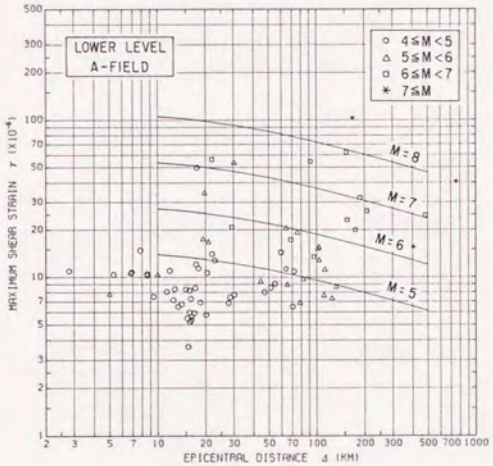

(b) Maximum shear strain

Fig.C.10 Attenuation characteristics of lower level ground strain at A-Field

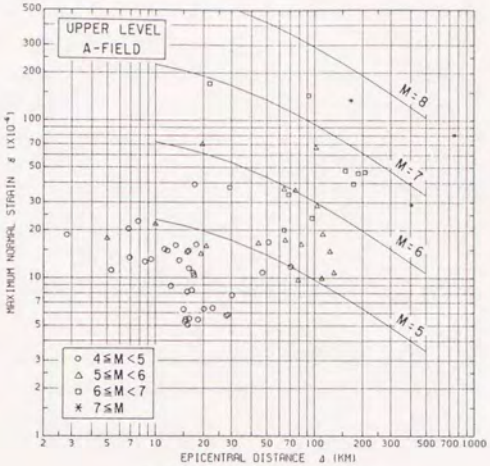

(a) Maximum normal strain

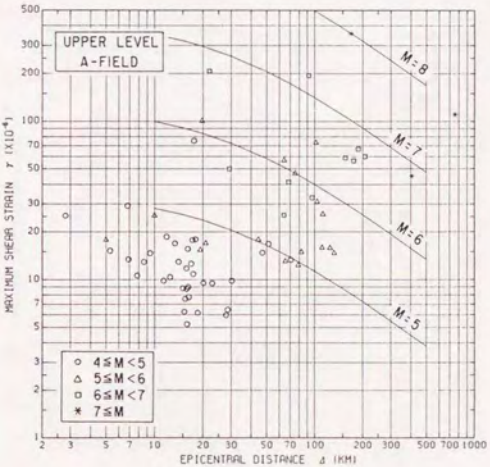

(b) Maximum shear strain

Fig.C.11 Attenuation characteristics of upper level ground strain at A-Field

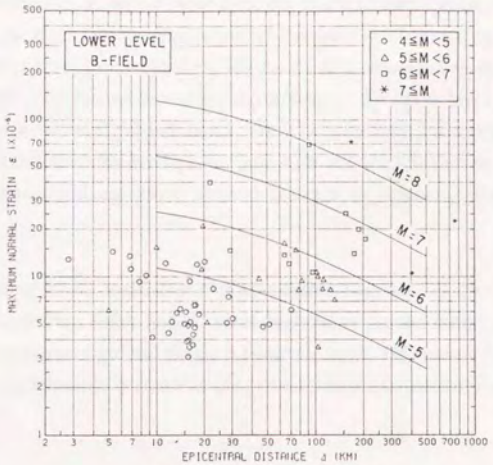

(a) Maximum normal strain

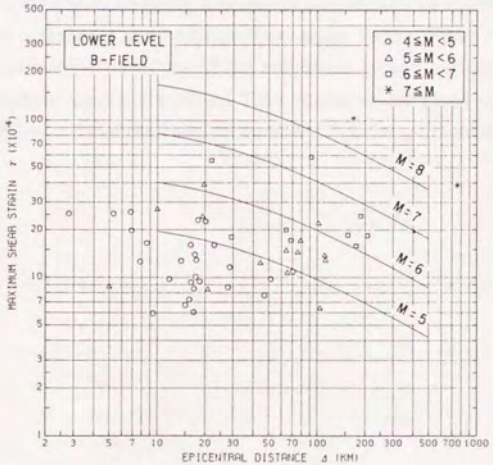

(b) Maximum shear strain

Fig.C.12 Attenuation characteristics of lower level ground strain at B-Field

The coefficient b, which represents the effect of earthquake magnitude on the maximum ground strains, of the attenuation for the upper level ground strains is larger than that for the lower level ground strains. The coefficient c, which represents the effect of epicentral distance on the maximum ground strains, of the upper level strains is smaller than that for the lower level ground strains. These facts indicate that the upper level ground strains are affected much by earthquake magnitude and the attenuation rate of the upper level ground strains with epicentral distance is larger, as compared with the lower level ground strains.

Comparing to the coefficient c of attenuation equations of the maximum ground motions estimated from either SMAC accelerograms or ground motion records at A2C0 point, c for the maximum ground strains is relatively large. This means that the attenuation rate with epicentral distance is small for the ground strains estimated in this analysis.

C.4 Conclusions

Ground strains induced during earthquakes are evaluated by a finite element method using the dense instrument array data obtained at the Public Works Research Institute campus. The attenuation equations of the maximum ground motions and strains are presented by multiple regression analyses. These results are compared with the attenuation characteristics of ground motions based on the SMAC accelerograph records.

REFERENCES

Abrahamson, N. A. (1985). "Estimation of Seismic Wave Coherency and Rapture Velocity Using the SMART-1 Strong-Motion Array Recordings", *Earthquake Engineering Research Center Report*, No.UCB/EERC-85/02, University of California, Berkeley.

Abrahamson, N. A., Bolt, B. A., Darragh, M., Penzien, J. and Tsai, Y. B. (1987). "The SMART-1 Accelerograph Array (1980-1987): A Review", *Earthquake Spectra*, Vol.3, No.2.

Arakawa, T., Kawashima, K., Tamura, K., Aizawa, K. and Takahashi, K. (1982). "Dense Instrument Array Observation by Public Works Research Institute – Observation System at Sagara Site –", *Technical Memorandum of PWRI*, No.1847 (in Japanese).

Arakawa, T., Kawashima, K., Tamura, K., Aizawa, K. and Takahashi, K. (1983a). "Dense Instrument Array Observation by Public Works Research Institute – Observation System at Yaizu Site –", *Technical Memorandum of PWRI*, No.1994 (in Japanese).

Arakawa, T., Kawashima, K., Tamura, K., Aizawa, K. and Takahashi, K. (1983b). "Experimental Study on Recording Accuracy of a Digital Strong Motion Accelerograph for Dense Instrument Array Observation", *Technical Memorandum of PWRI*, No.2019 (in Japanese).

Arakawa, T., Sasaki, Y., Kawashima, K., Tamura, K., Aizawa, K. and Takahashi, K. (1984). "Dense Instrument Array Observation by Public Works Research Institute – Observation System at Numazu Site –", *Technical Memorandum of PWRI*, No.2140 (in Japanese).

Arakawa, T., Kawashima, K. and Tamura, K. (1985). "Finite Ground Strains Induced During Earthquake for Application to Seismic Design of Underground Structures", *Proc. of 5th International Conference on Numerical Methods in Geomechanics*.

Bendat, J. S. and Piersol, A. G. (1986). *Random Data*, Analysis and Measurement Procedures, Second Edition, John Wiley & Sons.

Bolt, B. A. (1973). "Duration of Strong Ground Motion", *Proc. of 5th World Conference on Earthquake Engineering*.

Bolt, B. A., Loh, C. H., Penzien, J. and Tsai, Y. B. (1982). "Preliminary Report on the SMART-1 Array in Taiwan", *Earthquake Engineering Research Center Report*, No.UCB/EERC-82/13, University of California, Berkeley.

Bolt, B. A. ed. (1987). *Seismic Strong Motion Synthetics*, Academic Press.

Capon, J. (1969). "High-Resolution Frequency-Wavenumber Spectrum Analysis", *Proc. of IEEE*, Vol.57, No.8.

Darragh, R. B. (1988). "Analysis of Near-Source Waves: Separation of Wave Types Using Strong Motion Array Recordings", *Earthquake Engineering Research Center Report*, No.UCB/EERC-88/08, University of California, Berkeley.

Deodatis, G. and Shinozuka, M. (1989). "Simulation of Seismic Ground Motion Using Stochastic Waves", *Journal of Engineering Mechanics*, ASCE, Vol.115, No.12.

Farjoodi, J., Katayama, T. and Sato, N. (1985). "Ground Strain Characteristics Deduced by Using Dense Seismograph Array Data", *Proc. of 18th JSCE Earthquake Engineering Symposium*.

Goto, H., Kameda, H., Sugito, M. and Imanishi, N. (1978). "Correction of SMAC-B2 Accelerograph Records by Digital Filter", *Proc. of Japan Society of Civil Engineers*, No.277 (in Japanese).

Hao, H. (1989). "Effects of Spatial Variation of Ground Motions on Large Multiply-supported Structures", *Earthquake Engineering Research Center Report*, No.UCB/EERC-89/06, University of California, Berkeley.

Harada, T. (1984). "Probabilistic Modeling of Spatial Variation of Strong Earthquake Ground Displacements", *Proc. of 8th World Conference on Earthquake Engineering*.

Harada, T. and Shinozuka, M. (1988). "Stochastic Analysis of Seismic Ground Motions in Space and Time", *Proc. of 9th World Conference on Earthquake Engineering*.

Harada, T. and Shinozuka, M. (1989). "Stochastic Response of Ground and Its Implication for Spatial Variation of Earthquake Ground Motion", *Proc. of 5th International Conference on Structural Safety and Reliability*.

Harichandran, R. S. and Vanmarcke, E. H. (1986). "Stochastic Variation of Earthquake Ground Motion in Space and Time", *Journal of Engineering Mechanics*, ASCE, Vol.112, No.2.

Harichandran, R. S. (1988). "Local Spatial Variation of Earthquake Ground Motion", *Earthquake Engineering and Soil Dynamics 2 - Recent Advances in Ground-Motion Evaluation*, ASCE.

Hayashi, Y., Katukura, H., Watanabe, T., Kataoka, S., Yokota, H. and Tanaka, T. (1991). "Reliability of Integrated Displacements from Accelerograms by Digital Accelerographs", *Journal of Structural and Construction Engineering*, Architectural Institute of Japan, No.419 (in Japanese).

Hino, M. (1977). *Spectral Analysis*, Asakura Press (in Japanese).

Hoshiya, M., Ishii, K. and Kurita, H. (1987). "Simulation of Spatially and Temporally Variative Earthquake Ground Motions", *Proc. of Japan Society of Civil Engineers*, No.386/I-8 (in Japanese).

Iai, S., Kurata, E. and Tsuchida, H. (1978a). "Digitization and Corrections of Strong-Motion Accelerograms", *Technical Note of Port and Harbour Research Institute*, No.286 (in Japanese).

Iai, S. and Kurata, E. (1978b). "Integration of Strong-Motion Accelerograms", *Proc. of 5th Japan Earthquake Engineering Symposium*.

IASPEI/IAEE (1988). *Proc. of 2nd Workshop on Processing of Seismic Strong Motion Records*.

Isenberg, J., Richardson, E., Kameda, H. and Sugito, M. (1990). "Pipeline Response at Parkfield, CA to Loma Prieta Earthquake", *Proc. of 4th U.S. National Conference on Earthquake Engineering*.

Iwamoto, T., Sakurai, Y., Wakai, N., Hojo, S. and Furusyo, K. (1982a). "Observation of Dynamic Behavior of Earthquake-Proof Ductile Pipelines during Earthquakes", *Technical Report of Kubota Ltd.*, Vol.7, No.1.

Iwamoto, T., Wakai, N. and Yamaji, T. (1982b). "Observation of Dynamic Behavior of Anti-Earthquake Ductile Pipelines in Water-Main during Earthquake", *Proc. of 6th Japan Earthquake Engineering Symposium* (in Japanese).

Iwan, W. D. ed. (1978). "Strong-Motion Earthquake Instrument Arrays", *Proc. of International Workshop on Strong-Motion Earthquake Instrument Arrays*.

Iwan, W. D., Moser, M. A. and Peng, C. Y. (1985). "Some Observations of Strong-Motion Earthquake Measurement Using a Digital Accelerograph" *Bulletin of Seismological Society of America*, Vol.75, No.5.

Iwasaki, T., Sasaki, Y., Tamura, K., Aizawa, K. and Takahashi, K. (1986). "Dense Instrument Array System by PWRI for Observing Strong Earthquake Motion", *Proc. of 18th Joint Meeting, U.S.-Japan Panel on Wind and Seismic Effects*, UJNR.

Japan Road Association (1974). *Guidelines of Earthquake Countermeasures for Petroleum Pipelines* (in Japanese).

Japan Road Association (1986). *Design Guidelines for Common Utility Ducts* (in Japanese).

Japan Road Association (1990). *Design Specifications for Highway Bridges, Part V Seismic Design* (in Japanese).

Japan Sewage Works Association (1979). *Guidelines of Earthquake Countermeasures for Sewage Facilities* (in Japanese).

Japan Society of Civil Engineers (1975). *Specifications for Earthquake-Resistant Design of Submerged Tunnels* (in Japanese).

Japan Society of Civil Engineers (1988). *Earthquake Resistant Design for Civil Engineering Structures in Japan.*

Japan Society of Civil Engineers (1989a). *Research Report on Development of a Database for Strong Motion Array Records.*

Japan Society of Civil Engineers (1989b). *Dynamic Analysis and Seismic Design, Vol.4, Lifeline Facilities* (in Japanese).

Japan Water Works Association (1979). *Guidelines of Earthquake Resistant design for Water Supply Facilities* (in Japanese).

Kamiyama, M. (1976). "Stress and Strain in Ground during Earthquake", *Proc. of Japan Society of Civil Engineers*, No.250 (in Japanese).

Kataoka, S., Yokota, H., Tanaka, T., Katsukura, H., Hayashi, Y. and Watanabe, T. (1990). "Vibration Tests of Digital Strong-Motion Accelerographs by a Large-Scale Shaking Table", *Proc. of 8th Japan Earthquake Engineering Symposium* (in Japanese).

Katayama, T. and Sato, N. (1982). "Ground Strain Measurement by a Very Densely Located Seismometer Array", *Proc. of 6th Japan Earthquake Engineering Symposium.*

Katayama, T., Farjoodi, J. and Sato, N. (1984). "Measurement of Seismic Ground Strain by a Dense Seismograph Array", *Proc. of 8th World Conference on Earthquake Engineering.*

Katayama, T., Yamazaki, F., Nagata, S., Lu, L. and Turker, T. (1990a). "Development of Strong Motion Database for the Chiba Seismometer Array", *Report of Earthquake Disaster Mitigation Engineering Laboratory*, No.14, Institute of Industrial Science, University of Tokyo.

Katayama, T., Yamazaki, F., Nagata, S., Lu, L. and Turker, T. (1990b). "A Strong Motion Database for the Chiba Seismometer Array and Its Engineering Analysis", *Earthquake Engineering and Structural Dynamics*, Vol.19, No.8.

Kawakami, H. and Sato, Y. (1983). "Effect of Deformation of Seismic Waves on Estimated Value of Ground Relative Displacement or Strain", *Proc. of Japan Society of Civil Engineers*, No.337 (in Japanese).

Kawashima, K., Takagi, Y. and Aizawa, K. (1982a). "Accuracy of Digitization of Strong-Motion Records Obtained by SMAC Accelerograph", *Proc. of Japan Society of Civil Engineers*, No.323 (in Japanese).

Kawashima, K., Takagi, Y. and Aizawa, K. (1982b). "Procedure of Instrument Correction and Displacement Calculation for SMAC-B2 Accelerograph Records with

Considering Accuracy of Digitization", *Proc. of Japan Society of Civil Engineers*, No.325 (in Japanese).

Kawashima, K., Aizawa, K. and Takahashi, K. (1983). "Effects of Composition of Two Horizontal Components on Attenuation of Maximum Earthquake Ground Motions and Response Spectra", *Proc. of Japan Society of Civil Engineers*, No.329 (in Japanese).

Kawashima, K., Aizawa, K. and Takahashi, K. (1984). "Attenuation of Peak Ground Motion and Absolute Acceleration Response Spectra", *Proc. of 8th World Conference on Earthquake Engineering*.

Kawashima, K., Aizawa, K. and Takahashi, K. (1985a). "Attenuation of Peak Ground Motions and Absolute Acceleration Response Spectra", *Report of PWRI*, No.166 (in Japanese).

Kawashima, K., Aizawa, K. and Takahashi, K. (1985b). "Duration of Strong Motion Acceleration Records", *Proc. of Japan Society of Civil Engineers*, No.362/I-4.

Kawashima, K., Hasegawa, K. and Nagashima, H. (1991). "Seismic Behavior of Buried Pipelines through Field Observation", *Proc. of 3rd U.S. National Conference on Lifeline Earthquake Engineering*.

Kitagawa, Y., Ohkawa, I. and Kashima, T. (1988). "Dense Strong Motion Earthquake Seismometer Array at Site with Different Topographic and Geologic Conditions in Sendai", *Proc. of 9th World Conference on Earthquake Engineering*.

Kogarumai, M., Hojo, S. and Iwamoto, T. (1978). "Observation of Dynamic Behavior of Anti-Earthquake Ductile Pipes in Water-Main for Supply to Water Purification Yard at Hakusan, Hachinohe City during Earthquake", *Proc. of 5th Japan Earthquake Engineering Symposium* (in Japanese).

Kogarumai, M., Hojo, S. and Iwai, S. (1979). "Observation of Dynamic Behavior of Anti-Earthquake Ductile Pipes at Shimonaga, Hachinohe City during Earthquake", *Proc. of 15th JSCE Earthquake Engineering Symposium* (in Japanese).

Loh, C. H. (1985). "Analysis of the Spatial Variation of Seismic Waves and Ground Movements from SMART-1 Array Data", *Earthquake Engineering and Structural Dynamics*, Vol.13, No.5.

Loh, C. H. and Yeh, Y. T. (1988). "Spatial Variation and Stochastic Modelling of Seismic Differential Ground Movement", *Earthquake Engineering and Structural Dynamics*, Vol.16, No.4.

McCann, M. W., Jr. (1980). "RMS Acceleration and Duration of Strong Ground Motion", *John A. Blume Earthquake Engineering Center Report*, No.46, Stanford University.

Nakamura, M., Katayama, T. and Kubo, K. (1982). "Quantitative Study on Observed Seismic Strains in Underground Structures", *Proc. of Japan Society of Civil Engineers*, No.320 (in Japanese).

Newland, D. E. (1984). *An Introduction to Random Vibrations and Spectral Analysis*, Longman Scientific & Technical.

Nishio, N., Ukaji, T. and Tsukamoto, K. (1978). "Observation of Dynamic Behavior of Underground Pipelines during Earthquakes", *Proc. of 5th Japan Earthquake Engineering Symposium* (in Japanese).

Nishio, N., Yoneyama, K., Ukaji, T., Tsukamoto, K. and Hamura, J. (1979). "Study on Pipeline Response to Earthquakes (II)", *Technical Report of Research and Development Institute*, Tokyo Gas Co., No.24 (in Japanese).

Niazi, M. (1990). "Behavior of Peak Values and Spectral Ordinates of Near-Source Strong Ground Motion over the SMART-1 Array", *Earthquake Engineering Research Center Report*, No.UCB/EERC-90/17, University of California, Berkeley.

Noda, S., Kurata, E., Iai, S. and Tsuchida, H. (1982). "Observation of Earthquake Motions by Instrument Arrays in Port Area and Preliminary Analysis", *Proc. of 6th Japan Earthquake Engineering Symposium*.

Noda, S., Kurata, E. and Tsuchida, H. (1988). "Observation of Earthquake Motions by Dense Instrument Arrays at Soft Ground", *Proc. of 9th World Conference on Earthquake Engineering*.

Ohkubo, T., Iwasaki, T. and Kawashima, K. (1981). "Dense Instrument Array Program of the Public Works Research Institute and Preliminary Analysis of Some Records", *Proc. of 13th Joint Meeting, U.S.-Japan Panel on Wind and Seismic Effects*, UJNR.

Ohkubo, T., Arakawa, T. and Kawashima, K. (1984). "Dense Instrument Array Program of the Public Works Research Institute and Preliminary Analysis of the Records", *Proc. of 8th World Conference on Earthquake Engineering*.

Ohsaki, Y. (1976). *An Introduction to Spectral Analysis of Ground Motions*, Kajima Press (in Japanese).

Public Works Research Institute (1977). "A Proposal for Earthquake Resistant Design Method", *Technical Memorandum of PWRI*, No.1185 (in Japanese).

Saito, M. (1978). "An Automatic Design Algorithm for Band Selective Recursive Digital Filters", *Geophysical Exploration*, Vol.31, No.4 (in Japanese).

Sakurai, A., Takahashi, T., Tsutsumi, H. and others (1967). "Dynamic Stresses of Underground Pipe Lines during Earthquakes", *Report of Research Laboratory*, Central Research Institute of Electric Power Industry, No.67058 (in Japanese).

Sakurai, A. and Takahashi, T. (1969). "Observation of Ground Strains from Matsushiro Swarm Earthquakes and Estimation of Underground Pipe Strains", *Proc. of 9th JSCE Earthquake Engineering Symposium* (in Japanese).

Sakurai, A., Takahashi, T., Kurihara, C. and Yajima, H. (1970). "Dynamic Stresses of Underground Pipe Lines during Earthquakes 2", *Report of Research Laboratory*, Central Research Institute of Electric Power Industry, No.69087 (in Japanese).

Sasaki, Y., Tamura, K., Aizawa, K. and Takahashi, K. (1985). "Dense Instrument Array Observation by Public Works Research Institute – Observation System at Matsuzaki Site –", *Technical Memorandum of PWRI*, No.2238 (in Japanese).

Sasaki, Y., Tamura, K. and Aizawa, K. (1988a). "Analysis on Ground Motions during Earthquakes Observed by Dense Arraies around Suruga Bay", *Technical Memorandum of PWRI*, No.2546 (in Japanese).

Sasaki, Y., Tamura, K. and Aizawa, K. (1988b). "Analysis of Phase Velocity of Ground Motion with Use of Array Records", *Proc. of 9th World Conference on Earthquake Engineering*.

Sasaki, Y., Tamura, K. and Aizawa, K. (1989). "Estimation of Ground Motions from Strong Motion Records on Ground Surface", *Technical Memorandum of PWRI*, No.2797 (in Japanese).

Sato, N. and Katayama, T. (1983). "Observation of Earthquake Ground Motions and Strains", *Seisan-Kenkyu*, Institute of Industrial Science, University of Tokyo, Vol.35, No.9 (in Japanese).

Sato, N., Katayama, T. and Farjoodi, J. (1984). "Observation of Earthquake Ground Motions and Strains (II)", *Seisan-Kenkyu*, Institute of Industrial Science, University of Tokyo, Vol.36, No.9 (in Japanese).

Sato, N., Nakamura, M., Iwamoto, T. and Ohbo, N. (1986). "Observation of Seismic Ground Motion and Buried Pipe Strain", *Proc. of 7th Japan Earthquake Engineering Symposium* (in Japanese).

Takada, S. and Wright, J. P. (1980). "Earthquake Relative Motions for Lifelines", *Proc. of Japan Society of Civil Engineers*, No.299 (in Japanese).

Tamura, K. (1984). "Dense Instrument Array Observation Systems by the Public Works Research Institute", *Japan Society for Earthquake Engineering Promotion News*, No.78 (in Japanese).

Tamura, K., Kawashima, K., Aizawa, K. and Takahashi, K. (1988). "Accuracy of Digital Strong-Motion Accelerograph with Independent Triggering and Recording System for Analysis of Finite Ground Strains during Earthquake", *Proc. of Japan Society of Civil Engineers*, No.392/I-9 (in Japanese).

Tamura, K., Winterstein, S. R. and Shah, H. C. (1990). "Random Field Models of Spatially Varying Ground Motions", *John A. Blume Earthquake Engineering Center Report*, No.92, Stanford University.

Tamura, K., Winterstein, S. R. and Shah, H. C. (1991). "Spatially Varying Ground Motion Models and Their Application to the Estimation of Differential Ground Motion", *Proc. of Japan Society of Civil Engineers*, No.437/I-17.

Tamura, K. and Aizawa, K. (1992). "Differential Ground Motion Estimation Using a Time-Space Stochastic Process Model", *Proc. of Japan Society of Civil Engineers*, No.441/I-18.

Toki, K. (1981). *Seismic Analysis of Structures*, Gihodo Press (in Japanese).

Tokida, K., Tamura, K. and Aizawa, K. (1989). "Analysis on Strong Ground Motions during Earthquakes Observed by Dense Array at PWRI – Attenuation Characteristics of Ground Strains Induced during Earthquakes –", *Technical Memorandum of PWRI*, No.2798 (in Japanese).

Tokida, K., Tamura, K. and Aizawa, K. (1990). "Attenuation Characteristics of Ground Strains during Earthquake", *Proc. of 8th Japan Earthquake Engineering Symposium*.

Tokida, K., Tamura, K. and Aizawa, K. (1991). "Attenuation Characteristics of Ground Strains Induced during Earthquake", *Proc. of 2nd International Conference on Recent Advances in Geotechnical Earthquake Engineering and Soil Dynamics*.

Trifunac, M. D. and Brady, A. G. (1975). "A Study on the Duration of Strong Earthquake Ground Motion", *Bulletin of Seismological Society of America*, Vol.65, No.3.

Tsuchida, H., Minami, K., Kiyomiya, O., Kurata, E. and Nishizawa, H. (1981). "Stress of Buried Pipe during Earthquakes Based on Two Dimensional Seismometer Array Observation", *Report of Port and Harbour Research Institute*, Vol.20, No.4 (in Japanese).

Vanmarcke, E. H. (1972). "Properties of Spectral Moments with Applications to Random Vibration", *Journal of the Engineering Mechanics Division*, ASCE, Vol.98, No.2.

Vanmarcke, E. H. and Lai, S.-S. P. (1980). "Strong-Motion Duration and RMS Amplitude of Earthquake Records", *Bulletin of Seismological Society of America*, Vol.70, No.4.

Vanmarcke, E. H. (1983). *Random Fields*, MIT Press.

Yamada, Y., Iemura, H., Izuno, K., Nakanishi, S. and Kurosawa, W. (1985). "A Three Points Array Observation by Accelerographs with Absolute Time and Estimation of Ground Strains", *Proc. of 18th JSCE Earthquake Engineering Symposium* (in Japanese).

Yamada, Y., Noda, S., Izuno, K. and Doi, H. (1989). "Attempt to Correct Digital Accelerograph Records with Kalman Filter Algorithm", *Journal of Structural Engineering*, Japan Society of Civil Engineers, Vol.35A (in Japanese).

Yamazaki, F. and Shinozuka, M. (1988). "Digital Generation of Non-Gaussian Stochastic Fields", *Journal of Engineering Mechanics*, ASCE, Vol.114, No.7.

Zienkiewicz, O. C. and Taylor, R. L. (1989). *The Finite Element Analysis*, Fourth Edition, Vol.1, Basic Formulation and Linear Problems, McGraw-Hill.

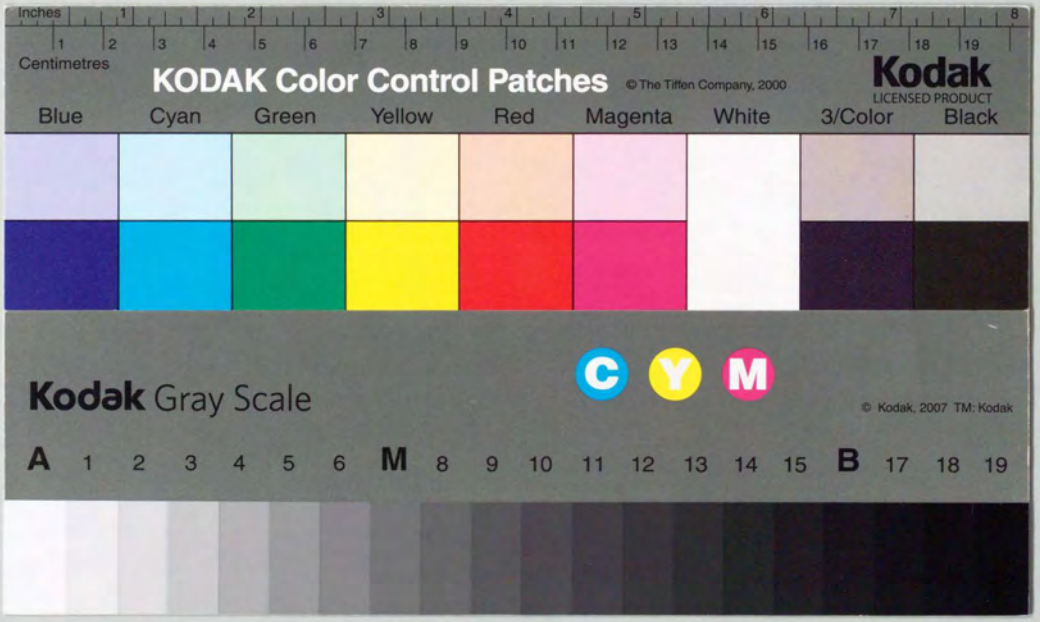
Inches
Centimetres
KODAK Color Control Patches
© The Tiffen Company, 2000
Kodak
LICENSED PRODUCT
Blue
Cyan
Green
Yellow
Red
Magenta
White
3/Color
Black
Kodak Gray Scale
C
Y
M
© Kodak, 2007 TM: Kodak
A 1 2 3 4 5 6 M 8 9 10 11 12 13 14 15 B 17 18 19